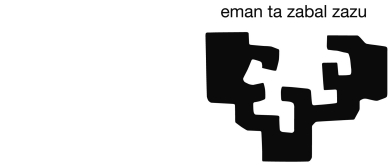

Density Functional Theory for Steady-State Thermoelectric Transport with Applications to Strongly Correlated Systems

Nahual Carlos Sobrino Coll

Nano-bio Spectroscopy Group
Donostia International Physics Center

Universidad del Pais Vasco

Supervised by
Dr. Roberto D'Agosta
Dr. Stefan Kurth

October 2021

Acknowledgements

Personal

I would like to thank my supervisors Roberto D'Agosta and Stefan Kurth for all their guidance and support throughout these years. They have always selflessly taught me about science. They really made this process a pleasant and fruitful experience.

Also thanks to David Jacob and Quim Jornet for all their help and for the good moments, specially for the interesting discussions after lunch.

Mi familia ha sido siempre el motor de mi motivación y mi sustento en todo momento, es por ello que esta tesis está dedicada a ellos. En especial a mi madre y mi padre por enseñarme siempre desde la libertad, fomentando mi desarrollo intelectual y creativo, así como a mis hermanos Gabriel y Sirio, por su generosidad y todos los buenos momentos compartidos.

También agradezco a Liliana por su compañía y apoyo durante estos años. Su decisión de acompañarme en este proceso ha sido esencial para mi.

Institutional

I acknowledge funding by Donosti International Physics Center.

Abstract

Density functional theory (DFT) has become one of the most popular and successful methods for determining the microscopic properties of matter. In particular, its low computational cost makes it an excellent method for ab-initio calculations. The successes and failures of the theory crucially depend on the accuracy of the approximations for the exchange-correlation (xc) functionals. However, some quantities are not accessible with original DFT and therefore one needs to extend the framework. In this thesis, we study equilibrium properties and propose methodological developments on the steady-state transport problem within DFT. We apply our general results for model Hamiltonians, a perfect scenario with full control of the interactions to explore the structural properties of the xc functionals which, in the case of strong correlations, are governed by steps at integer occupation.

The thesis is divided in two parts. Part I explores the multi-orbital situation at equilibrium and low temperatures. From an analysis of stability diagrams, we find that the functionals of a double quantum dot in a thermal bath subject to generic density-density interactions and Hund's rule coupling can be decomposed into four basic potentials based on the single orbital problem. In addition, we generalize this decomposition for an arbitrary number of interacting dots subject to inter- and intra-Coulomb repulsion. We also study the properties of the xc functionals for a strongly correlated double quantum dot asymmetrically coupled to the electrodes, where abrupt population inversions occur between the two dots.

Part II deals with the non-equilibrium transport problem. We extend the steady-state DFT framework to arbitrary thermal gradients between the electrodes, finding a general, exact expression for the Seebeck coefficient which is successfully applied for the single impurity Anderson model in the Kondo regime. Furthermore, we construct a general and formally exact density functional theory formalism which gives access not only to the correct density and electrical current, but also to the heat current of the interacting system in the steady-state. The linear response regime of this new framework is presented and gives access to all the transport coefficients in terms of quantities of the theory. We further apply the theory to the Anderson model and parametrize the xc functionals from a reverse engineering procedure in the Coulomb Blockade regime. Finally, using our theory in a three-terminal setup with one of the terminals only weakly connected, a general expression for the

non-equilibrium spectral function at arbitrary temperature is derived and applied for an Anderson impurity at finite bias voltage, capturing the splitting of the Kondo resonance as predicted by numerically exact many-body approaches.

Resumen

La teoría funcional de la densidad (DFT) se ha convertido en uno de los métodos más exitosos y utilizados para determinar las propiedades microscópicas de la materia. En concreto, su bajo coste computacional lo convierte en un excelente método para cálculos *ab-initio*. Los logros y fallos de la teoría dependen fundamentalmente de la precisión de las aproximaciones de los funcionales de intercambio y correlación (xc). Sin embargo, algunas cantidades no son accesibles a través del formalismo DFT original, y por tanto, una extensión del formalismo es necesaria.

En esta tesis, se revisan y proponen diferentes marcos teóricos basados en la teoría funcional de la densidad que tienen como objetivo describir el transporte eléctrico y térmico debido a electrones en el estado estacionario a través de uniones nanoscópicas. El estudio se focaliza fundamentalmente en sistemas fuertemente correlacionados, sistemas que usualmente se han considerado no poder ser descritos mediante la teoría funcional de la densidad. Mediante el uso de sistemas Hamiltonianos modelo y diferentes métodos tanto analíticos como numéricos, la estructura de los funcionales de intercambio y correlación necesarios para una correcta descripción de estos sistemas es estudiada, hayándose necesaria la inclusión de funciones de tipo escalón.

En primer lugar, las propiedades de equilibrio de los funcionales xc de puntos cuánticos multiorbitales se tratan en la parte I, donde se toma como pieza fundamental sobre la que construir funcionales una impureza única, problema bien estudiado en la literatura que sirve como base para la descripción de situaciones más complejas. Los potenciales xc de puntos cuánticos dobles en la colectividad macrocanónica sujetos a interacciones generales del tipo densidad-densidad y con interacción del tipo *Hund's rule coupling* se estudian en el capítulo 3. Para ello, se considera la solución exacta del problema de muchos cuerpos y se invierte numéricamente (ingeniería inversa) las soluciones exactas de los funcionales necesarios. A bajas temperaturas, la estructura de los potenciales de Hartree e intercambio y correlación (Hxc) fundamentalmente se compone de funciones de tipo escalón cuyas posiciones exactas dependen del régimen definido por los parámetros de interacción. Estas estructuras pueden ser entendidas y derivadas a través de un análisis de los diagramas de estabilidad. Tanto la posición de todas las funciones escalón, como la altura de cada una de ellas, es obtenida de este modo. Alternativamente, la descomposición del término de interacción del Hamiltoniano en diferentes componentes, permite

racionalizar las estructuras escalonadas de los potenciales Hxc en componentes básicos relacionados con el problema de un único orbital (problema cuya parametrización es bien conocida) de una manera sencilla. Además, la descomposición en potenciales básicos se generaliza a sistemas multiorbitales arbitrarios para la situación en la que las repulsiones Coulombianas entre electrones de un mismo punto cuántico son más grandes que la repulsión Coulombiana (que se considera común) entre electrones de distintos puntos cuánticos. La implementación de los potenciales Hxc parametrizados mediante estas dos vías equivalentes, muestran que los cálculos DFT proporcionan resultados excelentes (a bajas temperaturas) en concordancia con los resultados numéricos exactos para puntos cuánticos dobles, triples y cuádruples.

La unión de los puntos cuánticos con los terminales o depósitos de electrones, da lugar a la configuración de transporte electrónico. En el capítulo 4, estudiamos la estructura de los potenciales Hxc del punto cuántico doble cuando los acoplamientos a los depósitos son diferentes para cada punto. A bajas temperaturas y energías *in situ* similares, el vaciado brusco de una impureza y el llenado de la otra impureza a medida que el voltaje de la puerta varía continuamente, corresponde con el efecto conocido como *cambio de ocupación de nivel* (LOS). Mediante la variación del acoplamiento de una de las impurezas con los terminales, se puede controlar el LOS. En este capítulo, el objetivo se centra en la descripción de potenciales Hxc que permitan describir cualitativamente este efecto. Para ello se proponen estructuras basadas en el punto cuántico simple con un intercambio en la dependencia local del acoplamiento a los terminales, es decir, cada punto cuántico o impureza depende del acoplamiento del otro punto con los terminales. La comparación con resultados de un método exacto para este tipo de problemas de impurezas (NRG), destaca la precisión de la conductividad no interactuante (KS) a bajas temperaturas, que se describe correctamente dentro del marco propuesto por Landauer y Büttiker (LB + DFT) de transporte usando DFT (basado en funciones de Green) y está de acuerdo con la regla de la suma de Friedel. Sin embargo, la correcta descripción de las conductividades eléctricas para el punto cuántico doble depende en gran medida de los detalles de la parametrización de los funcionales Hxc . Una estructura del funcional unificada desde el acoplamiento simétrico hasta el acoplamiento completamente asimétrico con los electrodos es todavía una cuestión abierta.

La situación de transporte fuera de equilibrio se considera en la parte II. Un marco formalmente exacto en este contexto es DFT dependiente del tiempo (TDDFT). Dado que en esta tesis el estudio se focaliza en el régimen de estado estacionario, se considera un marco general propuesto recientemente para el transporte eléctrico en el estado estacionario (i-DFT) [41] que tiene la ventaja sobre TDDFT de que lo funcionales de intercambio y correlación solo dependen de la región molecular, a difrerencia de TDDFT donde los funcionales dependen de posiciones lacalizadas en

los terminales. En el capítulo 5, se generaliza i-DFT a la situación en la que hay un gradiente de temperatura finito entre los terminales o depósitos de electrones. Como consecuencia directa, se deriva una expresión exacta y analítica para el coeficiente de Seebeck del sistema interactuante que se compone como la suma de un término no interactuante (KS) y un término de corrección relacionado con una derivada de la corrección xc al voltaje del sistema en i-DFT. También se deriva una expresión general para la contribución electrónica a la conductividad térmica dentro de i-DFT, pero puesto que el formalismo i-DFT está por construcción limitado a la correcta descripción de la corriente eléctrica no está garantizada una correcta descripción de la conductividad térmica (cantidad derivada a través de la corriente de calor). Para el modelo de Anderson de una impureza simple (SIAM) se construye una aproximación a los funcionales Hxc tanto en el régimen *Coulomb Blockade* (CB) así como en el régimen de Kondo. En el CB se utiliza el proceso de ingeniería inversa de manera analítica considerando una función espectral modelo de un sistema no acoplado. Se encuentra que tanto el funcional del potencial de puerta Hxc como el potencial xc del voltaje consisten en la suma o diferencia de dos términos, cada uno de los cuales depende solo de la temperatura de uno de los terminales. Se comparan los coeficientes de transporte para el SIAM obtenidos con nuestro método con los de los cálculos NRG bien datados en la literatura. Si bien nuestra parametrización por construcción se vuelve exacta a altas temperaturas, en el régimen de Kondo ($T \ll T_K$) la concordancia es razonable pero no perfecta para la conductividad eléctrica y el coeficiente de Seebeck. Sin embargo, la conductividad térmica de i-DFT no captura el comportamiento correcto esperado en el problema de muchos cuerpos. Esta discrepancia es totalmente esperada ya que i-DFT por construcción está destinado a la descripción de la densidad en la región molecular y la corriente eléctrica a través de ella, pero no se espera que también capture correctamente la corriente de calor (o energía) a través de la región molecular. Por tanto, en el capítulo 6 se propone un nuevo marco teórico dentro de la teoría funcional de la densidad, al cual llamamos iq-DFT, para describir el transporte electrónico y de calor (energía) en el estado estacionario para una unión (molecular) conectada a $\mathcal{N}$ conductores y llevada a situaciones fuera de equilibrio a través de voltajes externos y/o gradientes de temperatura entre los terminales. Los cimientos de iq-DFT se basan en la correspondencia uno a uno entre el conjunto de "densidades" y el conjunto de "potenciales" que probamos para un entorno finito de voltajes no nulos y gradientes térmicos alrededor del equilibrio. El sistema KS correspondiente requiere $2\mathcal{N} - 1$ potenciales de intercambio y correlación que deben aproximarse en la práctica. El formalismo i-DFT puede verse como una aproximación a iq-DFT donde las contribuciones xc al campo Ψ se desprecian por completo y la contribución xc a el potencial local (puerta) es independiente de la corriente de

calor. Se desarrolla la respuesta lineal del formalismo iq-DFT para la situación de dos terminales, permitiendo acceder a todos los coeficientes lineales de transporte térmico, es decir, la conductividad eléctrica, el coeficiente de Seebeck, así como la contribución electrónica a la conductividad térmica. Todos estos coeficientes pueden expresarse exactamente en términos de cantidades accesibles a través de iq-DFT, lo que lleva a correcciones xc para los tres coeficientes de transporte. Como primera aplicación del formalismo, se procede a calcular el régimen de respuesta lineal al modelo de Anderson. A través de un proceso de ingeniería inversa y mediante el uso de una función espectral modelo (del sistema interactuante) para el regimen CB, se invierten de manera analítica las parametrizaciones de las derivadas de los potenciales xc necesarios en iq-DFT. Estos potenciales permiten reproducir con precisión los coeficientes de transporte del modelo de muchos cuerpos. Se espera que las parametrizaciones sirvan como un primer paso hacia la construcción de funcionales xc aproximados más allá del régimen CB, en analogía con el capítulo anterior. Como cualquier marco DFT, debido a la naturaleza no interactuante del sistema KS, se puede esperar que iq-DFT sea un sistema numérico altamente eficiente para el cálculo *ab-initio* del transporte de corrientes electricas y de calor a través de sistemas en la nanoescala a medida que se disponga de aproximaciones precisas para los funcionales de intercambio y correlación. Si bien la construcción de tales funcionales que se puedan usar en cálculos *ab-initio* aún es un trabajo para el futuro, se espera que nuestros estudios sobre modelos simples puedan ser una guía útil en el desarrollo de este camino.

Finalmente, en el capítulo 7 se procede a generalizar el formalismo i-DFT para el transporte en el estado estacionario a través de uniones en la nanoescala en la situación de múltiples electrodos, configuración particular del previamente descrito marco iq-DFT. En particular, para la situación de tres terminales en el límite de acoplamiento débil a uno de los electrodos (límite ideal STM), se muestra cómo se puede extraer la función espectral del estado de no-equilibrio tanto a temperatura cero como a termperaturas finitas, extiendiéndose así el trabajo anterior [108] restringido tanto al equilibrio como a temperatura cero. Para la situación específica de un modelo de Anderson acoplado a tres electrodos, se procede a construir un funcional de intercambio y correlación aproximado que describe, al menos para interacciones no demasiado fuertes, la separación o división del pico de Kondo bajo la apliación de voltajes finitos dando lugar a resultados razonables y en concordancia cualitativa con otros métodos computacionales de muchos cuerpos más demandantes como NRG y QMC de no equilibrio. Aunque para interacciones más fuertes nuestra aproximación no captura la división del pico de Kondo, no obstante se procede a identificar la característica faltante que debe incorporarse en futuros funcionales. Dado que la configuración multiterminal de i-DFT es

comparable en esfuerzo computacional a cálculos estándar LB + DFT, se puede producir resultados y estudiar systemas actualmente inaccesibles para los métodos precisos de muchos cuerpos fuera de equilibrio.

Contents

List of Abbreviations **xv**

List of Publications **xvii**

1 Introduction **1**

2 Theoretical Background **7**

2.1 Equilibrium Density Functional Theory 7

2.2 Non-Equilibrium Density Functional Theory: Steady-State Transport 13

2.2.1 Landauer-Büttiker+DFT 13

2.2.2 Steady-state density functional theory for finite bias conductances 16

2.3 Lattice Hamiltonians 18

I Equilibrium Density Functional Theory **25**

3 Multi-orbital Quantum Dots **27**

3.1 Modelling of the Hxc potentials 28

3.1.1 Hxc potentials and link to stability diagrams for the double quantum dot at low temperatures 28

3.1.2 Decomposition of the interaction into basic building blocks . 34

3.1.3 Generalization of Hxc potential to more than two orbitals . . 38

3.2 Results 39

3.2.1 Results for the double quantum dot 41

3.2.2 Results for more than two orbitals 45

4 Zero Temperature Conductance in Asymmetric Double Quantum Dot **47**

4.1 The Level Occupation Switching effect in the double quantum dot . 48

4.2 Modelling of the Hxc potentials with asymmetric couplings 51

II Non-Equilibrium Density Functional Theory 57

5 Steady-state Density Functional Theory Formalism for Electronic Transport with Finite Thermal Gradients 59
5.1 i-DFT for finite temperature gradients . . . 60
5.1.1 Reverse engineering of the SIAM xc potentials for finite thermal gradient . . . 61
5.2 Transport coefficients . . . 66
5.2.1 Electrical conductance . . . 66
5.2.2 Seebeck Coefficient . . . 67
5.2.3 Thermal conductance . . . 73

6 Steady-state Density Functional Theory Formalism for both Electrical and Heat Transport 77
6.1 Formalism . . . 78
6.1.1 Kohn-Sham equations of iq-DFT . . . 81
6.2 Linear Response . . . 83
6.3 Application to the single impurity Anderson Model . . . 86
6.3.1 Reverse engineering from the Many-Body Model . . . 87
6.3.2 Numerical results . . . 91

7 Non-Equilibrium Spectral functions with Multi-Terminal Steady-State Density Functional Theory 95
7.1 Non-Equilibrium Spectral functions from multi-terminal i-DFT . . . 96
7.2 i-DFT potentials for the Anderson model . . . 100
7.2.1 Results . . . 103

8 Conclusions 107

Appendices

A Basic exchange-correlation functionals from model Hamiltonians 113
A.1 Single Site Model . . . 113
A.2 Single Impurity Anderson Model . . . 115
A.3 Constant Interaction Model . . . 118

B Analytic expressions for the transport integrals in the Single Impurity Anderson Model 121

References 125

List of Abbreviations

CB	**C**oulomb **B**lockade
CIM	**C**onstant **I**nteraction **M**odel
DFT	**D**ensity **F**unctional **T**heory
DQD	**D**ouble **Q**uantum **D**ot
GCE	**G**rand **C**anonical **E**nsemble
i-DFT	Steady-State **D**ensity **F**unctional **T**heory for electrical transport
iq-DFT	Steady-State **D**ensity **F**unctional **T**heory for electrical and thermal transport
KS	**K**ohn-**S**ham
LB	**L**andauer-**B**üttiker
MBM	**M**any-**B**ody **M**odel
NEGF	**N**on-**E**quilibrium **G**reen **F**unctions
NRG	**N**umerical **R**enormalization **G**roup
QD	**Q**uantum **D**ot
QMC	**Q**uantum **M**onte **C**arlo
RE	**R**everse **E**ngineering
SIAM	**S**ingle **I**mpurity **A**nderson **M**odel
SSM	**S**ingle **S**ite **M**odel
STM	**S**canning **T**unneling **M**icroscopy
TDDFT	**T**ime **D**ependent **D**ensity **F**unctional **T**heory
WBL	**W**ide **B**and **L**imit

List of Publications

1 . Sobrino, N., D'Agosta, R., & Kurth, S. (2019). Steady-state density functional theory for thermoelectric effects. Physical Review B, 100(19), 195142.

2 . Kurth, S., Jacob, D., Sobrino, N., & Stefanucci, G. (2019). Nonequilibrium spectral functions from multiterminal steady-state density functional theory. Physical Review B, 100(8), 085114.

3 . Toranzo, I. V., Puertas-Centeno, D., Sobrino, N., & Dehesa, J. S. (2020). Analytical Shannon information entropies for all discrete multidimensional hydrogenic states. International Journal of Quantum Chemistry, 120(2), e26077.

4 . Sobrino, N., Kurth, S., & Jacob, D. (2020). Exchange-correlation potentials for multiorbital quantum dots subject to generic density-density interactions and Hund's rule coupling. Physical Review B, 102(3), 035159.

5 . Sobrino, N., Eich, F., Stefanucci, G., D'Agosta, R., & Kurth, S. (2021). Thermoelectric transport within density functional theory. Physical Review B, 104(12), 125115.

6 . Dehesa, J. S., & Sobrino, N. (2021). Complexity-like properties and parameter asymptotics of $\mathfrak{L}_q$-norms of Laguerre and Gegenbauer polynomials. Journal of Physics A: Mathematical and Theoretical (accepted).

7 . Sobrino, N., & Dehesa, J. S. (2021). Algebraic $\mathfrak{L}_q$-norms and complexity-like properties of Jacobi polynomials-Degree and parameter asymptotics. arXiv preprint arXiv:2110.11441.

1 Introduction

Quantum mechanics is a fundamental theory for the description of the microscopic properties of matter. The evolution of the quantum state of the system of interest can in principle be obtained by solving the many-body Schrödinger equation. Although the procedure is conceptually straightforward, it becomes computationally really demanding as the number of particles in the problem increases. During the last decades, Density functional theory (DFT) has become the most popular method for an ab-initio description of matter, from atoms, to molecules and solids [1–3] due to its favorable balance of accuracy and numerical efficiency [4–6]. The fundamental theorems of DFT establish that, for a given (static) external potential, there is a unique many-body ground state density which can alternatively be completely determined by solving the one-electron Schrödinger equation of an effective non-interacting system. The price to paid is in the so-called exchange-correlation (xc) potential, a functional of the density which has to be approximated.

The foundation theorems of DFT shown that the universal xc functional exists, making DFT a formally exact theory. In practice, the form of the universal functional is unknown, but many different approximations have been developed in the last 60 years. This led to a wide variety of successful applications of DFT to many different problems in physics and chemistry [7–9], particularly for the prediction of the structure and thermodynamic properties of molecules and solids [10]. Nevertheless,

there are some physical situations where standard approximations fail at properly describing the ground state density of the system, e.g., for the case of so-called strongly correlated systems. Several authors have contributed towards a progress in the description of such systems from a DFT perspective [11–18] although the lack of DFT functionals with the correct features (in particular for ab-initio calculations) led to a combination of DFT with other many-body approaches for the correct description of the strongly correlated physics [19–22]. In this direction, model Hamiltonians serve as a perfect basic scenario to study these systems, since the full control of the interaction parameters together with the low computational effort paves the way to understand the exact properties which the corresponding DFT xc functionals must have [23–26].

While the original ground state DFT formulation has been extremely successful for the computation of structural properties, there are many important issues which extend beyond its reach. Most notably, time-dependent processes and excited-state properties of electronic systems either are not included at all or are not easily accessible. This motivated the development of the time dependent version of DFT, namely TDDFT [2, 27, 28], which gives access to the non-equilibrium time-dependent density. Moreover, it also gives access to the excitation energies of a many-electron system [2, 28, 29].

In principle, TDDFT is a proper framework for the study of electronic transport of a biased system both in the time domain but also in the steady-state. In TDDFT the steady-state is achieved in the long-time limit of the time evolution of the system after switching on a DC bias. Within TDDFT, one can hope to describe the (longitudinal) part of the electronic (steady) current. However, in practice it turns out to be difficult to construct (ultra-nonlocal) TDDFT functionals correctly describing transport [30–33]. For the additional description of heat (or energy) current, the formalism has been extended recently [34–36], but applications have so far been restricted to non-interacting systems [37] due to the lack of approximations to the corresponding xc functionals.

Another widely used framework for steady-state electronic transport combines DFT with the Landauer-Büttiker approach (LB+DFT) [38–40]. This LB+DFT formalism, also known as DFT+NEGF (DFT plus Non-equilibrium Green Functions), treats transport as a scattering problem of non-interacting electrons. The resulting Landauer formula for the electronic current is physically very intuitive in that the current is given as energy integral of the transmission function integrated over the bias window. The LB+DFT framework has become extremely useful in a qualitative understanding of transport through, e.g., single molecules. However, one should keep in mind that the non-interacting nature of electrons in LB+DFT clearly is an approximation. As a consequence, the connection between quantities of the real system and those calculated within the LB+DFT framework is typically nontrivial and strong corrections may appear [41, 42]. Furthermore, LB+DFT uses ground state (equilibrium) DFT in a non-equilibrium situation (transport) which is formally not justified. Formally, the long-time limit of TDDFT leads to exchange-correlation (xc) corrections to the bias [30–33, 43, 44] which are absent in LB+DFT but are difficult to model.

Recently, an alternative DFT approach to transport in the steady-state was proposed [41]. This so-called i-DFT formalism allows to compute the steady-state density and electronic current (and thus the electrical conductance). Again, just like in TDDFT, this is achieved via an xc contribution to the bias. Unlike in TDDFT, however, xc functionals have been constructed for non-trivial model systems such as the single impurity Anderson model (SIAM), both in the Kondo as well as in the Coulomb blockade (CB) regime [45]. Also, in TDDFT the exact xc functional has memory dependence [3, 46–50] whereas the i-DFT xc functionals only depends on the steady-state values of the density and the current.

Thermoelectricity [51] is at the heart of a range of technological applications, e.g., energy conversion, and is intrinsically related to both charge and heat transport. With progress in the manipulation and fabrication of new materials at the nanoscale and even at the level of single molecules [52–56]), designing more efficient thermoelectrics requires reliable modeling techniques at an atomistic level.

This thesis concerns about the correct description of both steady-state electrical as well as the electronic contribution to heat transport within DFT. In part I we will explore the equilibrium properties of the xc functionals for the description of multi-orbital systems in the limit of low temperatures, with special attention to strong correlations. Before introducing the transport setup, in chapter 3 we will consider the thermodynamical equilibrium situation of impurities in contact with a particle bath and arbitrary interactions among them. This statistical ensemble correctly describes the density in the system in a simple form, and will allow us to reverse engineer the exact properties that the functionals must have. Then, in chapter 4 we will consider the LB+DFT approach for the description of the electrical conductance in a double quantum dot. We will propose different functionals able to accurately reproduce the abrupt transitions in the local occupations of the dots when the coupling to the electrodes is different in each dot.

The methodological developments for the non-equilibrium transport problem within DFT will be the focus of part II. In chapter 5 we will generalize the i-DFT framework to the situation when there is a temperature gradient across the junction. This extension will allow us to describe the correct linear Seebeck coefficient of the many-body system and accurate functionals for both the CB and Kondo regime for the SIAM will be parametrized. The main contribution of this thesis is addressed in chapter 6 where we will introduce a formally exact theory for the description of electrical and thermal transport (driven by electrons) in the steady-state within a DFT framework. In the linear response regime, this theory will give us access to all the transport coefficients, quantities of great interest in thermoelectric materials due to their technological applications [57–59]. As a first illustrative application of the framework we will parametrize the required xc contributions for the transport coefficients in the CB for the SIAM. Finally in chapter 7 we will show how to extract the non-equilibrium spectral function of a molecular junction at both zero and finite temperature within i-DFT by considering a three-terminal setup in the limit of vanishing coupling to one of the electrodes (ideal STM limit). This general result

will be applied to the SIAM and the related xc functionals will be constructed, allowing us to partially capture the splitting of the Kondo peak under finite bias.

2
Theoretical Background

Contents

2.1 Equilibrium Density Functional Theory 7
2.2 Non-Equilibrium Density Functional Theory: Steady-State Transport 13
2.2.1 Landauer-Büttiker+DFT 13
2.2.2 Steady-state density functional theory for finite bias conductances 16
2.3 Lattice Hamiltonians 18

In this chapter we will introduce the theory on which the fundamental pillars of this work are built. First, the principles of the equilibrium density functional theory are presented at zero and finite temperature. Then, the general framework is applied in the context of steady-state electronic transport, i.e., a non-equilibrium problem. Two different approaches will be introduced in this context, namely, the Landauer-Büttiker+DFT and the i-DFT formalism.

2.1 Equilibrium Density Functional Theory

The foundations of the DFT turn back to 1964 when the seminal paper [60] by Hohenberg and Kohn provided the fundamental theorems showing that the

Thomas-Fermi model (see [61]) may be regarded as an approximation to an exact theory for ground states densities.

Hohenberg-Kohn Theorem

The Hohenberg-Kohn theorem proofs that time-independent many-particle systems (under the application of local, spin-independent external potentials) at $T = 0$K can be fully characterized by the ground state density.

Let us consider the non-relativistic time-independent Hamiltonian of a system of N interacting electrons

$$\hat{H} = \hat{T} + \hat{V} + \hat{W} \tag{2.1}$$

that can be written in second quantized notation in the form (atomic units are used throughout)

$$\begin{aligned}\hat{H} = &-\frac{1}{2}\sum_{\sigma}\int d^3r\hat{\psi}^{\dagger}_{\sigma}(\mathbf{r})\nabla^2\hat{\psi}_{\sigma}(\mathbf{r}) + \sum_{\sigma}\int d^3r\hat{\psi}^{\dagger}_{\sigma}(\mathbf{r})v(\mathbf{r})\hat{\psi}_{\sigma}(\mathbf{r}) \\ &+\frac{1}{2}\sum_{\sigma,\sigma'}\int d^3r\int d^3r'\hat{\psi}^{\dagger}_{\sigma}(\mathbf{r})\hat{\psi}^{\dagger}_{\sigma'}(\mathbf{r}')w(\mathbf{r},\mathbf{r}')\hat{\psi}_{\sigma'}(\mathbf{r}')\hat{\psi}_{\sigma}(\mathbf{r})\end{aligned} \tag{2.2}$$

where $\hat{\psi}^{\dagger}_{\sigma}(\mathbf{r})$ ($\hat{\psi}_{\sigma}(\mathbf{r})$) is the field operator which describes the creation (annihilation) of one particle with spin σ at position $\mathbf{r}$. The usual choice for the two-particle interaction is the Coulomb repulsion $w(\mathbf{r},\mathbf{r}') = |\mathbf{r}-\mathbf{r}'|^{-1}$, but other interactions are allowed.

The single-particle probability density of the electronic ground state is given by ($\mathbf{x}_j \equiv (\mathbf{r}_j, \sigma_j)$)

$$n_0(\mathbf{r}) = N\sum_{\sigma}\int d\mathbf{x}_2\cdots\int d\mathbf{x}_N|\Psi_0(\mathbf{r},\sigma,\mathbf{x}_2,\ldots,\mathbf{x}_N)|^2, \tag{2.3}$$

where the N-particle wave function $\Psi_0(\mathbf{r},\sigma,\mathbf{x}_2,\ldots,\mathbf{x}_N)$ is the lowest energy eigenstate (ground state) of the static Schrödinger equation $\hat{H}\Psi_0(\mathbf{x}_1,\mathbf{x}_2,\ldots,\mathbf{x}_N) = E_0\Psi_0(\mathbf{x}_1,\mathbf{x}_2,\ldots,\mathbf{x}_N)$.

Since the ground state density of eq. (2.3) is obtained from the wave function, which in turn is obtained from the Hamiltonian, we can deduce that the ground

state density is a functional of the external potential $v(\mathbf{r})$. We define the map $\mathcal{A}$ between the set $\mathcal{V}$ of external potentials which differ by more than a constant

$$\mathcal{V} = \{v \mid \text{corresponding } \Psi_0 \text{ exists and} \\ \text{non-degenerate, } v'(\mathbf{r}) \neq v(\mathbf{r} + \text{const})\}, \tag{2.4}$$

and the set $\mathcal{X}$ of resulting ground states

$$\mathcal{X} = \{\Psi_0 \mid \Psi_0 \text{ ground state corresponding to } v_0 \in \mathcal{V} \text{ and} \\ \Psi_0 = e^{i\phi}\Psi_0 \text{ with } \phi \text{ being some global phase}\}. \tag{2.5}$$

We also define the map $\mathcal{B}$ between the set $\mathcal{X}$ and the set $\mathcal{N}$ of all ground state densities obtained from some element of $\mathcal{X}$

$$\mathcal{N} = \{n_0 \mid n_0(\mathbf{r}) \text{ fullfills eq. (2.3) with } \Psi_0 \in \mathcal{X}\}. \tag{2.6}$$

We can easily see that these maps are surjective by construction. Hohenberg and Kohn demonstrated by *reductio ad absurdum* that the maps $\mathcal{A}$ and $\mathcal{B}$ are also injective (one to one) and therefore bijective, which implies that the maps can be fully inverted. This allows to state the following theorem:

Hohenberg-Kohn Theorem: For an N-electron interacting system with given particle-particle interaction, there exists a one-to-one correspondence between the external potential $v(\mathbf{r})$ and the ground state density $n_0(\mathbf{r})$, i.e., the external potential is a unique functional of the ground state density, $v[n_0](\mathbf{r})$, up to an arbitrary additive constant.

The original proof was restricted to non-degenerate ground state densities, but the generalization to degenerate ground states is straightforward [62].

Two corollaries related to the total energy functional are extracted from the theorem. First, since the wave function is a functional of the density $\psi = \psi[n]$, any ground state observable is a density functional, i.e., $O[n] := \langle\psi[n]|\,\hat{O}\,|\psi[n]\rangle$. In particular, the ground state energy can be expressed as the sum of a universal functional and the external potential contribution

$$E_v[n] = \langle\Psi[n]|\,\hat{H}\,|\Psi[n]\rangle = F[n] + \int d^3r v(\mathbf{r})n(\mathbf{r}), \\ F[n] := \langle\Psi[n]|\,\hat{T} + \hat{W}\,|\Psi[n]\rangle = T[n] + W[n], \tag{2.7}$$

where $F[n]$ is *universal* in the sense that it is the same for any N-electron system with the same electron-electron interaction, independently of what external potential is acting on it. On the other hand, as a consequence of the Rayleigh-Ritz principle, for any fixed external potential $v_0(\mathbf{r})$, the ground state energy takes its minimum value for the ground state density $n_0(\mathbf{r})$ corresponding to this external potential

$$E_{v_0}[n] \geq E_{v_0}[n_0]. \tag{2.8}$$

The ground state density can be found from the Euler equation

$$\mu = v(\mathbf{r}) + \frac{\delta F[n]}{\delta n[\mathbf{r}]}, \tag{2.9}$$

where μ is the Lagrange multiplier associated with the constraint $\int n(\mathbf{r})d\mathbf{r} = N$

Kohn-Sham Equations

In 1965, Kohn and Sham [63] realized that one can use an effective single-particle picture of non-interacting particles to transform DFT into a practical scheme to calculate the ground state properties of systems of interacting particles. If we rewrite the total energy functional of eq. (2.7) by adding and subtracting non-interacting terms (in the following represented by a s subscript)

$$\begin{aligned} E_{v_0}[n] =& T_s[n] + \int d^3r\, n(\mathbf{r})v_0(\mathbf{r}) + E_{\mathrm{H}}[n] + E_{\mathrm{xc}}[n], \\ E_{\mathrm{H}}[n] =& \frac{1}{2}\int d^3r \int d^3r' \frac{n(\mathbf{r})n(\mathbf{r}')}{|\mathbf{r}-\mathbf{r}'|}, \\ E_{\mathrm{xc}}[n] =& T[n] - T_s[n] + W[n] - \frac{1}{2}\int d^3r \int d^3r' \frac{n(\mathbf{r})n(\mathbf{r}')}{|\mathbf{r}-\mathbf{r}'|}, \end{aligned} \tag{2.10}$$

one observes that the density variational principle of the interacting system is equivalent to the variational principle of the non-interacting system with the potential

$$v_s[n](\mathbf{r}) = v_0(\mathbf{r}) + \int d^3r' \frac{n(\mathbf{r}')}{|\mathbf{r}-\mathbf{r}'|} + v_{\mathrm{xc}}[n](\mathbf{r}), \tag{2.11}$$

where the xc potential is defined as

$$v_{\mathrm{xc}}[n](\mathbf{r}) = \frac{\delta E_{\mathrm{xc}}[n]}{\delta n(\mathbf{r})}. \tag{2.12}$$

This implies that the ground state density of any *interacting* system can be obtained by solving the one electron Schrödinger equation

$$\hat{H}_s(\mathbf{r})\phi_j(\mathbf{r}) = \epsilon_j\phi_j(\mathbf{r}), \tag{2.13}$$

where $\hat{H}_s(\mathbf{r}) = \left(-\frac{\nabla^2}{2} + v_s[n](\mathbf{r})\right)$, and the ground state density is related to the single-particle wave functions through

$$n_0(\mathbf{r}) = \sum_{j=1}^{N} |\phi_j(\mathbf{r})|^2. \tag{2.14}$$

Eqs. (2.11) to (2.14) are the *Kohn-Sham equations*. In practice, eq. (2.13) is solved through a self-consistent procedure: We first need to provide an approximation for the xc potential eq. (2.12) to calculate the single-particle wave functions and thereafter the density, which in turn is used to update the Kohn-Sham Hamiltonian $\hat{H}_s(\mathbf{r})$. This procedure is repeated until the self-consistency between the old and updated ground state density is reached.

In the last decades, many different approximations for $v_{\mathrm{xc}}[n]$ have been developed [64]. The most popular approximations are the Local-Density Approximation (LDA), whose energy functional depends solely upon the value of the electronic density at each point in the space, and the Generalized-Gradient Approximation (GGA) [65] based functionals, where the non-homogeneity of the true electron density is captured due to te explicit dependence of the energy functional on the gradient of the density.

Equilibrium Finite Temperature Density Functional Theory

In 1965 D. Mermin presented a seminal paper [66] where he extended the Hohenberg and Kohn approach to nonzero temperatures. He considered the grand canonical ensemble (GCE) at fixed temperature T and proof that there is a one-to-one correspondence between the external potential $v(\mathbf{r})$ and the equilibrium density. Furthermore, he derived the analogous corollaries at finite temperature for the grand potential Ω. To show this, it is used a minimum property of the grand potential analogous to that of the ground state energy. If

$$\Omega[\hat{\rho}] = \mathrm{Tr}\left[\hat{\rho}\left(\hat{H} - \mu\hat{N} + T\log\hat{\rho}\right)\right] \tag{2.15}$$

then the grand canonical potential,

$$\Omega = -\frac{1}{\beta} \ln \mathrm{Tr}\left[e^{-\beta(\hat{H}-\mu\hat{N})}\right] \tag{2.16}$$

is given by $\Omega[\hat{\rho}]$ where $\beta = 1/T$ and $\hat{\rho}$ is the grand canonical density matrix (statistical operator)

$$\hat{\rho} = \frac{e^{-\beta(\hat{H}-\mu\hat{N})}}{Z} = \frac{1}{Z}\sum_m e^{-\beta(E_m-\mu N_m)} \left|m\right\rangle \left\langle m\right| \tag{2.17}$$

with $Z = \mathrm{Tr}[e^{-\beta(\hat{H}-\mu\hat{N})}]$ is the GCE partition function. The $|m\rangle$ are the many-body eigenstates of the system and E_m the corresponding eigenenergies, i.e. $\hat{H}\left|m\right\rangle = E_m \left|m\right\rangle$. Therefore the density in the GCE reads

$$n = \mathrm{Tr}[\hat{\rho}\,\hat{n}] = \frac{1}{Z}\sum_m \left\langle m\right| \hat{n} \left|m\right\rangle e^{-\beta(E_m-\mu N_m)}. \tag{2.18}$$

The functional 2.15 satisfies [66]

$$\Omega[\hat{\rho}] \geq \Omega[\hat{\rho}_0]. \tag{2.19}$$

To show the one-to-one correspondence between the external potential and the equilibrium density, Mermin considered two different potentials leading to the same density with different Hamiltonians, density matrices and grand potentials. The comparison between eq. (2.15) for both systems leads to a contradiction which directly implies that only one $v(\mathbf{r})$ can result in a given $n(\mathbf{r})$. Therefore, since $n(\mathbf{r})$ uniquely determines $v(\mathbf{r})$ which in turn determines $\hat{\rho}$, the entire equilibrium density matrix $\hat{\rho}$ is a functional of $n(\mathbf{r})$. In particular

$$\mathcal{F}[n(\mathbf{r})] = \mathrm{Tr}\left[\hat{\rho}\left(\hat{T} + \hat{W} + \frac{1}{\beta}\ln\hat{\rho}\right)\right] \tag{2.20}$$

can be taken to be a functional of the density alone with a universal form valid for all $v(\mathbf{r})$. For a given potential $v(\mathbf{r})$, we define the functional

$$\Omega_v[n] = \int d^3r\, v(\mathbf{r})n(\mathbf{r}) + \mathcal{F}[n(\mathbf{r})]. \tag{2.21}$$

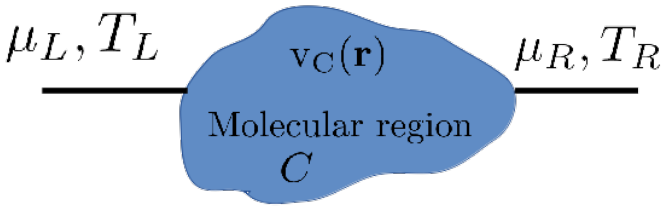

Figure 2.1: Schematic illustration of the quantum transport setup.

When $n_0(\mathbf{r})$ is the correct equilibrium density in the potential v_0, then $\Omega_{v_0}[n_0]$ equals the grand potential Ω. If $n(\mathbf{r})$ is the equilibrium density associated with any other potential $v(\mathbf{r})$, then

$$\Omega_v[n(\mathbf{r})] \geq \Omega_{v_0}[n_0(\mathbf{r})] \tag{2.22}$$

This completes the generalization of the basic theorems of Hohenberg and Kohn to finite temperature.

2.2 Non-Equilibrium Density Functional Theory: Steady-State Transport

In the present section we will generalize the DFT to study steady-state transport, a particular situation of the Time-Dependent DFT (TDDFT) [3] after the transient dynamics disappear in the long time evolution of the system. A general approach for electronic transport within DFT will be introduced, the Landauer-Büttiker approach. The success and failures of the theory will be discussed and subsequently the steady-state DFT framework for electronic transport (i-DFT) will be presented as a promising alternative to study molecular junctions out of equilibrium.

2.2.1 Landauer-Büttiker+DFT

The description of coherent transport of nano-electronic devices requires a full quantum mechanical description that accounts for the wave-like nature of electrons. The development of the theory started already in the 1950s [39, 67] and was extended in particular in the 1980s and early 1990s [38, 68].

We consider the transport setup as depicted in fig. 2.1, where a molecular central region that characterizes the physical properties of the system is coupled to two metallic leads (also called electrodes) at chemical potentials μ_α and temperatures T_α with $\alpha = L, R$, which serve as sink or reservoirs of electrons, smoothly connected to the central region in order to avoid back-scattering due to the contacts. Under the application of a finite DC-bias across the junction $V = V_L - V_R$ the system is brought out of equilibrium, leading to a finite steady-state current.

The description of this system from a DFT perspective requires the self-consistent solution of the Kohn-Sham (KS) equations 2.13. Given that the system is neither finite nor periodic, the transport problem is conveniently formulated in terms of the non-equilibrium Green functions (NEGF), the resulting LB+DFT formalism is also known with the acronym DFT+NEGF.

We introduce a localized orthonormal and complete single-particle basis $|jq\rangle$ where j denotes an atomic site and q labels the different basis functions localized at this site [15]. In the Green's functions language the problem consists of solving the equation

$$((\omega + \mathrm{i}\eta)\mathbb{I} - \boldsymbol{\mathcal{H}}_s)\,\boldsymbol{\mathcal{G}}(\omega) = \mathbb{I} \tag{2.23}$$

with $\eta \to 0^+$. In eq. (2.23) $\boldsymbol{\mathcal{H}}_s$ represents the KS Hamiltonian in the introduced localized basis

$$\boldsymbol{\mathcal{H}}_s = \begin{bmatrix} \mathbf{H}_{LL} & \mathbf{H}_{LC} & 0 \\ \mathbf{H}_{CL} & \mathbf{H}_{CC} & \mathbf{H}_{CR} \\ 0 & \mathbf{H}_{RC} & \mathbf{H}_{RR} \end{bmatrix} \tag{2.24}$$

where $\mathbf{H}_{\alpha\alpha'}$ is the matrix element connecting the regions α and α' ($\alpha, \alpha' \in \{L, C, R\}$). The Green's function can be expressed as

$$\boldsymbol{\mathcal{G}}(\omega) = \begin{bmatrix} \mathbf{G}_{LL}(\omega) & \mathbf{G}_{LC}(\omega) & \mathbf{G}_{LR}(\omega) \\ \mathbf{G}_{CL}(\omega) & \mathbf{G}_{CC}(\omega) & \mathbf{C}_{CR}(\omega) \\ \mathbf{G}_{RL}(\omega) & \mathbf{G}_{RC}(\omega) & \mathbf{G}_{RR}(\omega) \end{bmatrix}. \tag{2.25}$$

Now solving eq. (2.23) for $\mathbf{G}_{CC}$ we find

$$\mathbf{G}(\omega) := \mathbf{G}_{CC}(\omega) = ((\omega + \mathrm{i}\eta)\mathbb{I}_C - \mathbf{H}_{CC} - \boldsymbol{\Sigma}_L(\omega) - \boldsymbol{\Sigma}_R(\omega))^{-1} \tag{2.26}$$

where $\mathbf{\Sigma}_\alpha(\omega) = \mathbf{\Sigma}^{eq}_\alpha(\omega - V_\alpha)$ is the (retarded) embedding self energy for lead α and

$$\mathbf{\Sigma}^{eq}_\alpha(\omega) = \mathbf{H}_{C\alpha}\left((\omega + \mathrm{i}\eta)\mathbb{I}_\alpha - \mathbf{H}_{\alpha\alpha}\right)^{-1}\mathbf{H}_{\alpha C} \tag{2.27}$$

the equilibrium contribution. The central block of the steady-state density matrix $\boldsymbol{\rho}$ can be obtained through the following equation [69]

$$\boldsymbol{\rho} = 2\sum_{\alpha=L,R}\int \frac{d\omega}{2\pi} f(\omega - V_\alpha)\mathbf{G}(\omega)\mathbf{\Gamma}_\alpha(\omega)\mathbf{G}^\dagger(\omega), \tag{2.28}$$

where the broadening matrix

$$\mathbf{\Gamma}_\alpha(\omega) = \mathrm{i}\left(\mathbf{\Sigma}_\alpha(\omega) - \mathbf{\Sigma}^\dagger_\alpha(\omega)\right). \tag{2.29}$$

From the density matrix we can calculate the electronic density according to

$$n(\mathbf{r}) = \sum_{jq,j'q'} \rho_{jq,j'q'}\langle jq|\mathbf{r}\rangle\langle\mathbf{r}|j'q'\rangle = 2\sum_{\alpha=L,R}\int\frac{dw}{2\pi} f(\omega - V_\alpha)A_{\alpha,s}(\mathbf{r},\omega), \tag{2.30}$$

with

$$A_{\alpha,s}(\mathbf{r},\omega) = \sum_{jq,j'q'}\left[\mathbf{A}_{\alpha,s}(\omega)\right]_{jq,j'q'}\langle jq|\mathbf{r}\rangle\langle\mathbf{r}|j'q'\rangle, \tag{2.31}$$

and

$$\mathbf{A}_{\alpha,s}(\omega) = \mathbf{G}(\omega)\mathbf{\Gamma}_\alpha(\omega)\mathbf{G}^\dagger(\omega) \tag{2.32}$$

is the partial KS spectral function. The KS spectral function is then defined as $\mathbf{A}_s(\omega) = \sum_\alpha \mathbf{A}_{\alpha,s}(\omega)$. Given that the (non-interacting) Green's functions depend on the Hxc potential (through the dependence of the Hamiltonian) and this depends on the density, eq. (2.30) defines a self-consistent problem. The number of electrons in the central region C can directly be obtained from the density

$$N = \int_C d^3\mathbf{r}\, n(\mathbf{r}) = 2\sum_{\alpha=L,R}\int\frac{d\omega}{2\pi} f(\omega - v_{\alpha,s})\mathrm{Tr}[\mathbf{A}_{\alpha,s}(\omega)]. \tag{2.33}$$

Once the ground state density is obtained, one can calculate the steady-state electrical current in the present formalism using the famous Landauer-Büttiker formula

$$I_s = 2\int\frac{d\omega}{2\pi}\left(f(\omega - V_L) - f(\omega - V_R)\right)\mathrm{Tr}\Big[\mathbf{G}(w)\mathbf{\Gamma}_L(\omega)\mathbf{G}^\dagger(\omega)\mathbf{\Gamma}_R(\omega)\Big]. \tag{2.34}$$

The subscript s in I_s emphasizes the fact that the calculated current from eq. (2.34) corresponds to the current of the KS system. From the previous definition of the electrical current we can calculate the KS zero-bias conductance

$$G_s = \left.\frac{\partial I_s}{\partial V}\right|_{V=0} = -2\int \frac{d\omega}{2\pi} f'(\omega)\mathrm{Tr}\Big[\mathbf{G}(\omega)\mathbf{\Gamma}_L(\omega)\mathbf{G}^{\dagger}(\omega)\mathbf{\Gamma}_R(\omega)\Big]. \tag{2.35}$$

The LB+DFT approach is widely used in ab-initio calculations to describe transport through nanoscale systems, considering transport as a scattering process of non-interacting electrons where the KS potential is used as the scattering potential. Nevertheless, it presents one inconvenience: although it provides a path to calculate the exact equilibrium density of the molecular junction (assuming the correct Hxc functional is provided), the electrical current obtained (and therefore the electrical conductance) is only a good approximation to the many-body one when the interaction effects are small.

2.2.2 Steady-state density functional theory for finite bias conductances

In 2015 the steady-state density functional theory for finite bias conductances [41] (i-DFT) was introduced. The main idea behind the theory consists of provide a formal basis for a DFT based steady-state transport theory.

The foundation of i-DFT is the one-to-one correspondence between the pair of the external potential in the central region C and the applied bias through the junction $(v(\mathbf{r}), V)$ and the related density in the region C and the electrical current across the junction $(n(\mathbf{r}), I)$ through the following theorem:

Theorem: For any finite temperature and fixed external potentials in the leads, the map $(v(\mathbf{r}), V) \to (n(\mathbf{r}), I)$ is invertible in a finite bias window around equilibrium, i.e., we have $v(\mathbf{r}) = v[n, I](\mathbf{r})$ and $V = V[n, I]$.

To prove the theorem [41] it is enough to show that the Jacobian of the system is non-vanishing. We do not explicitly show the proof in the present section, but some generalizations with their corresponding proofs will be shown in the following

chapters[1]. Since the Jacobian of the system is a continuous function around equilibrium, there exists a finite interval out of equilibrium where the theorem holds.

However, it is important to note that the proof goes through independent of the form of the interaction, in particular also for no interaction at all. Suppose that we have the pair $(n(\mathbf{r}), I)$ of interacting steady-state "densities" corresponding to the pair of potentials $(v(\mathbf{r}), V)$. If we assume that these "densities" are non-interacting representable, i.e., that they can be reproduced through the pair of potentials $(v_s(\mathbf{r}), V_s)$ of a *non-interacting* system, then we can define the xc potentials of the theory

$$v_{\mathrm{Hxc}}[n, I](\mathbf{r}) = v_s[n, I](\mathbf{r}) - v[n, I](\mathbf{r}), \tag{2.36}$$

$$V_{\mathrm{xc}}[n, I] = V_s[n, I] - V[n, I]. \tag{2.37}$$

For given potentials $(v(\mathbf{r}), V)$, the KS equations of i-DFT which allow to reproduce the interacting densities from effectively non-interacting equations, then read

$$n(\mathbf{r}) = 2\int \frac{dw}{2\pi}\left(f(w - \frac{V + V_{\mathrm{xc}}[n, I]}{2})A_{L,s}(\mathbf{r}, w) + f(w + \frac{V + V_{\mathrm{xc}}[n, I]}{2})A_{R,s}(\mathbf{r}, w)\right), \tag{2.38a}$$

$$I = 2\int \frac{dw}{2\pi}\left(f(w - \frac{V + V_{\mathrm{xc}}[n, I]}{2}) - f(w + \frac{V + V_{\mathrm{xc}}[n, I]}{2})\right)T_s(w), \tag{2.38b}$$

where the KS spectral function has been defined in eq. (2.31) and the transmission function $T(w) = \mathrm{Tr}\Big[\mathbf{G}(w)\mathbf{\Gamma}_L(w)\mathbf{G}^\dagger(w)\mathbf{\Gamma}_R(w)\Big]$. Eqs. (2.38) are formally equivalent to the ones from the LB+DFT approach (eqs. (2.30) and (2.34)) with the difference that the dependence on the bias has been replaced by the KS bias $V_s = V + V_{\mathrm{xc}}$. Given that both v_{Hxc} and V_{xc} depend on the two basic variables, eqs. (2.38) define a self-consistent problem of two coupled equations. Notice that in the i-DFT framework, the steady-state current obtained from eq. (2.38b) corresponds now to the correct many-body quantity (assuming that the correct pair of xc functionals is provided). As a direct consequence, upon linearization of this equation the exact

[1] In chapter 5 the theorem will be extended for situations in presence of a thermal gradient. In chapter 6 the theorem will be generalized to include the description of the heat current in multiple terminals situations.

many-body electrical conductance can be expressed from i-DFT; the inclusion of the xc bias leads to the electrical conductance of te interacting system expressed purely in terms of i-DFT accessible quantities

$$G = \frac{G_s}{1 - G_s \left.\frac{\partial V_{\rm xc}}{\partial I}\right|_{I=0}}, \tag{2.39}$$

where G_s corresponds to the KS conductance defined in eq. (2.35).

2.3 Lattice Hamiltonians

In this section some particular models will be introduced to highlight the different results obtained for the transport quantities. In particular, the xc correction for the bias within i-DFT will allow to describe the many-body physics of the Coulomb Blockade regime, where the LB+DFT fails even when providing the exact $v_{\rm Hxc}$ functional.

Our interest will be focus on the study of model Hamiltonians describing impurities or quantum dots (QD) in a transport setup. In this thesis we will study lattice models of systems of $\mathcal{M}$ impurities. A Hamiltonian of a system with two-body interactions and on-site energy, attached to $\mathcal{N}$ semi-infinite leads in the steady-state, can be written in second quantization as

$$\hat{H} = \hat{H}_{\rm dot} + \hat{H}_{\rm leads} + \hat{H}_{\rm coupling}, \tag{2.40}$$

$$\begin{aligned}\hat{H}_{\rm dot} = &\sum_{i}^{\mathcal{M}}\sum_{\sigma} v_{i\sigma}\hat{n}_{i\sigma} + \sum_{i}^{\mathcal{M}} U_i \hat{n}_{i\uparrow}\hat{n}_{i\downarrow} - t\sum_{i}^{\mathcal{M}}\sum_{\sigma}\left(\hat{d}^{\dagger}_{i\sigma}\hat{d}_{i+1\sigma} + H.c.\right) \\ &- \sum_{i<j}\sum_{\sigma} J_{ij}\left[\hat{n}_{i\sigma}\hat{n}_{j\sigma} + \hat{d}^{\dagger}_{i\sigma}\hat{d}_{i\bar{\sigma}}\hat{d}^{\dagger}_{j\bar{\sigma}}\hat{d}_{j\sigma}\right] + \sum_{i<j} U'_{ij}\hat{n}_i\hat{n}_j,\end{aligned} \tag{2.41}$$

$$\hat{H}_{\rm leads} = \sum_{\alpha}^{\mathcal{N}}\sum_{k}\sum_{\sigma}(\epsilon_{\alpha k\sigma} + V_\alpha)\hat{c}^{\dagger}_{\alpha k\sigma}\hat{c}_{\alpha k\sigma}, \tag{2.42}$$

$$\hat{H}_{\rm coupling} = \sum_{\alpha}^{\mathcal{N}}\sum_{k}\sum_{\sigma}\sum_{i}^{\mathcal{M}}\left(t_{\alpha k}\hat{c}^{\dagger}_{\alpha k\sigma}\hat{d}_{i\sigma} + H.c.\right), \tag{2.43}$$

where $d_{i\sigma}$ ($d^{\dagger}_{i\sigma}$) are the annihilation (creation) operators for orbital i and spin σ, $\hat{n}_{i\sigma}$ is the number operator and $\hat{n}_i = \hat{n}_{i\uparrow} + \hat{n}_{i\downarrow}$. The corresponding operators $\hat{c}_{\alpha\sigma}$ ($\hat{c}^{\dagger}_{\alpha\sigma}$) for the lead α are defined in an analogous way. The first three terms in eq. (2.41) describe the one-electron contributions to the impurities, where $v_{i\sigma}$ is

the on-site energy (or gate potential) of an electron with spin σ in the orbital i, U_i is the intra-Coulomb repulsion between electrons in the orbital i and t is the hopping between electrons in adjacent orbitals. The first term in the second line corresponds to the Hund's rule coupling contribution, which has been split into the density-density contribution and the spin-flip contribution. The last term in the second line is the inter-Coulomb repulsion U'_{ij}. The eq. (2.42) account for the single-particle eigenstates as well as the bias V_α contributions of the isolated leads and eq. (2.43) holds for the tunneling Hamiltonian between the dot and the leads with couplings $\Gamma_\alpha(w) := 2\pi \sum_k |t_{\alpha k}|^2 \delta(w - \epsilon_{\alpha k})$. We consider featureless electronic leads described by frequency-independent couplings $\Gamma_\alpha(w) = \gamma_\alpha$, i.e., we work in the wide band limit (WBL).

In the following, we will specify three relevant models (extracted from the lattice Hamiltonian introduced above) which will be studied in the following chapters.

Single Site model

Our first model for a quantum dot consists of a single level with on-site energy v which can hold up to two electrons [70]. The corresponding Hamiltonian has the form

$$\hat{H}^{\mathrm{SSM}} = v\hat{n} + U\hat{n}_\uparrow\hat{n}_\downarrow. \tag{2.44}$$

Despite its simplicity, this model is useful to highlight certain aspects of strong electronic correlation.

The exact equilibrium density of the system in the GCE can be derived from eq. (2.18)

$$n(v) = \frac{1}{Z}\mathrm{Tr}\left[e^{-\beta\hat{H}^{\mathrm{SSM}}}\hat{n}\right] = \frac{2\left[e^{-\beta v} + e^{-\beta(2v+U)}\right]}{1 + 2e^{-\beta v} + e^{-\beta(2v+U)}}. \tag{2.45}$$

The exact spectral function for the SSM has the form

$$A(w) = \left(1 - \frac{n}{2}\right)\delta(w - v) + \frac{n}{2}\delta(w - v - U). \tag{2.46}$$

Therefore, for the KS system we can combine eq. (2.30) and eq. (2.46) (for $U = 0$) leading to the simple expression of the ground state density

$$n(v_s) = 2f(v_s). \tag{2.47}$$

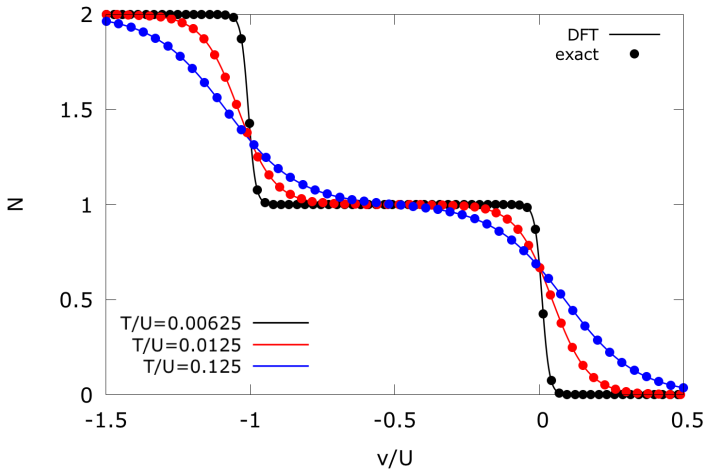

Figure 2.2: Total occupation of the SSM as function of the gate potential for different temperatures and strong correlations $U = 8$. The solid line corresponds to DFT (eq. (2.47)) and dots to the exact result (eq. (2.45))

In appendix A eq. (2.45) and eq. (2.47) are used to analytically invert the exact xc functional for the SSM.

In fig. 2.2 the total occupation of the SSM is presented as function of the gate level for different temperatures and strong correlations $U = 8$. One can appreciate the presence of a plateau at $n = 1$ for low temperatures. This feature appears due to the shifting in energy that the Coulomb interaction produces in the following available state. The DFT result by construction matches the exact density eq. (2.45) when the Hxc functional eq. (A.3) is used.

Single Impurity Anderson Model

The Single Impurity Anderson Model (SIAM) is the minimal model for the description of transport through a correlated system [45]. It is obtained by coupling the SSM with a pair of electrodes (with energy independent tunneling rate $1/\gamma$). The corresponding Hamiltonian takes the form

$$\hat{H}^{\mathrm{SIAM}} = v\hat{n} + U\hat{n}_\uparrow\hat{n}_\downarrow + \sum_{\alpha,k,\sigma}(\epsilon_{\alpha k\sigma} + V_\alpha)\hat{c}^\dagger_{\alpha k\sigma}\hat{c}_{\alpha k\sigma} + \sum_{\alpha,k,\sigma}\left(t_{\alpha k}\hat{c}^\dagger_{\alpha k\sigma}\hat{d}_\sigma + H.c.\right) \quad (2.48)$$

where $\alpha = L, R$ for the left and right electrodes. In the following chapters, except when stated explicitly, we will consider energy independent couplings (wide Band Limit) as well as symmetric coupling of the leads, i.e., $\gamma_L = \gamma_R = \gamma/2$.

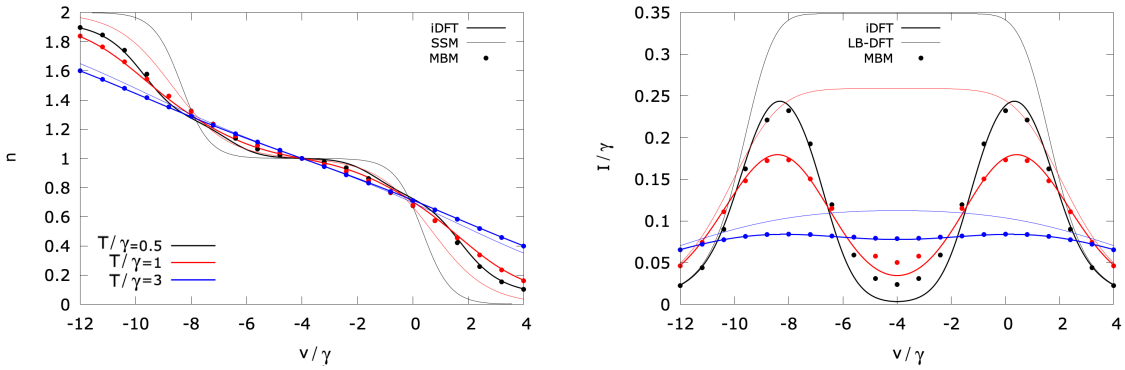

Figure 2.3: Left: Total occupation comparison between i-DFT (using the xc functionals eqs. (A.17) and (A.18)), MBM and SSM (using eq. (A.3)). Right: Steady-state current comparison between i-DFT, LB+DFT and MBM. In both figures $V/\gamma = 3$ and $U/\gamma = 8$.

In order to calculate the ground state density and the steady electrical current of the SIAM, we consider the following many-body model (MBM) for the spectral function [15, 71] which correctly describes the impurity coupled to the leads in the CB regime

$$A(\omega) = \left(1 - \frac{n}{2}\right) \frac{\gamma}{(\omega - v)^2 + \frac{\gamma^2}{4}} + \frac{n}{2} \frac{\gamma}{(\omega - v - U)^2 + \frac{\gamma^2}{4}}. \tag{2.49}$$

Eq. (2.49) can be viewed as the generalization of the SSM spectral function eq. (2.46) where the delta peaks are broadened due to the effect of the couplings. The MBM spectral function eq. (2.49) together with the interacting equations

$$n = 2 \int d\omega \left(f(\omega - V_L) + f(\omega - V_R)\right) A(\omega) \tag{2.50a}$$

$$I = \gamma \int d\omega \left(f(\omega - V_L) - f(\omega - V_R)\right) A(\omega) \tag{2.50b}$$

will produce the reference results in the range of temperatures $T/\gamma > 1$. For the KS system, n and I can be obtained using eqs. (2.38a) and (2.38b) together with the non-interacting spectral function

$$A_s(w) = \frac{\gamma}{(w - v_s)^2 + \frac{\gamma^2}{4}}. \tag{2.51}$$

In the left panel of fig. 2.3 the total occupation of the SIAM is compared with the SSM. The MBM reference result for the SIAM is presented to benchmark the accuracy of the xc functionals used (eqs. (A.17) and (A.18)). While the SIAM

occupation shows two new steps around $v = 0, -U$ as the temperature is decreased, the SSM density only matches the regime when the temperatures are large compared to the coupling, where the steps vanish. In the right figure the steady-state electrical current from i-DFT is compared with the one obtained from LB+DFT (using the SSM functional eq. (A.3)) and the MBM. While the i-DFT and MBM show the two peak structure that characterizes the CB regime (which is a hallmark of strong correlations), the LB+DFT completely neglects this feature, showing a plateau centered at the particle-hole symmetric point instead. Only when the effect of the interaction is small, i.e., when the impurity is almost empty or full, the LB+DFT agrees with the many-body result.

Constant Interaction Model

The last relevant model of our interest is the Constant Interaction Model (CIM) consisting of a series of $\mathcal{M}$ impurities that can be coupled or not to the electrodes. The Hamiltonian of the system reads

$$\begin{aligned}\hat{H}^{\mathrm{CIM}} =& \sum_{i}^{\mathcal{M}} v_i \hat{n}_i + \sum_{i}^{\mathcal{M}} U \hat{n}_{i\uparrow}\hat{n}_{i\downarrow} + \sum_{i<j} U \hat{n}_i \hat{n}_j \\ &+ \sum_{\alpha,k,\sigma} \epsilon_{\alpha k\sigma} \hat{c}^{\dagger}_{\alpha k\sigma}\hat{c}_{\alpha k\sigma} + \sum_{\alpha,k,\sigma} \left(t_{\alpha k} \hat{c}^{\dagger}_{\alpha k\sigma}\hat{d}_{\sigma} + H.c. \right). \end{aligned} \tag{2.52}$$

This system can be seen as a generalization of the SIAM for multiple-levels where the Coulomb repulsion between the electrons is constant. In the disconnected situation (last two terms of eq. (2.52) vanish) the resulting model is a generalization of the SSM. In this case, the many-body problem is solved for a given set of gates v_i. The resulting set of eigenstates and corresponding energies determines the densities n_i in the GCE according to eq. (2.18).

For the non-interacting system, the density is simply determined by the gate $v_{i,s}$ of a non-interacting QD and is thus simply given by the Fermi-Dirac distribution

$$n_i = 2f(v_{i,s}). \tag{2.53}$$

Since the non-interacting spectral function is $A_s(w) = \delta(w - v_s)$.

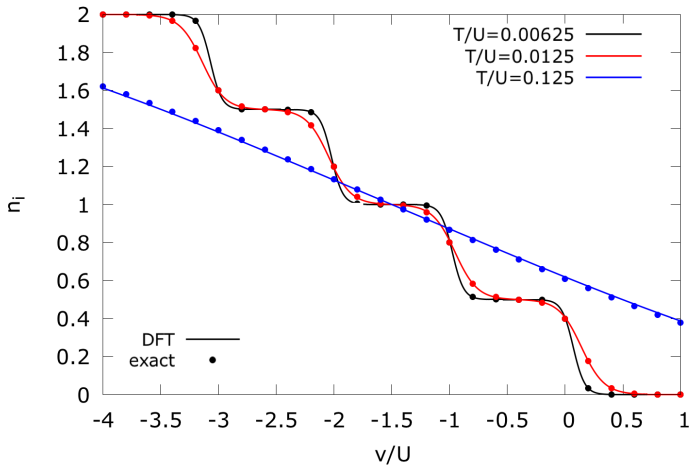

Figure 2.4: Densities of the uncontacted CIM as function of the gate potential ($v = v_1 = v_2$) for different temperatures in units of the Coulomb repulsion $U = U'$. The solid line corresponds to DFT (eq. (A.22)) and dots to the numerical exact result.

In fig. 2.4 the density $n_i = n_1 = n_2$ of the uncontacted CIM in the case $\mathcal{M} = 2$ is presented as function of the gate level for different temperatures in units of the Coulomb repulsion. The DFT functional eq. (A.22) derived in appendix A allows to obtain an excellent agreement with the exact result eq. (2.18) where the main features are the steps at integer total occupation $N = n_1 + n_2$ due to the effect of the Coulomb repulsion.

Part I

Equilibrium Density Functional Theory

This chapter is based on the article [72].

3 Multi-orbital Quantum Dots

Contents

3.1 Modelling of the Hxc potentials 28
3.1.1 Hxc potentials and link to stability diagrams for the double quantum dot at low temperatures 28
3.1.2 Decomposition of the interaction into basic building blocks 34
3.1.3 Generalization of Hxc potential to more than two orbitals 38
3.2 Results 39
3.2.1 Results for the double quantum dot 41
3.2.2 Results for more than two orbitals 45

In this chapter the Hxc potentials for the multi-orbital quantum dot subject to generic density-density interactions and Hund's rule coupling are derived and compared with reverse engineering of exact solutions. The study of stability diagrams also sheds light on the properties of the Hxc potentials.

We start by considering a particular case of Eq. (2.40) for the non-contacted multi-orbital quantum dot. The Hamiltonian of the system takes the form

$$\begin{aligned}\hat{H} =& \sum_i v_i \hat{n}_i + \sum_i U_i \, \hat{n}_{i\uparrow}\hat{n}_{i\downarrow} + \sum_{i<j} U_{ij} \, \hat{n}_i \hat{n}_j \\ & - \sum_{i<j,\sigma} J_{ij} \, \left[\hat{n}_{i\sigma}\hat{n}_{j\sigma} + \left(c^\dagger_{i\sigma} c_{i\bar{\sigma}} \, c^\dagger_{j\bar{\sigma}} c_{j\sigma}\right)\right]. \end{aligned} \tag{3.1}$$

This kind of Hamiltonian is very common in the fields of strongly correlated electrons and mesoscopic physics, as it provides a natural description of 3d- or 4f-shells of

transition metal or lanthanide impurities in metallic hosts and of multi-orbital quantum dots. In these systems density-density interactions and Hund's rule coupling are by far the most important interactions. In particular the role of the latter has become a focus of intense research in the field of strongly correlated electrons in the last years[73].

3.1 Modelling of the Hxc potentials

Here we work at (typically small) finite temperature T and consider the GCE as the proper statistical ensemble to describe the density matrix of the system in thermodynamical equilibrium with a heat and particle bath, allowing to interchange particles with the sites through the gate potentials v_i. Therefore, the equilibrium density n_i is obtained via eq. (2.18), i.e., $n_i = n_i(v_1, \ldots, v_{\mathcal{M}})$, which can (numerically) be inverted to give $v_i = v_i(n_1, \ldots, n_{\mathcal{M}})$. For the KS system, the density is simply described by the Fermi function eq. (2.53) which can easily be inverted as $v_{s,i} = v_{s,i}(n_i) = 2T \log \frac{2}{n_i} - 1$. The properties of the Hxc functionals $v_{\mathrm{Hxc,i}} = v_{s,i}(n_i) - v_i(n_1, \ldots, n_{\mathcal{M}})$ can then be studied by exploring the parameter space $v = (v_1, \ldots, v_{\mathcal{M}})$ which allows to establish the density-potential mapping for the entire space of densities $n = (n_1, \ldots, n_{\mathcal{M}})$ (for $n_i \in [0, 2]$).

3.1.1 Hxc potentials and link to stability diagrams for the double quantum dot at low temperatures

We now focus on the two-orbital case, i.e. a double quantum dot (DQD) with generic density-density interactions (U_1, U_2, U_{12}). For the time being we only investigate cases with vanishing Hund's rule coupling, i.e., $J_{i,j} = 0$. Here [72] we are interested in the qualitative structure of the Hxc potentials, in particular in the positions (and heights) of step structures which appear in the low-temperature limit. In fact, these steps are not only the crucial but also the *only* features of the Hxc potential in the limit of low temperatures. In this section we will show how these step structures can be deduced completely from the stability diagrams.

A stability diagram highlights the occupations (densities) of the ground states in the different regions of the plane of external gates v_1 and v_2. The position and shape of these regions in the v_1-v_2 plane depend on the values of the interaction parameters but within each region the pair of densities (n_1, n_2) remains constant at (close to) zero temperature and the possible values of these local densities are $n_i \in \{0, 1, 2\}$. Each of the nine pairs of densities (n_1, n_2) (corresponding to a finite region in the stability diagram) corresponds to a single point which we call a vertex in the n_1-n_2 plane.

It turns out that the positions of the steps which characterize the Hxc potentials in the n_1-n_2 plane can be obtained from the stability diagram by connecting the vertices corresponding to density regions which are adjacent in the v_1-v_2 plane. The heights of these steps can also be extracted from the stability diagram. Below we will illustrate how this works presenting some representative examples and we will also explain the physical reasons behind our observations.

We have identified three different regions for the interaction parameters where qualitative changes both in the stability diagram as well as in the Hxc potentials occur. These are Regime I ($U_{12} < U_1, U_2$), Regime II ($U_1 < U_{12} < (U_1 + U_2)/2$) and Regime III ($U_1 \leq (U_1 + U_2)/2 \leq U_{12}$) where it is assumed without loss of generality that $U_1 \leq U_2$.

As a first example we choose the Regime I, where the corresponding stability diagram is shown in panel (d) of fig. 3.1 with $U_1 = 2.5U_{12}$, $U_2 = 3U_{12}$. Here the regions corresponding to the different possible ground state densities (given in parenthesis) are marked by different colors. The RE Hxc potentials for orbitals 1 and 2 are shown in panels (e) and (f) of fig. 3.1, respectively. In the stability diagram, the domain corresponding to the occupation $(0, 0)$ is directly adjacent only to the domains with occupations $(1, 0)$ and $(0, 1)$. If we connect the $(0, 0)$ vertex with one of those vertices in the n_1-n_2 plane we see that the resulting lines run along the border of the allowed density domain. The complete set of lines along the borders of the density domain follow from the sequence of vertices $(0, 0) \to (1, 0) \to (2, 0)$, $(0, 0) \to (0, 1) \to (0, 2)$, $(2, 0) \to (2, 1) \to (2, 2)$, and $(0, 2) \to (1, 2) \to (2, 2)$. The other possibilities of connecting vertices corresponding to adjacent regions in

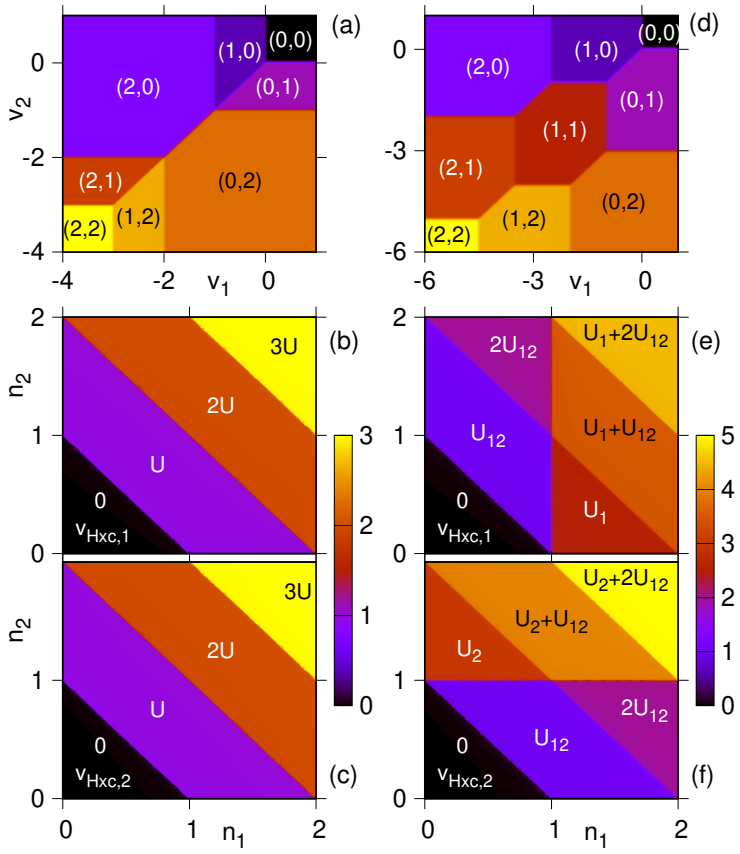

Figure 3.1: Panels (a)-(c) (constant interaction model, CIM): stability diagram (a) and Hxc potentials for orbitals 1 and 2 (panels (b) and (c), respectively) of the double quantum dot for $U_1 = U_2 = U_{12}$. Panels (d)-(f) (Regime I): stability diagram (d) and Hxc potentials for orbitals 1 and 2 (panels (e) and (f), respectively) of the double quantum dot for $U_1 = 2.5U_{12}$, $U_2 = 3U_{12}$. All energies in units of smallest interaction (U_{12}).

the $v_1 - v_2$ plane are (i) $(1,0) \rightarrow (0,1)$, (ii) $(1,0) \rightarrow (1,1)$, (iii) $(1,1) \rightarrow (1,2)$, (iv) $(2,0) \rightarrow (1,1)$, $(v)(1,1) \rightarrow (0,2)$, (vi) $(2,1) \rightarrow (1,2)$, (vii) $(0,1) \rightarrow (1,1)$ and (viii) $(1,1) \rightarrow (2,1)$. These lines are exactly the position of the steps in the Hxc potentials, see panels (e) and (f) of fig. 3.1. Notice that for some fixed v_1 the vertices $(1,0) \rightarrow (1,1) \rightarrow (2,1)$ lead to the step at $n_1 = 1$ for $v_{\mathrm{Hxc},1}$ while for some fixed v_2 the vertices $(0,1) \rightarrow (1,1) \rightarrow (1,2)$ lead to the step at $n_2 = 1$ in $v_{\mathrm{Hxc},2}$. This is the main difference with respect to the $v_{\mathrm{Hxc,i}}$ of the CIM, panels (b) and (c) of fig. 3.1.

The height of these steps can also be deduced from the stability diagram as schematically illustrated in fig. 3.2 : the length of the projection of the degenerate lines connecting regions in the abscissa (ordinate) gives the height of the step connecting these vertices in the $v_{\mathrm{Hxc},1}$ ($v_{\mathrm{Hxc},2}$). We begin by looking at the regions

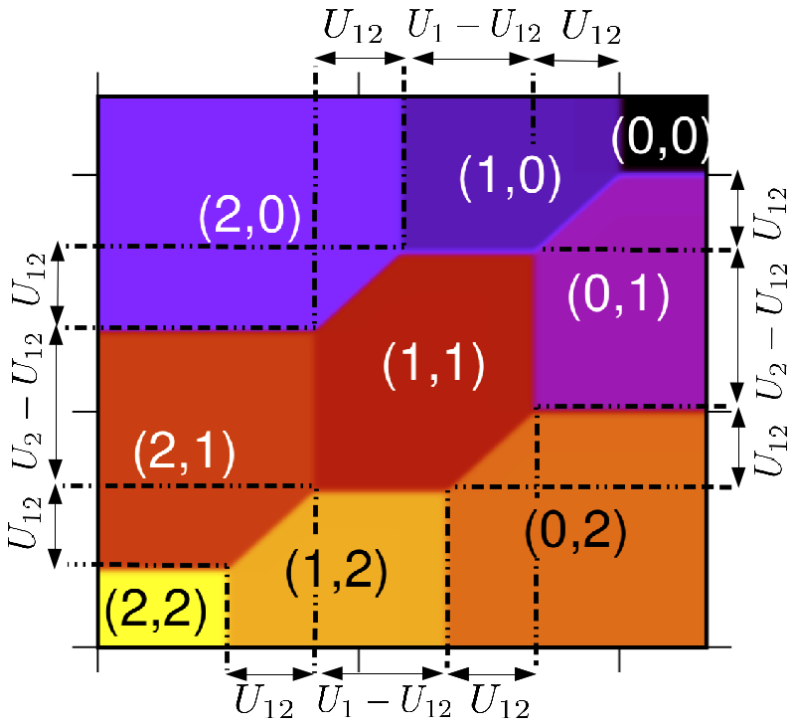

Figure 3.2: Stability diagram of Regime I of the DQD for $U_1 = 2.5U_{12}$, $U_2 = 3U_{12}$. The length of the projection of the degenerate lines connecting regions are explicitly shown. These values exactly correspond to the height of the steps connecting these regions in the Hxc potential. The projections on the abscissa give the steps heights in $v_{\mathrm{Hxc},1}$ and on the ordinate give the steps heights in $v_{\mathrm{Hxc},2}$.

with occupations $(1,0)$ and $(0,1)$. The corresponding states are degenerate along the line $v_1 = v_2$ and for $-U_{12} < v_1 < 0$ they are the ground states of the double dot. For the KS system to reproduce this density for external potentials $v_1 = v_2$ in the same interval, we need the KS potentials on both orbitals to be pinned to the Fermi energy. Therefore both Hxc potentials need to exhibit a step of height U_{12} along the line connecting the vertices $(1,0)$ and $(0,1)$. The regions $(1,0)$ and $(1,1)$ are adjacent along the line $v_2 = -U_{12}$ for $-U_1 < v_1 < -U_{12}$ and thus the KS potential of the first orbital needs to be pinned to the Fermi energy for this range of v_1 leading to a step of height $U_1 - U_{12}$ along the line connecting the $(1,0)$ and $(1,1)$ vertices for $v_{\mathrm{Hxc},1}$ (see fig. 3.2). Similarly, $v_{\mathrm{Hxc},2}$ needs to exhibit a step of height $U_2 - U_{12}$ along the line connecting the $(0,1)$ and $(1,1)$ vertices. Next, the regions $(2,0)$ and $(1,1)$ are adjacent for $-U_{12} - U_i < v_i < -U_i$ $(i = 1,2)$ and therefore both Hxc potentials have a step of height U_{12} along the lines connecting the $(2,0)$ and $(1,1)$ vertices.

Similarly, there also has to be a step of height U_{12} in both Hxc potentials along the line connecting the $(0,2)$ and $(1,1)$ vertices. The regions $(1,1)$ and $(1,2)$ are adjacent for $-2U_{12} < v_1 < -U_1 - U_{12}$ leading to a step of height $U_1 - U_{12}$ in $v_{\mathrm{Hxc},1}$ along the line $(1,1) \to (1,2)$. Similarly, there is a step of height $U_2 - U_{12}$ in $v_{\mathrm{Hxc},2}$ along the $(1,1) \to (2,1)$ line. Finally, the regions $(2,1)$ and $(1,2)$ are adjacent along a line of length U_{12} leading to a step of this height in both Hxc potentials along the $(2,1) \to (1,2)$ line. In this way we now have completely determined the (low temperature) Hxc potentials of both orbitals just by analyzing the stability diagram. The overall structure of the $v_{\mathrm{Hxc,i}}$ is such that they exhibit steps for integer total occupation $N = n_1 + n_2$ for both Hxc potentials plus an additional step at $n_i = 1$ for $v_{\mathrm{Hxc,i}}$. Note also that for the special case $U_{12} = 0$ only the steps at $n_i = 1$ for $v_{\mathrm{Hxc,i}}$ survive while those at integer N disappear. This is not surprising since in this case our model just describes two completely independent single impurities and, naturally, the corresponding Hxc potential for orbital i is completely independent of the other orbital and given by the Hxc potential of a SSM with interaction strength U_i. This has also been discussed as "intra-system steps" in ref. [74].

A particular relevant situation of the Regime I is the CIM, when all the parameter interactions are equal $U_1 = U_2 = U_{12}$. The stability diagram and corresponding Hxc potentials are shown in panel (a-c) of Fig. 3.1.

For the Regime II and Regime III the inter-orbital interaction U_{12} is smaller than at least one of the intra-orbital ones. In panels (a)-(c) of fig. 3.3 we show the stability diagram and Hxc potentials for interaction parameters chosen in Regime II. Compared to Regime I (panels (d)-(f) of fig. 3.1), in the stability diagram we now find that there exists a range of potentials for which regions $(2,0)$ and $(0,1)$ are directly adjacent and, similarly, for the regions $(2,1)$ and $(0,2)$. As expected, these transitions lead to the new steps in the Hxc potentials. On the other hand, for the Hxc potential of orbital 1 the step at $n_1 = 1$ (present in Regime I) now disappears while in $v_{Hxc,2}$ the step at $n_2 = 1$ survives (this step is related to the vertical lines delimiting the $(1,1)$ region in the stability diagram). We have annotated the plateau

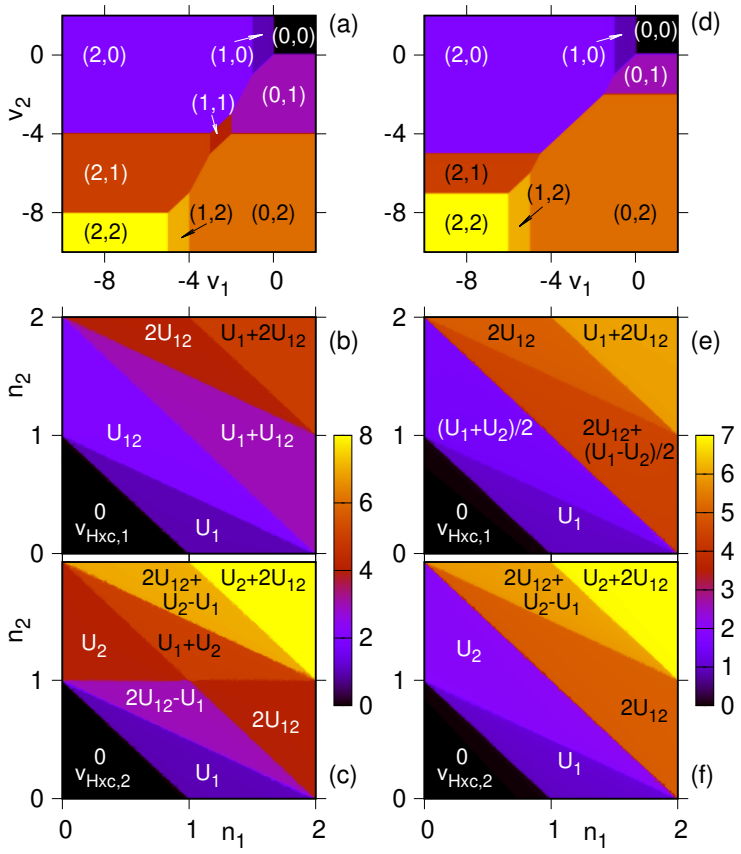

Figure 3.3: Panels (a)-(c) (Regime II): stability diagram (a) and Hxc potentials for orbitals 1 and 2 (panels (b) and (c), respectively) of the double quantum dot for $U_2 = 4U_1$ and $U_{12} = 2U_1$. Panels (d)-(f) (Regime III): stability diagram (d) and Hxc potentials for orbitals 1 and 2 (panels (e) and (f), respectively) of the double quantum dot for $U_2 = 2U_1$, and $U_{12} = 2.5U_1$. All energies in units of the smallest interaction (U_1).

values in both Hxc potentials which can be found by analyzing the stability diagram using similar arguments to the ones used above for Regime I.

Finally, in panels (d)-(f) of fig. 3.3 we show the stability diagram and Hxc potentials for interaction parameters chosen in Regime III. Compared to Regime II, the main qualitative difference is the disappearance of the step at $n_2 = 1$ in the Hxc potential of orbital 2. Again, all the step structures in the Hxc potentials can fully be deduced by analyzing the stability diagram.

3.1.2 Decomposition of the interaction into basic building blocks

In the following we show that the Hxc potentials of (uncontacted) multi-orbital quantum dots for generic density-density interactions can be built from a few basic potentials. We start with the Regime I where the corresponding Hxc potential shows steps at integer values of $N = n_1 + n_2$, connected to a CIM potential, as well as steps at $n_1 = 1$ for orbital 1 or at $n_2 = 1$ for orbital 2 connected to a SSM potential of the corresponding orbital. We can rationalize this idea by a decomposition of the Coulomb interaction term as follows. Rewriting the inter-orbital repulsion as

$$U_{12}\,\hat{n}_1\,\hat{n}_2 = \frac{U_{12}}{2}\hat{N}(\hat{N}-1) - U_{12}\sum_i \hat{n}_{i\uparrow}\hat{n}_{i\downarrow}, \tag{3.2}$$

we can split the interaction $\mathcal{V}_{int} = \sum_i U_i\,\hat{n}_{i\uparrow}\hat{n}_{i\downarrow} + U_{12}\,\hat{n}_1\hat{n}_2$ into a CIM part and two SSM interactions (one for each orbital):

$$\mathcal{V}_{int} = \frac{1}{2}U_{12}\,\hat{N}(\hat{N}-1) + \sum_i \delta U_i\,\hat{n}_{i\uparrow}\hat{n}_{i\downarrow} \tag{3.3}$$

where $\delta U_i \equiv U_i - U_{12}$ is the "excess interaction" for each orbital. This suggests to write the Hxc potential for level i for Regime I ($U_{12} \leq U_1, U_2$) as the sum of the CIM Hxc potential for interaction U_{12} and the SSM potential for δU_i:

$$v^{\text{Reg I}}_{\text{Hxc},i}[\boldsymbol{n}] = v^{\text{CIM}}_{\text{Hxc}}(U_{12})[N] + v^{\text{SSM}}_{\text{Hxc}}(\delta U_i)[n_i], \tag{3.4}$$

where $v^{\text{CIM}}_{\text{Hxc}}$ and $v^{\text{SSM}}_{\text{Hxc}}$ are the xc potentials of eq. (A.23) and eq. (A.3), respectively. For the Regime II and Regime III (U_{12} is larger than at least one of the intra-orbital interactions U_i) this decomposition of the Coulomb interaction leads to negative interactions δU_i in the SSM parts. Since the step in the Hxc potential of the SSM at $n_i = 1$ would actually vanish for negative interactions [75], in this regimes the step structure can not be rationalized by eq. (3.4). Indeed the structure of the RE Hxc potentials (fig. 3.3) appears to be quite different from that for the regime $U_{12} \leq U_i$. Essentially, two new features are found in this situation: (i) an increase of the step height at $N = 2$ with respect to the CIM potential, and (ii)

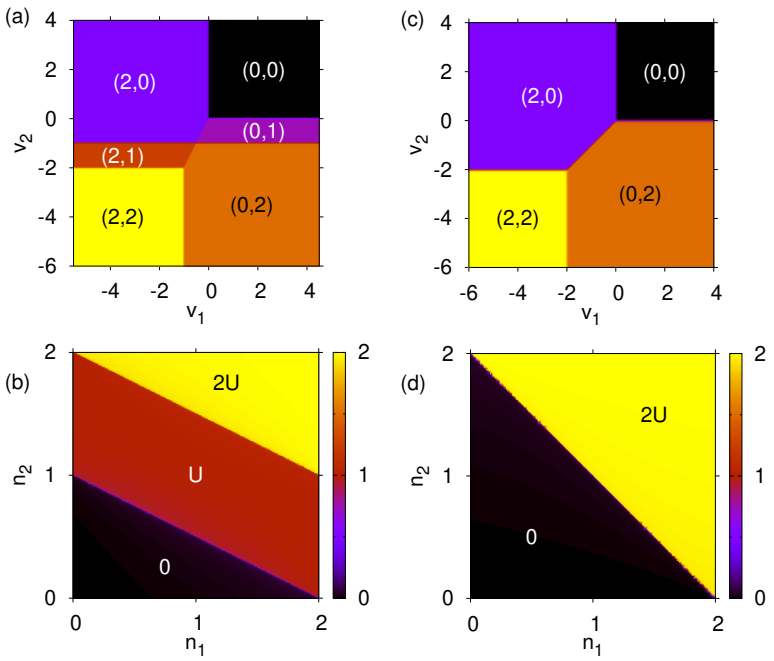

Figure 3.4: Stability diagram (a) and Hxc potential of orbital 2 (b) for the Skew interaction $\mathcal{V}_{\text{skew}} = \frac{U}{2}\hat{n}_2(\hat{N}-1)$. The structure of the Hxc potential for orbital 1 is the same as for orbital 2 but the step heights are half those of orbital 2 (0, $U/2$, U). Stability diagram (c) and Hxc potential of both orbitals (d) for the inter-orbital interaction $\mathcal{V}_{\text{inter}} = U\hat{n}_1\hat{n}_2$. All energies in units of U in both cases.

peculiar new steps at integer values of $n_1/2 + n_2$. The steps at integer $n_1/2 + n_2$ are generated by a peculiar interaction of the form

$$\mathcal{V}_{\text{skew}} = \frac{U}{2}\hat{n}_2(\hat{N}-1) \tag{3.5}$$

which we will refer to as *Skew interaction* from now on. This interaction is realized by setting $U_1 = 0$ and $U_{12} = U_2/2 = U/2$. The corresponding stability diagram and the Hxc potential for orbital 2 is shown in fig. 3.4. Note that the Hxc potential of orbital 1 has the same structure but the step heights are lower by a factor of 1/2.

Common to all cases is that there is always a contribution of the CIM potential, as long as all interactions (U_1, U_2, U_{12}) remain finite. From our observations we make the assumption that this contribution is given by the smallest interaction. Subtracting the CIM interaction $\sim U_1$ from the total interaction thus yields:

$$\mathcal{V}_{int} - \frac{U_1}{2}\hat{N}(\hat{N}-1) = (U_{12}-U_1)\,n_1 n_2 + (U_2-U_1)\,n_{2\uparrow}n_{2\downarrow} \tag{3.6}$$

Hence the remaining interaction consists of an inter-orbital interaction $\sim (U_{12} - U_1)$ and a SSM interaction $\sim (U_2 - U_1)/2$ for orbital 2. These two terms can be combined to yield the Skew interaction and a remaining term.

Given that we require the interactions to be positive, for the Regime II we use the relation $\hat{n}_1\hat{n}_2 = \hat{n}_2(\hat{N}-1) - 2\hat{n}_{2\uparrow}\hat{n}_{2\downarrow}$ to rewrite the excess of interaction eq. (3.6) as

$$(U_{12} - U_1)\,\hat{n}_2\,(\hat{N}-1) + 2(U_{\text{ave}} - U_{12})\,\hat{n}_{2\uparrow}\hat{n}_{2\downarrow}. \tag{3.7}$$

Overall this suggests the following decomposition of the Hxc potential in Regime II ($U_1 < U_{12} < U_{\text{ave}}$):

$$\begin{aligned} v_{\text{Hxc,i}}^{\text{Reg II}}[\boldsymbol{n}] =& v_{\text{Hxc}}^{\text{CIM}}(U_1)[N] + v_{\text{Hxc,i}}^{\text{skew}}\left(2(U_{12}-U_1)\right)[\boldsymbol{n}] \\ &+ v_{\text{Hxc}}^{\text{SSM}}\left(2(U_{\text{ave}}-U_{12})\right)[n_2]\,\delta_{i,2} \end{aligned} \tag{3.8}$$

where $\delta_{i,2}$ is the Kronecker-delta which ensures that the SSM term only contributes to the Hxc potential of orbital 2. Note that as $U_{12}\to U_{\text{ave}}$ the SSM term vanishes.

On the other hand Regime III occurs when the inter-orbital interaction exceeds the average intra-orbital interaction, i.e. $U_{12} > U_{\text{ave}} > U_1$. We use the relation $\hat{n}_{2\uparrow}\hat{n}_{2\downarrow} = \frac{1}{2}\left(\hat{n}_2(\hat{N}-1) - \hat{n}_1\hat{n}_2\right)$ to rewrite the excess of interaction 3.6 as

$$\frac{U_2 - U_1}{2}\,\hat{n}_2\,(\hat{N}-1) + (U_{12} - U_{\text{ave}})\,\hat{n}_1\hat{n}_2. \tag{3.9}$$

Eq. (3.9) corresponds to a Skew interaction (eq. (3.5)) and a pure inter-orbital interaction part. As can be seen in fig. 3.4(d), this inter-orbital term

$$\mathcal{V}_{\text{inter}} = U\hat{n}_1\hat{n}_2 \tag{3.10}$$

gives rise to a single step at $N = 2$ which explains the increase in step height at $N = 2$ with respect to the CIM, observed in Fig. 3.3(e,f). Overall this suggests the following decomposition of the Hxc potential in Regime III ($U_{12} > U_{\text{ave}} > U_1$):

$$\begin{aligned} v_{\text{Hxc,i}}^{\text{Reg III}}[\boldsymbol{n}] =& v_{\text{Hxc}}^{\text{CIM}}(U_1)[N] + v_{\text{Hxc,i}}^{\text{skew}}(U_2 - U_1)[\boldsymbol{n}] \\ &+ v_{\text{Hxc}}^{\text{inter}}(U_{12} - U_{\text{ave}})[N]. \end{aligned} \tag{3.11}$$

We can see that for $U_1 = U_2$ the Skew part of the Hxc potential disappears.

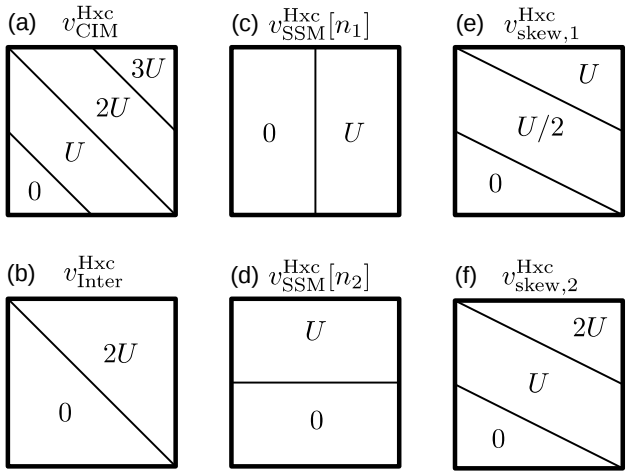

Figure 3.5: Schematic representation of the four basic Hxc potentials for building the generic potentials for all three regimes. (a) Hxc potential for CIM interaction $\frac{U}{2}\hat{N}(\hat{N}-1)$. (b) Hxc potential for inter-orbital interaction Un_1n_2. (c,d) Hxc potential for intra-orbital (i.e. SSM) interactions $Un_{i\uparrow}n_{i\downarrow}$. (e,f) Hxc for the Skew interaction $\frac{U}{2}\hat{n}_2(\hat{N}-1)$.

Hence we have found a decomposition of the Hxc potential for a two-orbital model with generic (density-density) interactions in all three regimes in terms of four basic potentials which are shown schematically in fig. 3.5. We would like to emphasize at this point that Regime I corresponds to a more natural choice of parameters than the other two regimes, since the inter-orbital interaction U_{12} is generally smaller than any of the intra-orbital interactions U_i. Nevertheless, the other regimes might be realized by effective models or possibly by screening of the Coulomb interactions.

So far we have neglected the effect of Hund's rule coupling on the Hxc potentials. In fig. 3.6 we show the stability diagram and the corresponding RE Hxc potential for the case of a CIM type direct interaction part ($U_1 = U_2 = U_{12}$) plus the full Hund's coupling contribution (J_H). Both the stability diagram and the RE Hxc potential shown in fig. 3.6 resemble the ones for the case with $U_{12} < U_i$ without Hund's coupling (fig. 3.1(d-f)). Only the size of the vertex regions changes in the stability diagram, and correspondingly in the Hxc potentials only the step heights change. Moreover, by switching off the spin-flip term in the Hamiltonian we find that it does not have any effect on the densities and consequently on the Hxc potentials and thus can be neglected. Hence in the following considerations we

only need to take into account the density-density part of the Hund's coupling in (next to last term in eq. (3.1)).

We can rewrite the density-density part of the Hund's rule coupling term in terms of a (negative) CIM interaction and (positive) SSM interactions for the remaining orbitals plus a remaining *positive* interaction part:

$$\begin{aligned}\mathcal{V}_H &= -J_H \sum_\sigma \hat{n}_{1\sigma}\hat{n}_{2\sigma} = -J_H \hat{n}_1\hat{n}_2 + J_H \sum_\sigma \hat{n}_{1\sigma}\hat{n}_{2\bar{\sigma}} \\ &= -\frac{J_H}{2}\hat{N}(\hat{N}-1) + J_H \sum_i \hat{n}_{i\uparrow}\hat{n}_{i\downarrow} + J_H \sum_\sigma \hat{n}_{1\sigma}\hat{n}_{2\bar{\sigma}}\end{aligned} \tag{3.12}$$

where in the last term $\bar{\sigma}$ denotes the opposite spin of σ. The last term gives rise to a step at $N = 2$ of height J_H in the Hxc potential similar to the inter-orbital interaction term but with step height J_H instead of $2U$ (fig. 3.4(d)).

When adding the density-density contribution of the Hund's rule coupling to the direct interaction part in Regime I ($U_{12} \leq U_1, U_2$), we can rewrite the interaction in terms of a CIM interaction, SSM terms, and the last term of the Hund density-density interaction (section 3.1.2) as

$$\begin{aligned}\mathcal{V}_{int} &= \frac{U_{12} - J_H}{2}\hat{N}(\hat{N}-1) + \sum_i (\delta U_i + J_H)\hat{n}_{i\uparrow}\hat{n}_{i\downarrow} \\ &+ J_H \sum_\sigma \hat{n}_{1\sigma}\hat{n}_{2\bar{\sigma}}\end{aligned} \tag{3.13}$$

where $\delta U_i = U_i - U_{12}$. Hence all terms can be modelled by the basic Hxc potentials shown in Fig. 3.5:

$$\begin{aligned}v_{\mathrm{Hxc,i}}[\boldsymbol{n}] = \; & v_{\mathrm{Hxc}}^{\mathrm{CIM}}(U_{12} - J_H)[N] + v_{\mathrm{Hxc}}^{\mathrm{SSM}}(\delta U_i + J_H)[\boldsymbol{n}] \\ & + v_{\mathrm{Hxc}}^{\mathrm{inter}}(J_H/2)[N].\end{aligned} \tag{3.14}$$

3.1.3 Generalization of Hxc potential to more than two orbitals

For specific choices of parameters we can generalize the Hxc potential for the DQD to an arbitrary number of orbitals in a straightforward manner. We concentrate on

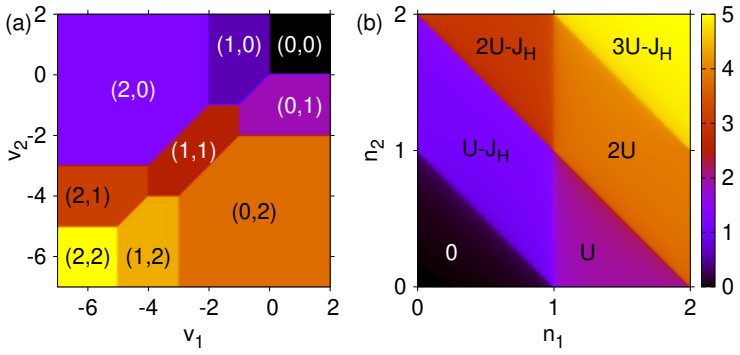

Figure 3.6: Effect of Hund's rule coupling on (a) Stability diagram and (b) Hxc potential of orbital 1 for CIM interaction plus Hund's rule coupling, $\mathcal{V}_{int} = \frac{U}{2}\hat{N}(\hat{N}-1) + \mathcal{V}_{\text{Hund}}$ for $U = 2J_H$. Here due to symmetry the Hxc potential for orbital 2 can simply be obtained by reflection along the $n_1 = n_2$ line. All energies in units of J_H.

the physically most relevant Regime I ($U_i, U_j > U_{ij}$). If we choose the inter-orbital interaction to be constant, $U_{ij} \equiv U'$, which thus has to be smaller than *all* of the intra-orbital interactions, $U' < U_i$, we can rewrite the interaction in a similar manner as in eq. (3.3) in terms of a CIM term $\sim U'$ for all the electrons $N = \sum_i n_i$ and SSM terms $\sim \delta U_i \equiv U_i - U'$ for the individual orbitals as

$$\mathcal{V}_{int} = \frac{1}{2}U'\hat{N}(\hat{N}-1) + \sum_i \delta U_i \, \hat{n}_{i\uparrow}\hat{n}_{i\downarrow} \tag{3.15}$$

where $\delta U_i = U_i - U'$. This suggests to decompose the xc functionals in complete analogy to the two-orbital case in Regime I as

$$v_{\text{Hxc,i}}[\boldsymbol{n}] = v_{\text{Hxc}}^{\text{CIM}}(U')[N] + v_{\text{Hxc}}^{\text{SSM}}(\delta U_i)[n_i]. \tag{3.16}$$

In the following section we will see that this decomposition of the Hxc potential leads to excellent results for multi-orbital QDs. For a more general choice of interaction parameters, the above decomposition is likely to become more complicated. This will be the focus of future work.

3.2 Results

In the following we will use the Hxc functional for the SSM (eq. (A.3)) as the basis for constructing approximations for the other three basic Hxc potentials into which the generic Hxc potential can be decomposed, namely the CIM, the

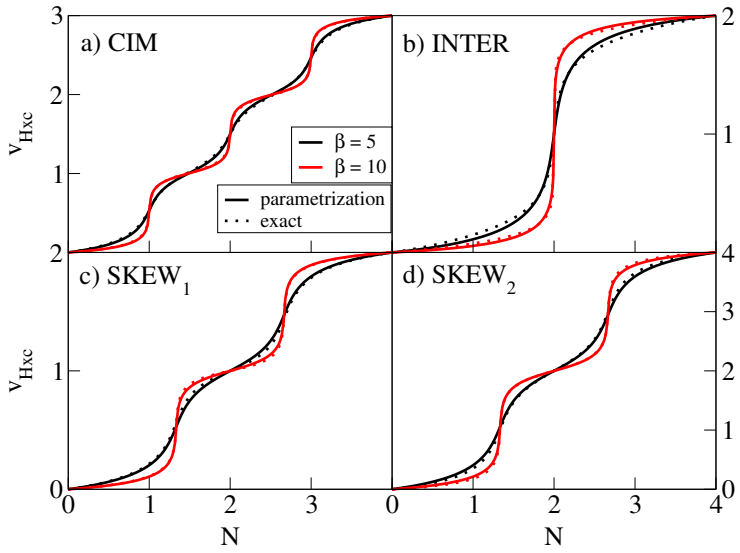

Figure 3.7: Comparison of parametrized and exact Hxc potentials as a function of $N = n_1 + n_2$ for three basic interactions: (a) CIM interaction ($U_1 = U_2 = U_{12} > 0$); (b) Inter-orbital interaction ($U_{12} > 0$ and $U_1 = U_2 = 0$); (c) Skew interaction ($U_2 = 2U_{12} > 0$ and $U_1 = 0$); All energies in units of the smallest non-zero interaction (U_{12}).

Inter-orbital, and the Skew potential (see fig. 3.5). For the CIM potential an excellent parametrization can be achieved by simply summing the (exact) SSM potential (A.3) over the charging states of the dot, and shifting and rescaling it such that the potential does not become negative or larger than $(2\mathcal{M} - 1)U$. This parametrization (eq. (A.23)) is presented in appendix A.

As can be seen in fig. 3.7(a), the agreement with the exact result is quite remarkable. In particular, it corrects the high temperature limit in which other DFT parametrization (eq. (A.22)) is not able to capture the properties of the functional, see fig. A.4.

For the inter-orbital potential we find a good parametrization describing the step at total $N = 2$ again in terms of the SSM potential, as

$$v_{\mathrm{Hxc}}^{inter}(U, \beta)[N] = v_{\mathrm{Hxc}}^{\mathrm{SSM}}(2U, \beta^*)[N/2] \tag{3.17}$$

where we have replaced the actual inverse temperature β by an effective reduced value, $\beta^* = 0.73\beta$ and the step height is increased by a factor of 2 compared to the SSM. The agreement with the exact potential is very good as can be seen in fig. 3.7(b).

Finally, for the Skew interaction, we parametrize the Hxc potential in a similar way as the Hxc potential for the CIM, by summing two SSM potentials, one for each of the steps, and shifting and rescaling so that the potential does not become negative or larger than the maximum value:

$$v^{\text{skew}}_{\text{Hxc,i}}(U)[\boldsymbol{n}] \;=\; \frac{i\,U}{v^{max}_{\text{skew}}} \sum_{J=0,1} \left\{ v^{\text{SSM}}_{\text{Hxc}}(\tfrac{U}{2}) \left[\tfrac{n_1}{2} + n_2 - J \right] - v^{\text{SSM}}_{\text{Hxc}}(\tfrac{U}{2})[-J] \right\} \quad (3.18)$$

where

$$v^{max}_{\text{skew}} = \sum_{J=0,1} \left\{ v^{\text{SSM}}_{\text{Hxc}}(\tfrac{U}{2})[3-J] - v^{\text{SSM}}_{\text{Hxc}}(\tfrac{U}{2})[-J] \right\}. \quad (3.19)$$

Also here the agreement with the exact potential is very good as can be seen in figs. 3.7(c+d).

We have thus found parametrizations of the four basic Hxc potentials. It should be noted, however, that at higher temperatures the exact CIM and Inter-orbital potentials (which in the zero temperature limit only depend on total N) acquire also a dependence on the difference $\delta N \equiv n_1 - n_2$ which has not been taken into account here.

In the following we study the evolution of the density $\boldsymbol{n}$ of multi-orbital QDs as a function of the applied gate v_g for different parameter sets with the purpose of check our constructed DFT parametrizations. The gate v_g exerts a total shift of the QD levels ϵ_i and hence the total gate for orbital i is given by

$$v_i = \epsilon_i + v_g. \quad (3.20)$$

Consequently, the differences in the gate potentials between different orbitals remain constant as the gate v_g changes, $\delta v_{ij} \equiv v_i - v_j = \epsilon_i - \epsilon_j$. In the following we will usually take the particle-hole symmetric (phs) point given by $\epsilon^*_i = -\frac{U_i}{2} - \sum_{j\neq i} U_{ij}$ as the reference system.

3.2.1 Results for the double quantum dot

We now study the DQD, and start by considering the degenerate case in Regime I, i.e. $U_1 = U_2 > U_{12}$ where $\epsilon_1 = \epsilon_2$. Fig. 3.8 compares the exact densities with the ones computed in DFT using the Hxc potential for Regime I, eq. (3.4). We see that

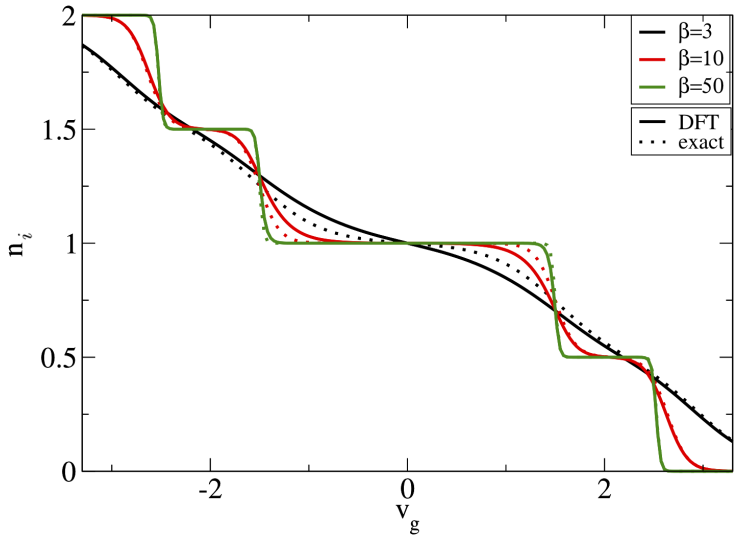

Figure 3.8: Density $\boldsymbol{n} = (n_1, n_2)$ as function of the gate voltage v_g for different temperatures when $U_1 = U_2 = 3U_{12} > 0$ (Regime I). The DFT result (solid line) becomes on top of the GCE result (dashed line) in the low temperature regime. All energies in units of the smallest interaction U_{12}.

the DFT results correctly describe all the features of the densities as a function of gate. At low temperatures, the width of the central step (around $v_g = 0$) is given by U_i while the other two step widths correspond to U_{12}. At higher temperatures our parametrization leads to moderate discrepancies in the slopes of the central step that disappear as the temperature approaches zero.

Next we consider the situation where the intra-orbital Coulomb repulsions are different, $U_1 > U_2 > U_{12}$. In fig. 3.9(a,b), the occupations n_i are presented as a function of the gate v_g for two different temperatures. At low temperatures (fig. 3.9(a)) and large negative gate voltage ($v_g < -2.5$) both orbitals of the DQD are completely filled ($n_i \sim 2$). As the gate is increased, first the orbital with the higher interaction (U_1) becomes half-filled around $v_g \sim -2.5$, and then around $v_g \sim -1.5$ also the orbital with the lower interaction (U_2) becomes half-filled. Upon further increase of the gate, the sequence is reversed, as first the orbital with the higher interaction and thus lower gate (v_2) is emptied around $v_g \sim 1.5$ and finally the orbital with lower interaction and thus higher gate (v_1) is emptied. At higher temperatures extra steps develop in the evolution of the density versus gate voltage, as can be seen in fig. 3.9(b). The appearance of new steps can be understood by

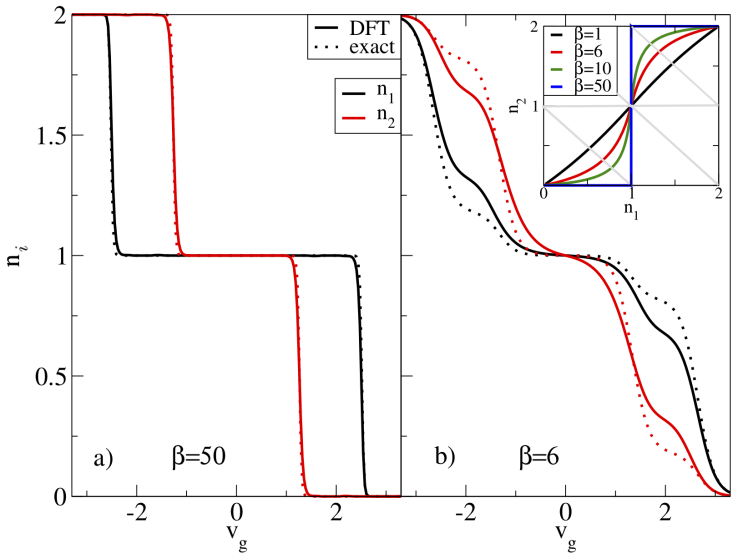

Figure 3.9: Density $\boldsymbol{n} = (n_1, n_2)$ as a function of the gate voltage v_g for $U_1 = 3U_{12}$, $U_2 = 2.5U_{12}$ (Regime I) for (a) low and (b) high temperatures. The inset of panel (b) shows the path in the $n_1 - n_2$ plane as the gate is varied for different temperatures. The grey lines show the steps of the CIM and SSM terms that appear in the Hxc potentials. All energies in units of the smallest interaction U_{12}.

the path taken in the $n_1 - n_2$ plane as the gate voltage changes, shown in the inset of fig. 3.9(b) for different temperatures. At low temperatures the path essentially follows three straight line segments, along the lower border, across the plane and finally along the upper border, thus avoiding extra steps of the CIM potential at $N = 1$ and $N = 3$. As the temperature increases the path becomes smoother, and passes through the $N = 1$ and $N = 3$ steps of the CIM potential, leading to the extra steps in the evolution of the densities at higher temperature. While for low temperatures the agreement of the DFT results with the exact ones is excellent, at higher temperatures deviations appear. Although DFT qualitatively captures the appearance of the extra steps in the evolution of the density versus gate voltage, their heights are not correctly reproduced in DFT. Presumably this discrepancy can be attributed to the development of a δN-dependence of the CIM potential at finite temperature, and will be addressed in future work.

Finally, we turn our attention to Regimes II and III, which are both characterized by the appearance of the peculiar "Skew" term in the Hxc potential. Fig. 3.10(a) directly compares the evolution of the density as a function of the gate in both

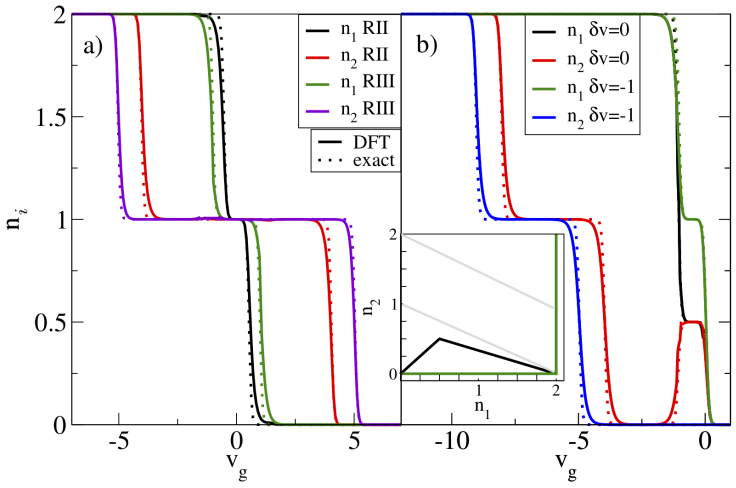

Figure 3.10: (a) Comparsion of the evolution of the density $\boldsymbol{n} = (n_1, n_2)$ with the gate voltage v_g in Regime II ($U_2 = 2U_{12} = 4U_1$) and Regime III ($U_2 = U_{12} = 4U_1$). (b) Comparison of density evolution for different two different values of the splitting δv in Regime II ($U_{12} = 2U_1$). The inset shows the different paths in the density plane. $\beta = 20/U_1$ everywhere. All energies in units of U_1.

regimes. As we can see the behaviour is actually quite similar for both regimes, and not so different from Regime I (fig. 3.9): As the gate increases, first the orbital with the higher interaction (here U_2) becomes half-filled, and then the orbital with the lower interaction (U_1). Then upon further increase of the gate, the order of emptying is reversed. Due to the higher inter-orbital interaction in Regime III, the width of the central plateau is increased for both orbitals. Again, at low temperature the agreement with the exact results is excellent, but at higher temperatures moderate quantitative deviations occur (not shown).

In order to investigate the influence of the Skew term in the Hxc potential on the evolution of the densities, we next concentrate on Regime II and explore different paths in the $n_1 - n_2$ plane. To this end we fix the energy splitting $\delta v = v_1 - v_2$ between the orbitals to different values while the total gate changes, i.e. $v_1 = \delta v + v_g$ and $v_2 = v_g$. Fig. 3.10(b) shows the evolution of the density for two different values of δv and correspondingly different paths in the $n_1 - n_2$ plane (shown in the inset). For $\delta v = 0$ we observe an interesting effect. As the gate increases, the occupation of orbital 2 decrease in two steps, first to half filled and then further to zero, while the first orbital remains fully occupied. Then around $v_g = -1$ the occupation of

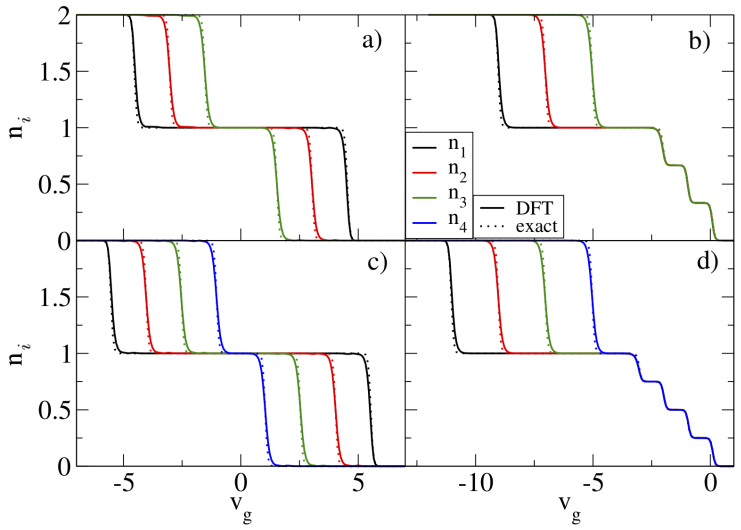

Figure 3.11: Local occupations for the triple (a, b) and quadruple (c, d) QD as function of the gate voltage. In the left panels the QD levels are taken at particle-hole ($v_i = \epsilon_i^* + v_g$) and in the right the impurities level is set to zero ($v_i = v_g$). $\beta = 20/U'$ and $U_1 = 5U'$, $U_2 = 4U'$, $U_3 = 3U'$, $U_4 = 2U'$. All energies in units of U'.

orbital 1 decreases abruptly to quarter filling, while now the occupation of orbital 2 increases again to quarter filling, $n_1 = n_2 = \sim 0.5$. This non-monotonic behavior of the occupation of orbital 2 is reminiscent of the so-called level occupation switching (LOS)[76, 77] and will be studied in detail in the following chapter. We find similar behaviour in Regime III (not shown).

3.2.2 Results for more than two orbitals

Finally, we apply the generalization of the Hxc potential (eq. (3.16)) for more than two orbitals to DFT calculations of multi-orbital QDs. Fig. 3.11 shows the evolution of the density n as a function of the applied gate voltage v_g for three (a,b) and four-level (c,d) QD with all intra-orbital Coulomb repulsions U_i different larger than the constant interdot repulsion $U' = U_{i,j}$ for all $i \neq j$ at low temperature. In panels (a) and (c) the gate v_g is applied w.r.t. the phs point, i.e. $\epsilon_i^* = -\frac{U_i}{2} - \sum_{j \neq i} U_{ij}$. In this case the path in the three- or four-dimensional density space avoids the steps in the CIM Hxc potential away from half-filling ($N = \mathcal{M}$) resulting in only three plateaus in the density evolution with the gate, in a similar way as in the DQD (fig. 3.9(a)). On the other hand, in panels (b) and (d) (where $\epsilon_i = 0$ and thus

$\delta v_{ij} = 0$) two (three) extra steps related to the inter-orbital Coulomb repulsions appear in the triple (quadruple) QD. The agreement between the DFT and the exact results is remarkable in all cases, showing that the generalization of eq. (3.16) of the Hxc potential to more than two orbitals is valid. Finding similar expressions for a more general choice of parameters will be the focus of future work.

4

Zero Temperature Conductance in Asymmetric Double Quantum Dot

Contents

4.1 The Level Occupation Switching effect in the double quantum dot 48

4.2 Modelling of the Hxc potentials with asymmetric couplings 51

In this chapter we use DFT to study charge transport properties of a capacitatively coupled double quantum dot in the Kondo regime. We construct a pair of Hxc functionals suitable for the description of the system in the situation of unequal coupling of the two dots to the reservoirs. We observe the Level Occupation Switching (LOS) effect which takes place when one of the dots is gradually disconnected from the electrodes but in contact with the other dot through the Coulomb interaction and benchmark against reference Numerical Renormalization Group (NRG) results.

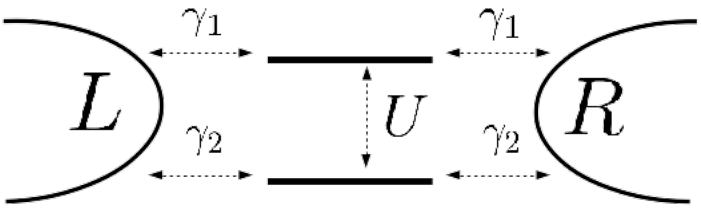

Figure 4.1: Schematic representation of the transport setup for the DQD.

4.1 The Level Occupation Switching effect in the double quantum dot

We consider a DQD consisting of two interacting impurities which can hold up to two electrons, each one coupled to two electrodes in the limit of low temperature. The total Hamiltonian of the system is given as the sum of the dot, the coupling between the leads and the dots, and the leads Hamiltonians

$$\hat{H} = \hat{H}_{DQD} + \hat{H}_{coupling} + \hat{H}_{leads}, \tag{4.1}$$

where

$$\hat{H}_{DQD} = \sum_{i\sigma} v_i \hat{n}_{i\sigma} + \sum_i U_i \hat{n}_{i\uparrow}\hat{n}_{i\downarrow} + U_{12}\hat{n}_1\hat{n}_2 \tag{4.2}$$

describes the capacitatively coupled DQD and $\hat{H}_{coupling}$ and $\hat{H}_{leads}$ are introduced in eq. (2.40) for $\mathcal{N} = 2$. In eq. (4.2) the index $i = 1, 2$ denotes the impurity level. We remind the reader that v_i and U_i are the on-site energy and the intra-Coulomb repulsion of the level i and U_{12} the intra-Coulomb repulsion between the two impurities.

In the following we work in the wide band limit (WBL), i.e., the system is coupled to featureless electronic leads described by frequency-independent couplings $\gamma_i = \Gamma_i(\omega)$. We also consider that each impurity is symmetrically coupled to both left and right leads. In fig. 4.1 the schematic representation of the DQD setup is shown with $U_{12} = U$.

In the KS system, the equilibrium density at temperature T in each dot can be expressed in terms of the non-interacting spectral function as (see eq. (2.30))

$$n_i = 2 \int \frac{d\omega}{2\pi} f(\omega) A_{s,i}(\omega) \tag{4.3}$$

where $f(x) = 1/(e^{x/T}+1)$ is the Fermi function of lead α and we set the equilibrium chemical potential $\mu = 0$ without loss of generality. Since we want to describe the situation in which the impurity is coupled to the reservoirs, we consider the non-interacting spectral function

$$A_{s,i}(\omega) = \frac{\gamma_i}{\frac{\gamma_i^2}{4} + (\omega - v_s)^2}. \tag{4.4}$$

In the limit of zero temperature, the Fermi function becomes a Heaviside step function $f(x) \to \theta(x)$ and eq. (4.3) reduces to

$$n_i = \frac{-2}{\pi} \arctan\left(2\frac{v_i + v_{\text{Hxc,i}}}{\gamma_i}\right) + 1 \tag{4.5}$$

where we have used the definition of the KS potential $v_{s,i} = v_i + v_{\text{Hxc,i}}$ of the dot i.

As stated in section 2.2.2, the correct description of the electrical conductance from a DFT approach requires the access to the correct (many-body) electrical current of the system, and therefore we require the inclusion of the xc corrections to the bias of the system (i-DFT framework). Nevertheless, it has been observed that in the limit of zero temperature, the KS zero-bias conductance already reproduces the correct behaviour of the interacting system due to the Friedel sum rule [45, 78, 79]. In this regime the current through the dots is described by the LB formula eq. (2.34) and then the zero bias electrical conductance in each of the dots is defined through eq. (2.35). The total KS linear conductance in the DQD system can be expressed as the sum of its individual contributions

$$G_s = \left.\frac{\partial I_s}{\partial V}\right|_{V=0} = \sum_{i=1}^{2} G_{s,i} = \sum_{i=1}^{2} \frac{\frac{\gamma_i^2}{4}}{v_{s,i}^2 + \frac{\gamma_i^2}{4}}. \tag{4.6}$$

Eq. (4.6) must be in agreement with the Friedel sum rule [80–82] which states that at zero temperature the zero-bias conductance of single-channel problems is

fully determined by the equilibrium density at the impurity. Since exact DFT by construction gives the exact equilibrium density, it therefore also must yield the exact zero-bias conductance, including the conductance plateau due to the Kondo effect. The Friedel sum rule expression for the electrical conductance reads

$$G = \sum_i \sin\left(\frac{\pi n_i}{2}\right)^2. \tag{4.7}$$

Eqs.(4.6) and (4.7) provide two equivalent expressions in the zero temperature regime for the determination of the electrical conductance.

There is an interesting physical effect in a strongly correlated DQD when the coupling to one of the dots is gradually reduced: this problem is well understood in the literature and has been studied in detail using different many-body approaches [77, 83]. When both dots are equally coupled to the leads $\gamma_1 = \gamma_2$ and $v = v_1 = v_2$, the physical system's symmetries are mathematically described by the SU(4) Lie group. In the Kondo regime, this setup leads to a plateau of height $2G_0$ in the conductance due to the contribution of the two degenerate levels. The effect of reducing the coupling of one of the dots to the leads (while keeping the coupling of the other dot fixed) induces a change in the local occupation of the dots and abrupt population inversions between them start to emerge. This effect is the so called level occupation switching (LOS). The transition between the totally symmetric case $\eta = \frac{\gamma_2}{\gamma_1} = 1$ to the completely asymmetric setup $\eta = \frac{\gamma_2}{\gamma_1} = 0$ (where the symmetries of the system are governed by the SU(2) Lie group) will be described using a DFT approach by realizing the correct Hxc potential's properties.

For equal couplings, $\gamma_1 = \gamma_2$, an Hxc functional with steps at integer occupation of the DQD has already been shown [79] to lead to a correct description of the density and the resulting KS conductance correctly describes the SU(4) Kondo regime. Therefore what remains to be done is to construct (local) Hxc functionals which also can describe the situation of the DQD with different couplings to the leads.

4.2 Modelling of the Hxc potentials with asymmetric couplings

We aim to construct approximations for the Hxc functionals which capture the effect produced through the variation of the coupling between each of the impurities with the leads in the fourfold-degenerate case $U_i = U_{12} = U$. For the sake of simplicity we also consider $v = v_1 = v_2$.

In the previous chapter we discussed that for an isolated DQD in a thermal bath, the Hxc functional can be described as the sum of steps or "basic building blocks", each of which corresponds to an xc correction to the simplest model with different density or parametric dependence. For the coupled case we follow the same argument based on the observation that the temperature and the coupling lead to similar smeared out of step features. The accuracy in the description of the densities of the DQD in the DFT approach then relies on the parametrization and on the way of adding the steps when constructing the Hxc potential for the CIM system, i.e., the Hxc functionals for the two dots are given by a combination of different steps in the $n_1 - n_2$ plane, as detailed in section 3.1.1.

We first propose the following simple structure for the Hxc potentials of the DQD

$$v_{\mathrm{Hxc,i}}^{\mathrm{CIM}}[N](\gamma_i) = v_{\mathrm{Hxc}}^{\mathrm{SIAM}}[N](\gamma_i) + v_{\mathrm{Hxc}}^{\mathrm{SIAM}}[N-1](\gamma_i) + v_{\mathrm{Hxc}}^{\mathrm{SIAM}}[N-2](\gamma_i). \tag{4.8}$$

consisting in the addition of three steps, each one centered at different total integer occupation N. In eq. (4.8) we have made explicit that the Hxc correction for dot i does only depend on the coupling γ_i.

For the $v_{\mathrm{Hxc}}^{\mathrm{SIAM}}$ potential we consider the accurate parametrization at $T = 0$ obtained using Bethe ansatz techniques in ref. [84], see eq. (A.9).

The combination of eq. (4.5) and eq. (4.8) constitutes the self-consistent KS equations that we solve using a numerical root solver method, e.g., the bisection algorithm. It is worth to notice that as the population inversions become more abrupt in the densities, the numerical evaluation of the problem becomes unstable.

In fig. 4.2 (left) we show the total KS conductance (in units of the quantum of conductance G_0) for strong correlations $U/\gamma_1 = 10$ and different values of the

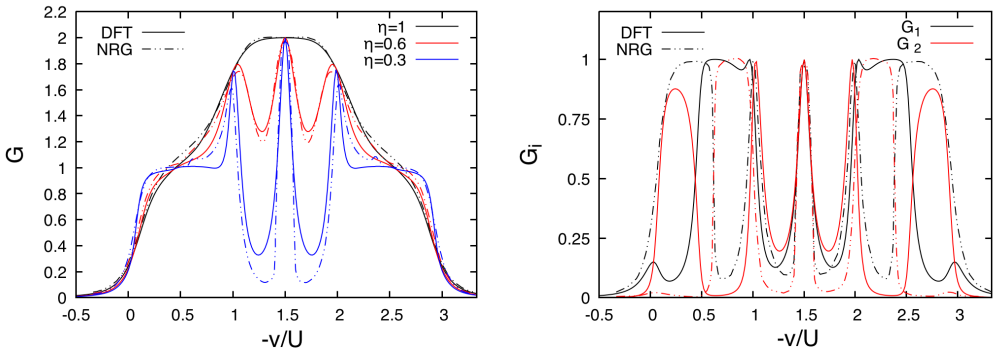

Figure 4.2: Left: Total electrical conductance for different coupling ratios $\eta = \frac{\gamma_2}{\gamma_1}$. Right: Local contributions to the electrical conductance when $\eta = 0.3$. In both plots the DFT result is obtained making use of the Hxc potentials of eq. (4.8), $U/\gamma_1 = 10$ and the conductances are measured in units of que quantum of conductance G_0.

coupling ratio $\eta = \frac{\gamma_2}{\gamma_1}$. As the coupling of the second dot is decreased, a three peak structure in the total conductance centered at the particle hole symmetric point starts to emerge due to the LOS effect that takes place in the densities. Although the results are in general in agreement with the NRG analysis from ref. [77], the local contributions to the KS conductance (fig. 4.2 (right)) fail to capture the correct physics. In fact, the KS conductance $G_{i,s} = G_1$ qualitatively follows the G_2 of NRG (and $G_{2,s}$ follows G_1 of NRG), finding good agreement only around the particle-hole symmetric point. This observation suggests us to swap the dependence on the couplings to the leads, i.e., we define the Hxc potentials for the DQD with asymmetric couplings to the leads as

$$v_{\mathrm{Hxc,i}}[N] = v^{\mathrm{CIM}}_{\mathrm{Hxc,i}}[N](\gamma_j), \quad (i \neq j), \tag{4.9}$$

i.e., we propose a functional parametrization in which the coupling dependence is only due to the other dot. This simple modification leads to very different results of the densities and therefore of the electrical conductances. In fig. 4.3 the total electrical conductance from eq. (4.6) with the functionals provided by eq. (4.9) with the CIM contribution of eq. (4.8) shows an excellent agreement with the NRG results for different values of the coupling ratio η and strong correlations $U/\gamma_1 = 10$. Moreover, compared to NRG, the accuracy of our DFT results at low coupling ratio η is improved with respect to the previous parametric coupling dependence

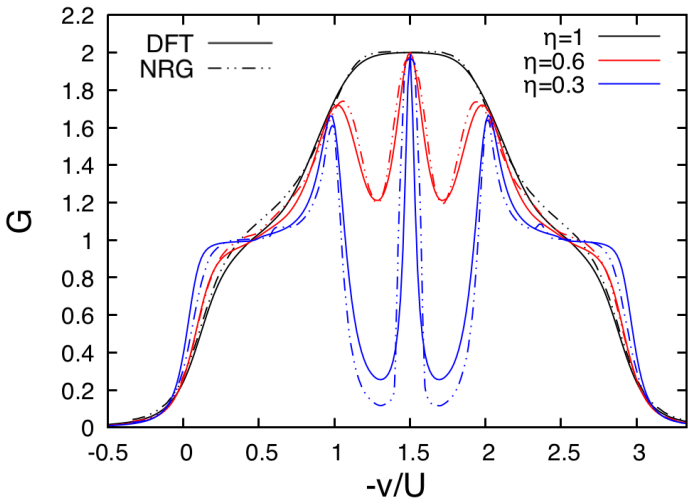

Figure 4.3: Total electrical conductance comparison between DFT with the Hxc potentials of eq. (4.9)(solid line) and NRG (dashed line) for different values of $\eta = \frac{\gamma_2}{\gamma_1}$ and $U/\gamma_1 = 10$.

(eq. (4.8)). The main improvement of the functionals of eq. (4.9) is observed in fig. 4.4 (left) where the DFT results capture the sudden transitions between 0 and 1 governed by the LOS effect in the densities (fig. 4.4 (right)). Nevertheless, one observe that the DFT transitions occur at multiple values of $v = -\frac{U}{2}$ while the NRG ones are slightly shifted with respect to these values. The reason behind this deviation is in the structure of the considered functionals: The proposed CIM functional is by construction pinned at integer values of the total occupation and therefore $v_{\mathrm{Hxc},1}[N] = v_{Hxc,2}[N]$ for $N \in \mathbb{Z}$. The LOS effect takes place exactly at the gate in which the populations are inverted, and therefore $n_1 = n_2$. From the KS equations of the density eq. (4.5) we observe that the gate at which this conditions are fulfilled corresponds to $v = -v_{\mathrm{Hxc}}$.

For the completely asymmetric situation $\eta \to 0$, the functional structure of eq. (4.9) do not capture the observations from NRG [77], requiring the addition of a step centered at $n_i = 1$ with the corresponding coupling to the leads γ_i and the subtraction of a step equally centered but with the coupling corresponding to the other impurity γ_j

$$v_{\mathrm{Hxc,i}}^{\eta\to 0}[N] = v_{\mathrm{Hxc,i}}^{\mathrm{CIM}}[N](\gamma_j) + v_{\mathrm{Hxc}}^{\mathrm{SIAM}}[n_i](\gamma_i) - v_{\mathrm{Hxc}}^{\mathrm{SIAM}}[n_i](\gamma_j) \tag{4.10}$$

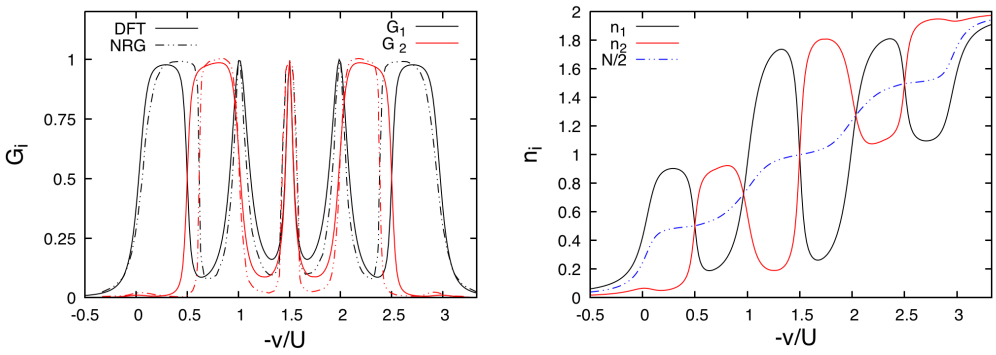

Figure 4.4: Left: Local contributions to the electrical conductance and Right: Local occupations as function of the gate voltage. In both plots the DFT result is obtained making use of the Hxc potentials of eq. (4.9), and $U/\gamma_1 = 10$.

In fig. 4.5 we present the results for the DQD in the asymmetric limit $\eta = 0$ and strong correlations $U/\gamma_1 = 10$ considering two different Hxc functional parametrizations: DFT 1 represents the results obtained through eqs. (4.9) and (4.10) while DFT2 the corresponding ones using eqs. (4.10) and (A.23) with the $v_{\rm Hxc}^{\rm SIAM}$ without any interpolation (see text below eq. (A.9)). In the left panel the NRG densities show six switching events in the occupancies around $v = -\frac{U}{2}, -U, 2U, -\frac{5U}{2}$ and two around $v = -\frac{3U}{2}$. The DFT 1 results for the density (and therefore for the electrical conductance) predict the LOS exactly at this multiple values of $-\frac{U}{2}$ due to the aforementioned pinning of the functional at $N \in \mathbb{Z}$. In this asymmetric limit $\eta \to 0$ when $v = v_1 = v_2$ the local occupations vary from almost empty to full occupied, where the Hxc functional is not accurate. In contrast, the DFT 2 results obtained by rescaling the addition of steps correctly capture almost all the features of the NRG results. The main discrepancy in both DFT approaches corresponds to the width of the central plateau in the densities and the conductance.

While the structure of eqs. (4.9) and (4.10) is based on the addition of step features centered at integer values of the total occupation N, a deeper understanding on the parametric dependence of $v_{\rm Hxc,i}$ on the effective coupling in each step remains an open question and the focus of future works.

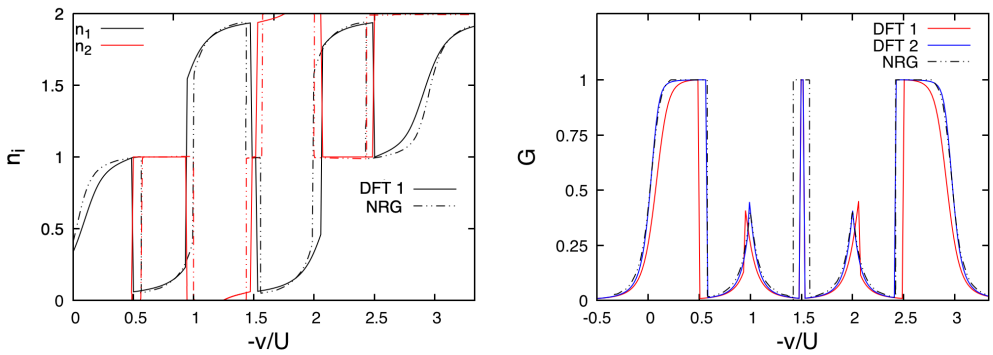

Figure 4.5: Local occupations (left) and electrical conductance (right) comparison between DFT (solid line) and NRG (dashed line) in the asymmetric limit $\eta = \frac{\gamma_2}{g_1} \to 0$ with $U/\gamma_1 = 10$. The DFT1 results is obtained through eqs. (4.9) and (4.10) while DFT2 with eqs. (4.10) and (A.23) with the $v_{\text{Hxc}}^{\text{SIAM}}$ without any interpolation.

Part II

Non-Equilibrium Density Functional Theory

This chapter is based on the article [85].

5

Steady-state Density Functional Theory Formalism for Electronic Transport with Finite Thermal Gradients

Contents

5.1 i-DFT for finite temperature gradients 60
5.1.1 Reverse engineering of the SIAM xc potentials for finite thermal gradient 61
5.2 Transport coefficients 66
5.2.1 Electrical conductance 66
5.2.2 Seebeck Coefficient 67
5.2.3 Thermal conductance 73

In this chapter we generalize the i-DFT framework to situations with finite temperature gradients [85]. The extension of the formalism through the restatement of the theorem for different temperatures in the leads opens the path to construct xc functionals with explicit dependence on the thermal gradient. Taking advantage of this idea, we derive a formally exact expression for the Seebeck coefficient valid for any molecular system in terms of purely i-DFT accessible quantities, in an analogous way to the electrical conductance [41]. We apply the general equations of the transport coefficients to the SIAM in both the CB and the Kondo regime.

5.1 i-DFT for finite temperature gradients

We consider the typical transport setup where a central region, e.g., a single molecule or a quantum dot, is coupled to a left (L) and a right (R) electrode. The system is driven out of equilibrium by applying a DC bias V across the junction and we are interested in the resulting steady-state current I. In the recently suggested i-DFT framework for steady-state transport (section 2.2.2), both left and right leads are kept at the same temperature T which enters the formalism as an external parameter only. Here we propose an extension of i-DFT to include a temperature difference between the leads. This thermal gradient creates an electronic current which can be compensated by a bias in an open circuit setup and thus allows to study the Seebeck effect. For simplicity, we symmetrically apply both a bias V as well as a temperature difference ΔT between the two leads, i.e., we have $V_\alpha = \pm V/2$ and $T_\alpha = T \pm \Delta T/2$ where $\alpha = L, R$[1]. Of course, now both T_L and T_R (or, equivalently, T and ΔT) enter as parameters into the formalism. If we make the (physically reasonable) assumption that the density in the central region and the current are continuously differentiable at $\Delta T = 0$, the original i-DFT proof [41] of the one-to-one correspondence between "densities" and "potentials" can directly be applied to our situation and we can formulate the i-DFT theorem for leads at different temperatures.

Theorem: For any pair of finite temperatures T_α in the leads, there exists a one-to-one correspondence between the pair of "densities" (n, I) and the pair of "potentials" (v, V) in a finite (and gate dependent) region around zero voltage V and zero thermal gradient ΔT.

The self-consistent coupled KS equations for the density and the current have the same structure as the original i-DFT eqs. (2.38a) and (2.38b) with the exception that the temperature difference ΔT between the two leads enters explicitly both in the Fermi functions f_α and in the functionals for v_{Hxc} and V_{xc}.

[1] Needless to say, we assume $T > \Delta T/2$ such that $T_L, T_R > 0$.

5.1.1 Reverse engineering of the SIAM xc potentials for finite thermal gradient

In this section we consider the SIAM (see section 2.3) as the first model for the development of approximate i-DFT functionals. In previous works [41, 45], some accurate parametrizations for the xc functionals in the wide band limit were designed in the case of equal lead temperatures, $T_L = T_R$. Our aim now resides in the construction of functionals in the more general case $T_L \neq T_R$.

Coulomb blockade regime - Following ideas used in earlier work [41], we first aim to construct approximations for the xc functionals in the Coulomb blockade regime. The main idea behind the RE process consists of inverting the equations of the basic variables (n, I) in terms of the basic potentials (v, V) both for the interacting system and for the non-interacting case. The difference between the non-interacting and the interacting potentials (as function of the basic variables) leads to the desired xc functionals.

The density on and the current through the dot in terms of the many-body spectral function $A(\omega)$ is [86]

$$n = \int \frac{d\omega}{2\pi} \left[\frac{2\gamma_L}{\gamma} f_L(\omega - V_L) + \frac{2\gamma_R}{\gamma} f_R(\omega - V_R) \right] A(\omega), \tag{5.1a}$$

$$I = \frac{2\gamma_L\gamma_R}{\gamma} \int \frac{d\omega}{2\pi} \left[f_L(\omega - V_L) - f_R(\omega - V_R) \right] A(w), \tag{5.1b}$$

where $\gamma = \gamma_L + \gamma_R$ is the total broadening.

In order to invert eqs. (5.1) we need a model for the many-body spectral function $A(w)$. As a starting point we use the exact spectral function of the SSM which is given by

$$A_0^{\mathrm{mod}}(\omega) = \left(1 - \frac{n}{2}\right) \delta(\omega - v) + \frac{n}{2} \delta(\omega - v - U) \, . \tag{5.2}$$

Using $A_0^{\mathrm{mod}}(\omega)$ as model spectral function for the *contacted* dot brings about an approximation since we are not considering the effect of the couplings. Nevertheless, it leads to exactly the same expressions for density and current as one would obtain by working out the rate equations which are valid in the CB regime [87]. Inserting eq. (5.2) into eqs. (5.1), the reverse-engineering for the Hxc gate and xc

bias potentials can be done analytically. This follows by forming from eqs. (5.1) the linear combinations $n + I/\gamma_L$ and $n - I/\gamma_R$ and realizing that the inversion of the resulting equations for the potentials $v \pm V/2$ (and $v_s \pm V_s/2$) can be done exactly as in refs. [47, 48]. The full inversion of the functionals is done in appendix A.2 obtaining the following Hxc gate and xc bias potentials

$$v_{\mathrm{Hxc}} = \frac{1}{2}\left[g(n, -I/\gamma_R, T_R) + g(n, I/\gamma_L, T_L)\right] \tag{5.3a}$$

$$V_{\mathrm{xc}} = g(n, -I/\gamma_R, T_R) - g(n, I/\gamma_L, T_L)\ , \tag{5.3b}$$

where we have defined

$$g(n, x, T) = U + T \log\left(\frac{p + \sqrt{p^2 - zye^{-U/T}}}{y}\right) \tag{5.4}$$

with $z = y - 2$, $y = 4x + n$ and $p = n - 1 + 2x\left(1 + e^{-U/T}\right)$. As mentioned above, eqs. (5.3) are equivalent to reverse-engineering the rate equations and therefore should be valid at high temperatures $T \gg \gamma$, i.e., in the parameter regime where the effect of temperature is much more important than the coupling to the leads.

For the construction of xc potentials which give reasonable approximations also in the regime of $T \sim \gamma$ we use the observation [15] that both temperature T and spectral broadening γ lead to similar smearing out of step features of the xc potentials which are present in the low-temperature and/or strongly correlated limit. Therefore we suggest a parametrization using the same analytic form as in eqs. (5.3) but replacing the left and right temperatures $T_{L/R}$ by effective temperatures $T^*_{L/R}$

$$T^*_\alpha(T_\alpha, \gamma) = \frac{T_\alpha^2 + (\eta\gamma)^2 + \eta\gamma T_\alpha}{T_\alpha + \eta\gamma}\ . \tag{5.5}$$

This parametrization is chosen in such a way that $T^*_\alpha(T_\alpha, \gamma \to 0) = T_\alpha$ and η is a fit parameter for which we take the value $\eta = 0.45$ in the CB regime.

In order to benchmark our analytical parametrizations, we consider the reference results from the MBM associated with the many-body spectral function

$$A^{\mathrm{mod}}_\gamma(\omega) = \left(1 - \frac{n}{2}\right) l_\gamma(\omega - v) + \frac{n}{2} l_\gamma(\omega - v - U). \tag{5.6}$$

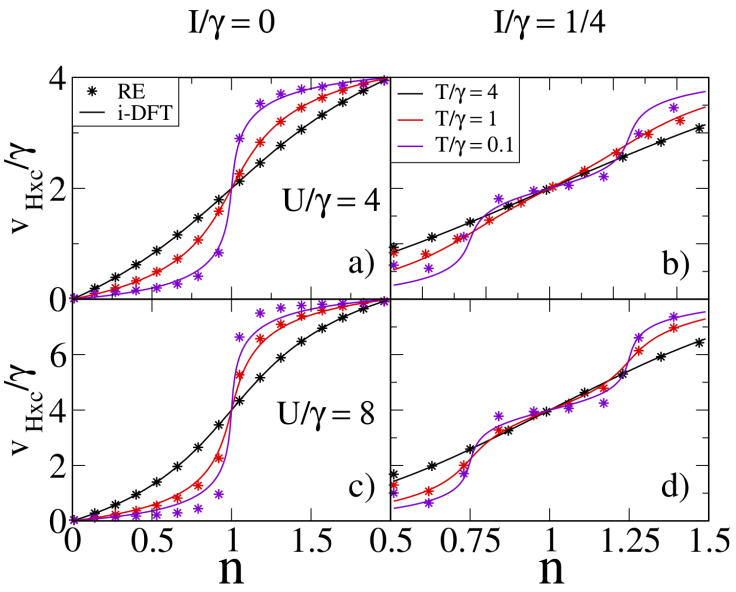

Figure 5.1: Hxc potential v_{Hxc} of the symmetrically coupled SIAM ($\gamma_L = \gamma_R = \gamma/2$) in the Coulomb blockade regime for different temperatures calculated by reverse-engineering (RE) compared to the parametrization (i-DFT) of eq. (5.3) including the effective temperature of eq. (5.5). Panels a) and b) are for $U/\gamma = 4$, panels c) and d) for $U/\gamma = 8$, while panels a) and c) are for zero current $I = 0$ and panels b) and d) for $I/\gamma = 1/4$.

Eq. (5.6) can be though as a generalization of eq. (5.2) where the effect of the broadening γ due to the coupling to the leads is taken into account. Let us note that the RE process has been carried out using eq. (5.2) instead of eq. (5.6) since the latter inversion of the potentials can not be done in an analytical way.

The quality of our parametrization can be appreciated in fig. 5.1 where we compare the model v_{Hxc} (eq. (5.3a)) including the effective temperature with the corresponding results of the numerical RE from the MBM spectral function (eq. (5.6)) for $U/\gamma = 4$ (panels a) and b)) and $U/\gamma = 8$ (panels c) and d)). We see that, at equilibrium ($I = 0$, panels a) and c)), our parametrization reproduces the RE Hxc potential very accurately for all the considered temperatures. Also at finite current ($I/\gamma = 1/4$, panels b) and d)), our approach gives a reasonable parametrization of the reverse-engineered Hxc potential, although there are some differences at the borders of the domain for the lowest temperature.

As another check on the quality of our parametrization, in fig. 5.2 we show the density and the electronic current induced by a temperature difference ΔT between

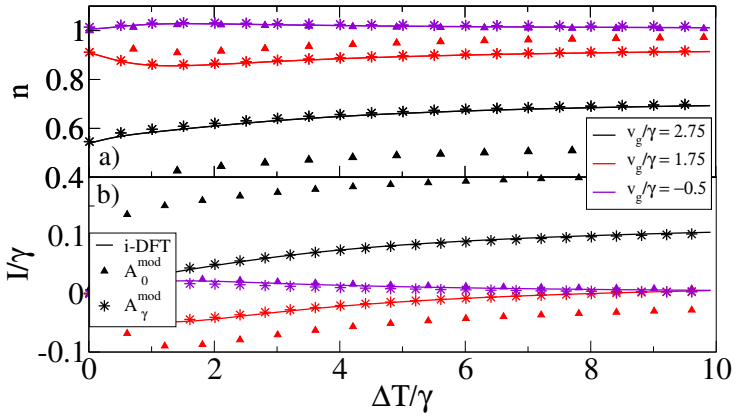

Figure 5.2: Densities (panel a)) and currents (panel b)) as function of the temperature difference $\Delta T = T_L - T_R$ for $U/\gamma = 5$, $T_R = 0.1$ and $V = 0$ for different gate voltages $v_g = v + \frac{U}{2}$. The i-DFT results using the xc potentials of eq. (5.3) and the effective temperature of eq. (5.5) are compared with those obtained directly from eq. (5.1) when using either the model spectral function A_0^{mod} of eq. (5.2) or A_γ^{mod} of eq. (5.6).

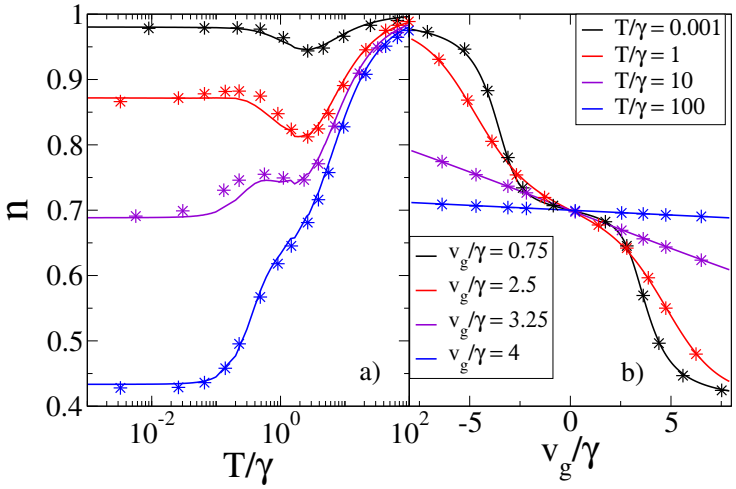

Figure 5.3: Panel a) Densities as function of temperature for different gate voltages. Panel b) Densities as function of gate voltage for different temperatures. In both panels i-DFT results are compared with the NRG results of ref. [88] for $U/\gamma = 8$.

the leads (at zero bias) as function of ΔT for different gate voltages $v_g = v + U/2$. The i-DFT results using the effective temperature T_α^* are compared to those obtained by the direct evaluation of eqs. (5.1) with the model spectral functions of eq. (5.2) and eq. (5.6), respectively. Note that the A_0^{mod} result exactly corresponds to the result that we would obtain with the functionals of eqs. (5.3) without including the effective temperature. Therefore, the excellent agreement with A_γ^{mod} is due to the inclusion of the effective temperature eq. (5.5).

Kondo regime - So far we have constructed functionals in the temperature regime of CB $T \gtrsim T_K$ where the Kondo temperature is defined as [88]

$$T_K = \gamma \sqrt{\frac{U}{4\gamma}} e^{\pi\gamma \frac{(v_g\gamma)^2 - (U/\gamma)^2}{U}}. \tag{5.7}$$

In order to extend the range of applicability of our approximation to temperatures below T_K, we follow the ideas outlined in ref. [45]. There the central observation was that at zero temperature the correct behaviour of the zero-bias conductance is already contained in the KS conductance

$$G = \frac{G_s}{1 - G_s \left.\frac{\partial V_{\rm xc}}{\partial I}\right|_{V=0}}, \tag{5.8}$$

due to the Friedel sum rule [70, 78, 84]. Therefore, at zero temperature the derivative $\partial V_{\rm xc}/\partial I$ has to vanish at $I = 0$. Following ref. [45], we modify our functional as

$$v_{\rm Hxc} = [1 - k(n, I, T)]\, v_{\rm Hxc} + k(n, I, T) v^{(0)}_{\rm Hxc}(n), \tag{5.9a}$$

$$V_{\rm xc} = [1 - k(n, I, T)]\, V_{\rm xc}(n, I, T), \tag{5.9b}$$

where $v^{(0)}_{\rm Hxc}$ is the zero-temperature, equilibrium Hxc potential of eq. (A.9) which accurately parametrizes density matrix renormalization group results [84].

We further introduce the prefactor $k(n, I, T)$ with the properties $k(n, I = 0, T = 0) = 1$ and $\partial k(n, I, T)/\partial I|_{I=0,T=0} = 0$, see eq. (A.8). The first property ensures that at zero current and zero temperature $v_{\rm Hxc}$ reduces to $v^{(0)}_{\rm Hxc}$, the second one leads to a vanishing correction to the KS zero-bias conductance at zero temperature. To be specific, we choose $k(n, I, T) = a(n, I)z(T)$, where $a(n, I)$ corresponds to the product of eqs. (A.8a) and (A.8b). This prefactor, although combined with a different form for the CB functionals $v_{\rm Hxc}$ and $V_{\rm xc}$, ensures a good description of the finite bias conductance for relatively low temperatures. We also found it convenient to introduce another prefactor $z(T) = (1 + (2.5T/\gamma)^3)^{-1}$ to ensure a smooth transition to the CB form of the functional at high temperatures. Finally, we redefine $\eta = 0.1U/\gamma + 0.36$ entering in the effective temperature T^* of eq. (5.5) in

order to correct the effect of the interactions at low temperatures. This is somewhat similar to ref. [45] where the smoothening of the step features in the CB part of the functional had to be modified in the Kondo regime $T \lesssim T_K$.

As a first test of this functional, we calculate self-consistent densities at equilibrium. Since no thermal gradient nor bias is applied, we only require the parametrizations of eq. (5.9a). In fig. 5.3 a) we plot the densities obtained for different gate voltages as function of the temperature of the leads $T = T_L = T_R$ for the strongly correlated case with $U/\gamma = 8$ and compare with numerical renormalization group (NRG) results of ref. [88]. Instead, in fig. 5.3 b) we show equilibrium densities as function of gate voltage for different temperatures. The agreement of our i-DFT densities with the NRG ones is excellent.

5.2 Transport coefficients

5.2.1 Electrical conductance

As explained in section 2.2.2, the i-DFT formalism provides the correct framework to calculate the many-body linear electrical conductance of any molecular system by correcting the non-interacting result (which corresponds to the LB result) according to eq. (5.8).

In the SIAM, the non-interacting contribution G_s can be calculated analytically as described in appendix B

$$G_s = \frac{-\gamma}{4\pi}\int f'(\omega)\frac{d\omega}{(\omega - v)^2 + \frac{\gamma^2}{4}} = \frac{\gamma}{4\pi^2 T}\mathrm{Im}\Big[i\psi^{(1)}(\frac{1}{2} + \frac{\gamma}{4\pi T} + i\frac{v_s}{2\pi T})\Big] \qquad (5.10)$$

where $\psi^{(1)}$ is the trigamma function [89].

In fig. 5.4, we show differential conductances for the SIAM at the particle-hole symmetric point obtained with the parametrizations of eq. (5.9) and compare them with those obtained using the functionals of ref. [45] (shown in eq. (A.6)) as well as with functional renormalization group (fRG) results of ref. [90]. The i-DFT results with our present functional agree reasonably well with the reference fRG results although some details like the overall shape of the side peaks seem to be

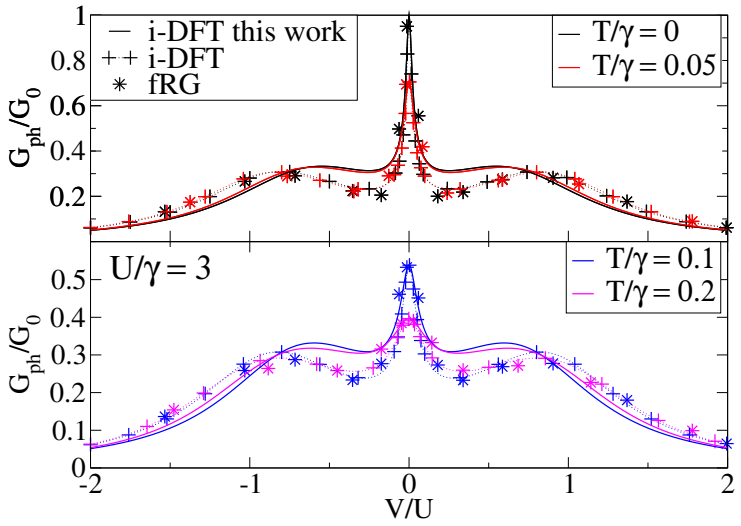

Figure 5.4: Differential conductance G_{ph} at the particle hole symmetric point $v = -U/2$ for the SIAM for $U/\gamma = 3$. The i-DFT results obtained with the functional of eqs. (5.9) are compared to those from ref. [45] and the fRG results of ref. [90]. $G_0 = 1/\pi$ is the quantum of conductance.

better captured by the functional of ref. [45]. Finally, the differential conductance at zero bias has been calculated and compared with both fRG of ref. [90] and NRG of ref. [91] for different interaction strengths obtaining very good agreements, as can be appreciated in fig. 5.5. In particular, the strongly correlated regime shown in fig. 5.5d) is completely captured within i-DFT from the Kondo regime at low temperatures (where the differential conductance shows a plateau centered at the particle-hole symmetric point) to the CB regime at higher temperatures (where te differential conductance's structure consist of a two peak structure at $v = -U, 0$). Here we remark one of the main advantages with respect to LB+DFT: While the Kondo regime physics of the differential conductance is correctly captured within LB+DFT, in the CB regime LB+DFT completely fails to describe the two peak structure centered at the particle-hole symmetric point that corresponds to the blue line of fig. 5.5d) showing a plateau instead (see ref.[15]), even when the exact functional is used.

5.2.2 Seebeck Coefficient

The Seebeck coefficient is defined as that bias which has to be applied to compensate a small temperature difference between the leads such that no current flows.

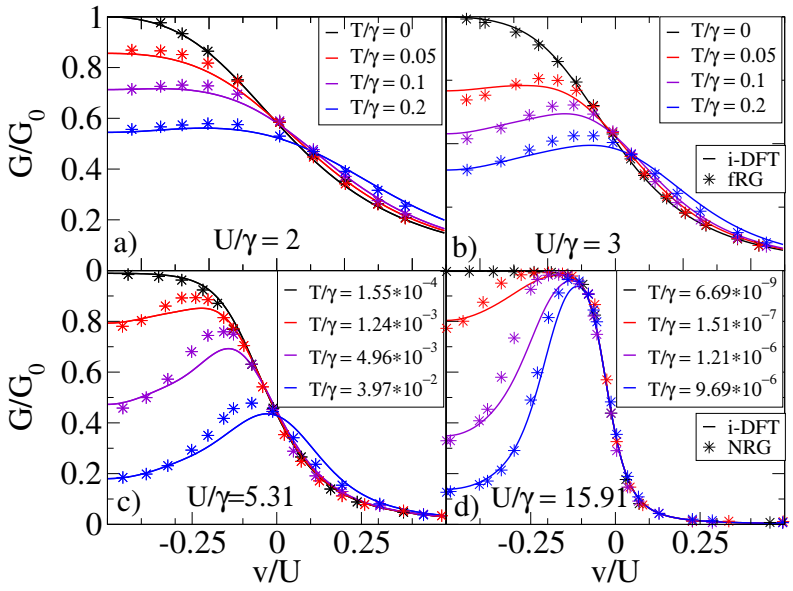

Figure 5.5: Zero-bias differential conductance of i-DFT obtained with the functional of eqs. (5.9) as function of the gate level v for different values of U/γ. In panels a) and b) the results are compared to fRG ones from ref. [90], in panels c) and d) NRG results from ref. [91] are used for comparison. $G_0 = 1/\pi$ is the quantum of conductance.

Formally it can be written as

$$S = \left.\frac{dV}{d\Delta T}\right|_{I=0}. \tag{5.11}$$

In general, we can write the infinitesimal variation of the electrical current as the sum of two contributions, i.e

$$dI = \left.\frac{dI}{dV}\right|_{\substack{V=0\\ \Delta T=0}} dV + \left.\frac{dI}{d\Delta T}\right|_{\substack{V=0\\ \Delta T=0}} \Delta T. \tag{5.12}$$

Therefore, we can rewrite the Seebeck coefficient as

$$S = -\frac{\left.\frac{dI}{d\Delta T}\right|_{\substack{V=0\\ \Delta T=0}}}{\left.\frac{dI}{dV}\right|_{\substack{V=0\\ \Delta T=0}}}. \tag{5.13}$$

In the linear response regime, a general expression for the Seebeck coefficient within i-DFT can be derived. We start by defining the quantities

$$L_s = -\frac{\gamma}{2T}\int d\omega f'(\omega) w A_s(\omega), \tag{5.14a}$$

$$G_s = -\frac{\gamma}{2}\int d\omega f'(\omega)\frac{dV_{\rm xc}}{d\Delta T} A_s(\omega). \tag{5.14b}$$

The numerator of eq. (5.13) is therefore

$$\frac{dI}{d\Delta T} = -\frac{\gamma}{2}\int d\omega f'(\omega)\left(\frac{dV_{\rm xc}}{d\Delta T}+\frac{w}{T}\right)A_s(\omega) = G_s\frac{dV_{\rm xc}}{d\Delta T}+L_s. \tag{5.15}$$

Expanding out the total derivative of the xc contribution

$$\frac{dV_{\rm xc}}{d\Delta T} = \frac{\partial V_{\rm xc}}{\partial \Delta T}+\frac{dV_{\rm xc}}{dI}\frac{dI}{d\Delta T}+\int d^3r\frac{\delta V_{\rm xc}}{\delta n(\mathbf{r})}\frac{dn(\mathbf{r})}{d\Delta T} \tag{5.16}$$

and taking into account that for the linear response regime ($V=0$ and $\Delta T=0$) the last term vanishes because $V_{\rm xc}[n, I=0]=0$, one finds

$$\frac{dI}{d\Delta T} = \frac{G_s\frac{\partial V_{\rm xc}}{\partial \Delta T}+L_s}{1-\frac{dV_{\rm xc}}{dI}}. \tag{5.17}$$

Combining eqs. (5.8) and (5.17) we then arrive at the following simple expression for the linear Seebeck coefficient:

$$S = S_s - \left.\frac{\partial V_{\rm xc}}{\partial \Delta T}\right|_{\substack{\Delta V=0\\ \Delta T=0}}, \tag{5.18}$$

where $S_s = -\frac{L_s}{G_s}$ is KS Seebeck coefficient (this terms exactly corresponds to the result that one obtains for the linear Seebeck coefficient within the LB+DFT approach) and the second term of eq. (5.18) is the xc contribution. Eq. (5.18) is one of the central results of the present chapter. It is formally exact and expresses the linear Seebeck coefficient of a general interacting system solely in terms of i-DFT quantities.

For the SIAM the Seebeck coefficient can be calculated beyond the linear response regime. We start by defining the following quantities

$$G_{s,\alpha} = -\frac{\gamma}{2}\int d\omega f'_\alpha(\omega_\alpha)A_s(\omega), \tag{5.19a}$$

$$L_{s,\alpha} = -\frac{1}{T_\alpha}\frac{\gamma}{2}\int d\omega f'_\alpha(\omega_\alpha)\omega_\alpha A_s(\omega), \tag{5.19b}$$

and $G_\pm = G_{s,R}\pm G_{s,L}$, $L_\pm = L_{s,R}\pm L_{s,L}$. The numerator of eq. (5.13) can be calculated directly from eq. (5.1b)

$$\begin{aligned}\frac{dI}{d\Delta T} &= \int d\omega\left[\frac{1}{2}f'_L(\omega_L)(-\frac{\omega_L}{T_L}-\frac{dV_{\rm xc}}{d\Delta T})-\frac{1}{2}f'_R(\omega_R)(+\frac{\omega_R}{T_R}+\frac{dV_{\rm xc}}{d\Delta T})\right]A_s(\omega)\\ &\quad -\int d\omega\left[f_L(\omega_L)-f_R(\omega_R)\right]A'_s(\omega)\frac{dv_s}{d\Delta T} \qquad (5.20)\\ &= \frac{1}{2}L_+ + \frac{1}{2}G_+\frac{dV_{\rm xc}}{d\Delta T}+G_-\frac{dv_{\rm Hxc}}{d\Delta T}. \qquad (5.21)\end{aligned}$$

We also require the calculation of the auxiliary term

$$\begin{aligned}\frac{dn}{d\Delta T} =& \int d\omega \left[\frac{1}{2}f_L'(\omega_L)(-\frac{\omega_L}{T_L} - \frac{dV_{\rm xc}}{d\Delta T}) + \frac{1}{2}f_R'(\omega_R)(+\frac{\omega_R}{T_R} + \frac{dV_{\rm xc}}{d\Delta T})\right] A_s(\omega) \\ & - \int d\omega \left[f_L(\omega_L) + f_R(\omega_R)\right] A_s'(\omega)\frac{dv_s}{d\Delta T} \qquad (5.22) \\ =& -\frac{1}{\gamma}\left(L_- + \frac{dV_{\rm xc}}{d\Delta T}G_- + 2G_+\frac{dv_{\rm Hxc}}{d\Delta T}\right). \qquad (5.23)\end{aligned}$$

Expanding out the total derivatives of the functionals

$$\frac{dV_{\rm xc}}{d\Delta T} = \frac{dV_{\rm xc}}{dn}\frac{dn}{d\Delta T} + \frac{dV_{\rm xc}}{dI}\frac{dI}{d\Delta T} + \frac{\partial V_{\rm xc}}{\partial \Delta T}, \qquad (5.24)$$

$$\frac{dv_{\rm Hxc}}{d\Delta T} = \frac{dv_{\rm Hxc}}{dn}\frac{dn}{d\Delta T} + \frac{dv_{\rm Hxc}}{dI}\frac{dI}{d\Delta T} + \frac{\partial v_{\rm Hxc}}{\partial \Delta T}, \qquad (5.25)$$

eqs. (5.21) and (5.23) become a coupled system that can be solved analytically.

On the other hand the denominator of eq. (5.13) corresponds to the finite-bias differential conductance calculated in ref. [45]

$$\frac{dI}{dV} = \frac{1}{D}\left(\frac{1}{2}G_+ + \frac{4}{\gamma}G_{s,L}G_{s,R}\frac{\partial v_{\rm Hxc}}{\partial n}\right), \qquad (5.26)$$

with

$$\begin{aligned}D =& 1 + \frac{1}{\gamma}G_-\frac{\partial V_{\rm xc}}{\partial n} + \frac{2}{\gamma}G_+\frac{\partial v_{\rm Hxc}}{\partial n} - \frac{1}{2}G_+\frac{\partial V_{\rm xc}}{\partial I} - G_-\frac{\partial v_{\rm Hxc}}{\partial I} \\ & + \frac{4}{\gamma}G_{s,L}G_{s,R}\left(\frac{\partial v_{\rm Hxc}}{\partial I}\frac{\partial V_{\rm xc}}{\partial n} - \frac{\partial v_{\rm Hxc}}{\partial n}\frac{\partial V_{\rm xc}}{\partial I}\right). \qquad (5.27)\end{aligned}$$

The combination of eq. (5.26) with the solution for $\frac{dI}{d\Delta T}$ leads to the final expression of the Seebeck coefficient

$$\begin{aligned}S = \frac{dV}{d\Delta T} =& -\frac{\partial V_{\rm xc}}{\partial \Delta T} - \frac{\frac{L_+}{2} + \gamma^{-1}\left(L_{s,R}G_{s,L} + L_{s,L}G_{s,R}\right)\left[\frac{dV_{\rm xc}}{dn} + 2\frac{dv_{\rm Hxc}}{dn}\right]}{\frac{G_+}{2} + 4\gamma^{-1}G_{s,R}G_{s,L}\frac{dv_{\rm Hxc}}{dn}} \\ & - \frac{\frac{\partial v_{\rm Hxc}}{\partial \Delta T}\left(G_- - 4\gamma^{-1}G_{s,R}G_{s,L}\frac{dV_{\rm xc}}{dn}\right)}{\frac{G_+}{2} + 4\gamma^{-1}G_{s,R}G_{s,L}\frac{dv_{\rm Hxc}}{dn}}. \qquad (5.28)\end{aligned}$$

The linear Seebeck coefficient eq. (5.18) is directly recovered from eq. (5.28) in the linear response regime, i.e, when $V = \Delta T = 0$ and $\frac{dV_{\rm xc}}{dn} = 0$ since $V_{\rm xc}[n, I = 0] = 0$.

Eq. (5.18) also arises as a generalization of a recent developed expression of the linear Seebeck coefficient valid for the SIAM and the CB regime [42]. In fact,

given the structural property of the xc potentials of eqs. (5.3) as the sum of two pieces (each one depending only on the temperature of one of the leads), it can be easily shown that this structure leads to the xc contribution to the many-body Seebeck coefficient (eq. (5.18)) of the form

$$S_{\rm xc}^{CB} = \left.\frac{\partial V_{\rm xc}}{\partial \Delta T}\right|_{\substack{V=0\\ \Delta T=0}} = -\left.\frac{\partial v_{\rm Hxc}}{\partial T}\right|_{\substack{V=0\\ \Delta T=0}}. \tag{5.29}$$

While this result holds for any approximation with the structural property mentioned above, for the special case of the functionals of eq. (5.3) it reduces exactly to the expression obtained in ref. [42].[2]

In the SIAM, the non-interacting contribution of eq. (5.18) can be expressed in an analytical and closed form as (see appendix B)

$$S_s = \frac{-1}{T}\frac{\int f'(\omega)\frac{\omega d\omega}{(\omega-v)^2+\frac{\gamma^2}{4}}}{\int f'(\omega)\frac{d\omega}{(\omega-v)^2+\frac{\gamma^2}{4}}} = -\frac{1}{T}\frac{\mathrm{Im}\Big[(\frac{\gamma}{2}+iv_s)\psi^{(1)}(\frac{1}{2}+\frac{\gamma}{4\pi T}+i\frac{v_s}{2\pi T})\Big]}{\mathrm{Im}\Big[i\psi^{(1)}(\frac{1}{2}+\frac{\gamma}{4\pi T}+i\frac{v_s}{2\pi T})\Big]}. \tag{5.30}$$

The combination of eq. (5.9) and eq. (5.18) opens the way to explore the linear Seebeck coefficient from the CB to the Kondo regime. As first step we analyze the relative magnitude of the KS Seebeck coefficient (S_s) and the xc correction ($S_{\rm xc}$) as a function of the gate voltage and the correlation strength. In fig. 5.6, we can see that, as expected, the xc contribution becomes dominant for almost any temperature as U/γ increases from 1 (fig. 5.6a) to 8 (fig. 5.6d), but also for intermediate values, $U/\gamma = 3$, the two terms have a comparable magnitude for any value of the gate voltage. Notice that, since both potential and temperature are evaluated in units of γ, S and $S_{\rm xc}$ are dimensionless. In fig. 5.7 we compare our results with the NRG ones of ref. [88] for fixed gate potential as a function of temperature. Again, similar to fig. 5.6, the panels report calculated values from weak (a) to strong correlations (d) in the dot. As expected we find a very good agreement between i-DFT and NRG for $T \gtrsim T_K$. For lower temperatures, i-DFT shows small discrepancies with respect to the reference result which exhibits a different evolution of the local minimum of the Seebeck coefficient when increasing the interaction.

[2]Notice that by comparing eq. (5.29) and eq. (5.18) one arrives at $S = S_s - S_{\rm xc}$. This reflects the standard definition $V_{\rm xc} = V_s - V$.

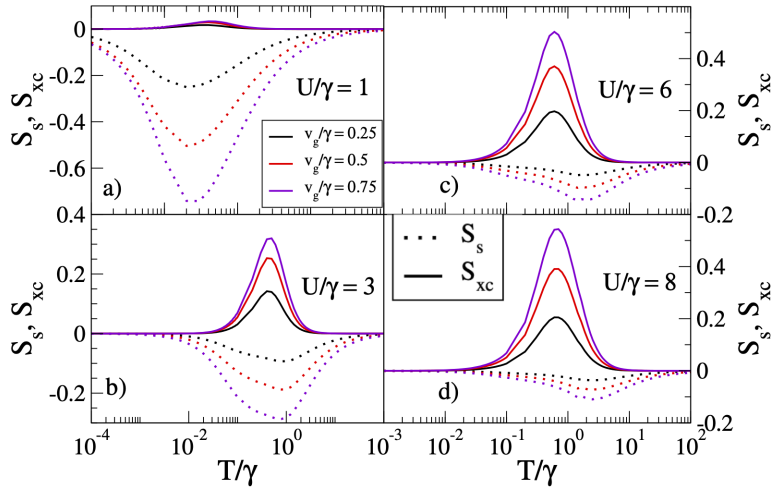

Figure 5.6: Linear KS Seebeck coefficient S_s and xc correction $S_{\rm xc}$ as function of temperature for different gate voltages and correlation strengths U/γ.

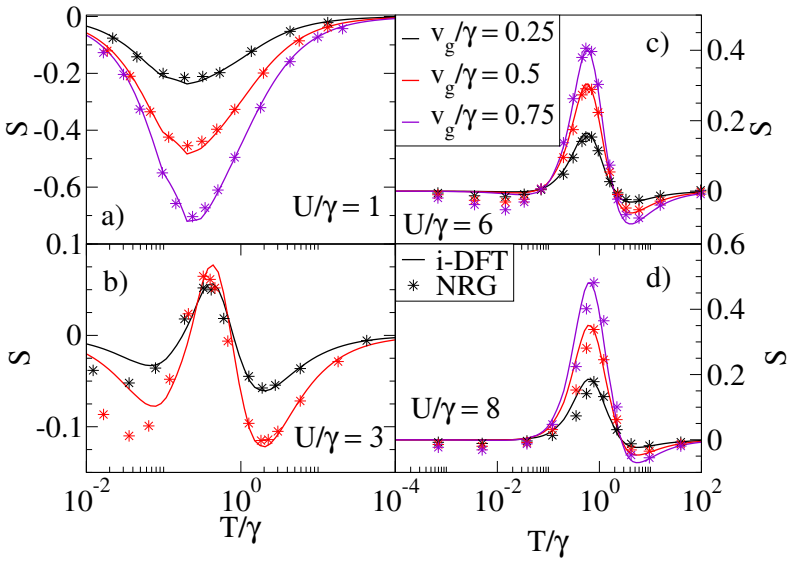

Figure 5.7: Comparison of the Seebeck coefficient obtained with i-DFT with the NRG results of ref. [88] as function of temperature for different gate voltages and correlation strengths U/γ.

In fig. 5.8, we show the Seebeck coefficient as function of the gate voltage for different values of the temperature and again compare with NRG results of ref. [88]. As already noticed above, for low temperatures there are discrepancies at certain gate values although with our i-DFT approach we manage to obtain the qualitative behaviour of the NRG results. For $T/\gamma \gtrsim 1$, on the other hand, the i-DFT results are in excellent agreement with the NRG ones.

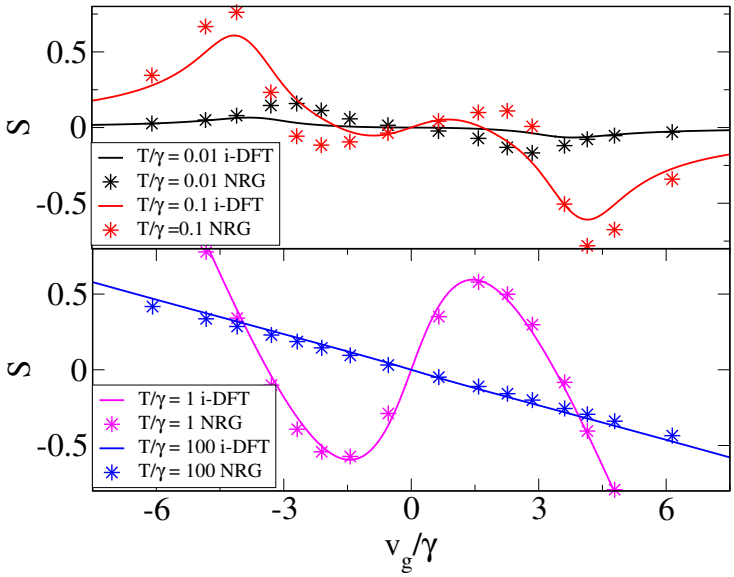

Figure 5.8: Comparison of the Seebeck coefficient obtained with i-DFT with the NRG results of ref. [88].S is shown as function of the gate voltage for different temperatures and for strong correlations $U/\gamma = 8$.

5.2.3 Thermal conductance

To conclude the chapter we derive the electronic contribution to the thermal conductance as function of terms accessible to iDFT. This coefficient is defined as $\kappa = \frac{dQ}{d\Delta T}\Big|_{\substack{I=0\\Q=0}}$, where Q represents the heat current of the system. Since the i-DFT theorem only guarantees the correct description of the density in the central region and the electrical current though it, the corresponding KS heat current (and therefore also the thermal conductance) need not coincide with the corresponding heat current of the interacting system. This situation is completely analogous to the description of the electrical current (and the electrical conductance) within the LB+DFT framework.

Nevertheless, by considering the linear response relationship between the currents (I, Q) and the potentials $(V, \Delta T)$, it is well known [92, 93] that the thermal conductance can be written in terms of the conductance matrix elements as (see section 6.1 for detailed derivation)

$$\kappa = \frac{dQ}{d\Delta T}\bigg|_{\substack{I=0\\Q=0}} = \frac{1}{T}\left(L_{22} - \frac{L_{12}^2}{L_{11}}\right), \tag{5.31}$$

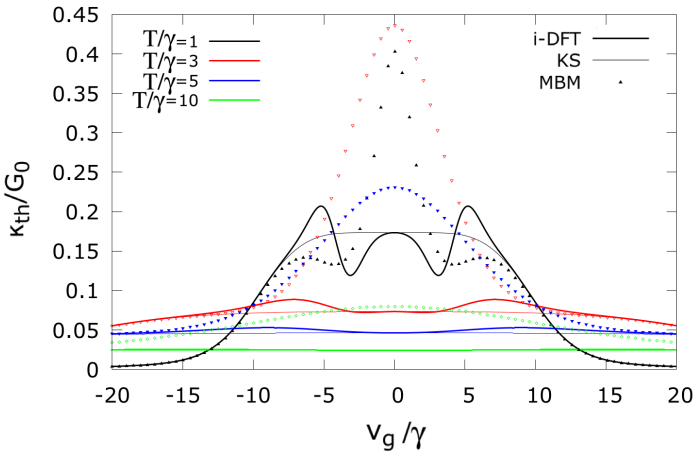

Figure 5.9: Thermal conductance as function of the gate voltage for different temperatures and strong correlations $U/\gamma = 8$. The thick line corresponds to the i-DFT result from eq. (5.34), the thin line to the KS result and the dots to the MBM (see eq. (6.23c)).

where $L_{11} = \frac{dI}{dV}\Big|_{\substack{V=0\\ \Delta T=0}} = G$, $L_{12} = T\,\frac{dI}{d\Delta T}\Big|_{\substack{V=0\\ \Delta T=0}} = -STG$ and $L_{22} = T\,\frac{dQ}{d\Delta T}\Big|_{\substack{V=0\\ \Delta T=0}}$. In order to derive the L_{22} contribution, we make use of the accessible heat current within the i-DFT formalism, i.e

$$Q^{\mathrm{i-DFT}} = \int d\omega \left(f_L(\omega - \frac{V_s}{2}) - f_R(\omega - \frac{V_s}{2}) \right) (\omega - \frac{V_s}{2}) \mathcal{T}_s(\omega), \tag{5.32}$$

where we explicitly label $Q^{\mathrm{i-DFT}}$ to emphasize that this is not always the heat current of the many body system, even if we use the exact $(v_{\mathrm{Hxc}}, V_{\mathrm{xc}})$. From eq. (5.32) we can proceed to calculate

$$\begin{aligned} L_{22} = \frac{dQ^{\mathrm{i-DFT}}}{d\Delta T}\Big|_{\substack{V=0\\ \Delta T=0}} &= -\int d\omega f'(\omega)(\frac{\omega^2}{T} + w\frac{dV_{\mathrm{xc}}}{d\Delta T})\mathcal{T}_s(\omega) \\ &= \frac{1}{T} L_{22,s} + L_{12,s}\frac{dV_{\mathrm{xc}}}{d\Delta T}, \end{aligned} \tag{5.33}$$

Making use of eq. (5.24) and rewriting the xc derivatives that appear in terms of both the interacting and non-interacting electrical conductance and Seebeck coefficient, the thermal conductance in the i-DFT framework can be written as

$$\kappa^{\mathrm{i-DFT}} = \kappa_s + G\left(S\left(S_s - \frac{G^2}{G_s^2} S \right) + S_s^2 \right) - G_s S_s^2. \tag{5.34}$$

From eq. (5.34) one can appreciate how the KS thermal conductance κ_s is recovered in the non-interacting situation. In fig. 5.9 we compare the thermal conductance

from the MBM with the KS and the i-DFT. Although the i-DFT result captures some new contributions, the results are still far away from the correct behaviour. In fact, one can appreciate that at the particle-hole symmetric point $\kappa^{\mathrm{i-DFT}} = \kappa_s$ (since $S(v_g = 0) = 0$), while the correct MBM thermal conductance shows the evolution of a peak as the temperature is increased.

This chapter is based on the article [94].

6

Steady-state Density Functional Theory Formalism for both Electrical and Heat Transport

Contents

6.1 Formalism 78
6.1.1 Kohn-Sham equations of iq-DFT 81
6.2 Linear Response 83
6.3 Application to the single impurity Anderson Model . 86
6.3.1 Reverse engineering from the Many-Body Model 87
6.3.2 Numerical results 91

In this chapter we will develop a new DFT formalism for the description of both charge and electronic transport. This framework, which we call iq-DFT [94], emerges as an extension of the previously described i-DFT. We emphasize that in this formalism we only include heat transport due to the electrons but don't deal with heat transport due to other degrees of freedom (e.g. phonons). First we introduce the formalism for the multi-terminal situation through the corresponding theorem. Then we establish the linear response regime of the formalism for the two terminal case and we derive general expressions for the transport coefficients. Finally, we apply the theory to the SIAM, where the xc contributions are analytically RE in

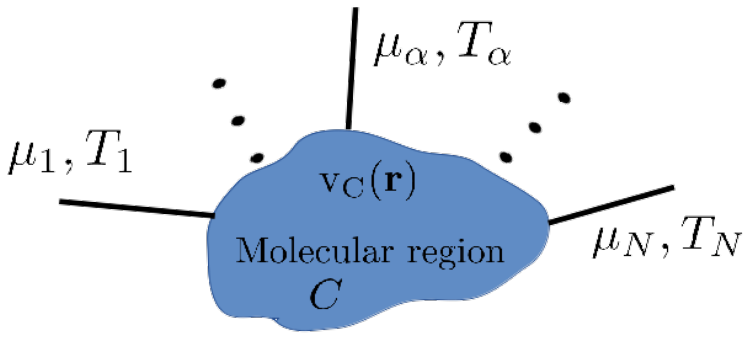

Figure 6.1: Schematic illustration of the multi-terminal quantum transport setup.

the CB regime and the transport coefficients are benchmarked against the MBM.

6.1 Formalism

We consider a general setup for electronic transport which consists of a central molecular junction (C) coupled to $\mathcal{N}$ electrodes, see fig. 6.1. The electrodes are in (local) thermal equilibrium with temperatures T_α and chemical potentials $\mu_\alpha = \mu + V_\alpha$, with $\alpha = 1, \ldots, \mathcal{N}$. The central region C is subject to an electrostatic potential $v(\mathbf{r})$ generated by, e.g., the nuclei in the molecular junction and/or an external gate potential which vanishes deep inside the electrodes. The system can be driven out of equilibrium by a finite thermal gradient ΔT_α and/or an external DC bias V_α to each of the leads. We assume that these perturbations in the long-time limit lead to steady-state electrical currents (I_α) as well as energy and heat currents (W_α and Q_α, respectively). Here the currents $I_\alpha, W_\alpha, Q_\alpha$ are the electrical, energy and heat currents flowing from lead α to the central region C.

We aim to construct a formally exact density functional framework, which we call iq-DFT, to describe such a steady-state and reproduce the currents of the interacting system through the corresponding, effectively non-interacting KS system. To this end, we extend the i-DFT, which in principle captures the steady-state density $n(\mathbf{r})$ in the central region C, as well as the steady currents I_α [95]. In the two terminal setup, by construction, in the linear-response regime, i-DFT gives access to

the (many-body) electrical conductance and can also describe the Seebeck coefficient (see eq. (5.18)). On the other hand, the energy or heat currents are not guaranteed to be reproduced in i-DFT and therefore also the thermal conductance is not captured.

In our new iq-DFT framework for the description of both electrical *and* thermal transport, we establish a one-to-one map between "densities" $(n(\mathbf{r}), I_1, \ldots, I_{\mathcal{N}-1}, Q_1, \ldots, Q_{\mathcal{N}-1})$ and "potentials" $(v(\mathbf{r}), V_1, \ldots, V_{\mathcal{N}-1}, \Psi_1, \ldots, \Psi_{\mathcal{N}-1})$, where $\Psi_\alpha = \Delta T_\alpha / T$ is the normalized thermal gradient and $T = \sum_\alpha (T_\alpha)/\mathcal{N}$ is the background temperature. In (two-terminal) linear response, iq-DFT gives access not only to the electrical conductance and the Seebeck coefficient but also to the electronic contribution to the thermal conductance, see Section 6.2.

In the following, we adopt the sign convention that currents flowing into the central region are positive. Due to charge and energy conservation, the steady-state electrical/energy currents flowing in is equal to the steady-state electrical/energy currents flowing out, i.e., $\sum I_\alpha = 0$, $\sum W_\alpha = 0$ (energy current) and $\sum Q_\alpha = -\sum I_\alpha V_\alpha$ (heat current).

The foundation of the multi-terminal iq-DFT rests on the following theorem which establishes the one-to-one correspondence between the basic variables of the theory $(n(\mathbf{r}), I_1, \ldots, I_{\mathcal{N}-1}, Q_1, \ldots, Q_{\mathcal{N}-1})$ and the related driving forces or potentials $(v(\mathbf{r}), V_1, \ldots, V_{\mathcal{N}-1}, \Psi_1, \ldots, \Psi_{\mathcal{N}-1})$ in a (gate dependent) finite region around $V_\alpha = 0$ and $\Psi_\alpha = 0$ for all α.

Theorem: For any finite temperature T and fixed electrostatic potential in the leads, there exists a one-to-one correspondence between the set of "densities" $(n(\mathbf{r}), I_1, \ldots, I_{\mathcal{N}-1}, Q_1, \ldots, Q_{\mathcal{N}-1})$ and the set of "potentials" $(v(\mathbf{r}), V_1, \ldots, V_{\mathcal{N}-1}, \Psi_1, \ldots, \Psi_{\mathcal{N}-1})$ in a (gate dependent) finite region around $V_\alpha = 0$ and $\Psi_\alpha = 0$ for all $\alpha = 1, \ldots, \mathcal{N}-1$.

Proof: The existence of the invertible map can be proven by showing that

the determinant of the Jacobian

$$J = \det \left(\begin{array}{cccccc} \frac{\delta n(\mathbf{r})}{\delta v(\mathbf{r}')} & \frac{\delta n(\mathbf{r})}{\delta V_1} & \cdots & \frac{\delta n(\mathbf{r})}{\delta V_{\mathcal{N}-1}} & \frac{\delta n(\mathbf{r})}{\delta \Psi_1} & \cdots & \frac{\delta n(\mathbf{r})}{\delta \Psi_{\mathcal{N}-1}} \\ \frac{\delta I_1}{\delta v(\mathbf{r}')} & \frac{\delta I_1}{\delta V_1} & \cdots & \frac{\delta I_1}{\delta V_{\mathcal{N}-1}} & \frac{\delta I_1}{\delta \Psi_1} & \cdots & \frac{\delta I_1}{\delta \Psi_{\mathcal{N}-1}} \\ \vdots & \vdots & \ddots & \vdots & \vdots & \ddots & \vdots \\ \frac{\delta I_{\mathcal{N}-1}}{\delta v(\mathbf{r}')} & \frac{\delta I_{\mathcal{N}-1}}{\delta V_1} & \cdots & \frac{\delta I_{\mathcal{N}-1}}{\delta V_{\mathcal{N}-1}} & \frac{\delta I_{\mathcal{N}-1}}{\delta \Psi_1} & \cdots & \frac{\delta I_N - 1}{\delta \Psi_{\mathcal{N}-1}} \\ \frac{\delta Q_1}{\delta v(\mathbf{r}')} & \frac{\delta Q_1}{\delta V_1} & \cdots & \frac{\delta Q_1}{\delta V_{\mathcal{N}-1}} & \frac{\delta Q_1}{\delta \Psi_1} & \cdots & \frac{\delta Q_1}{\delta \Psi_{\mathcal{N}-1}} \\ \vdots & \vdots & \ddots & \vdots & \vdots & \ddots & \vdots \\ \frac{\delta Q_{\mathcal{N}-1}}{\delta v(\mathbf{r}')} & \frac{\delta Q_{\mathcal{N}-1}}{\delta V_1} & \cdots & \frac{\delta Q_{\mathcal{N}-1}}{\delta V_{\mathcal{N}-1}} & \frac{\delta Q_{\mathcal{N}-1}}{\delta \Psi_1} & \cdots & \frac{\delta Q_{\mathcal{N}-1}}{\delta \Psi_{\mathcal{N}-1}} \end{array} \right) \Bigg|_{\substack{\{V_\beta\}=0 \\ \{\Psi_\beta\}=0}}, \tag{6.1}$$

is non-vanishing.

Since a change in the gate voltage can not produce a persistent current in the linear regime we have

$$\left.\frac{\delta I_\alpha}{\delta v(\mathbf{r})}\right|_{\substack{\{V_\beta\}=0 \\ \{\Psi_\beta\}=0}} = 0, \quad \left.\frac{\delta Q_\alpha}{\delta v(\mathbf{r})}\right|_{\substack{\{V_\beta\}=0 \\ \{\Psi_\beta\}=0}} = 0; \tag{6.2}$$

and from Onsager's reciprocal relation [93] also $\left.\frac{\partial n(\mathbf{r})}{\partial V_\alpha}\right|_0 = \left.\frac{\partial n(\mathbf{r})}{\partial \Psi_\alpha}\right|_0 = 0$ for $\alpha = 1, \ldots, \mathcal{N}-1$. Therefore we can write eq. (6.1) as

$$J = \det(\chi(\mathbf{r}, \mathbf{r}'))\det(\mathbf{L}) \tag{6.3}$$

where $\chi(\mathbf{r}, \mathbf{r}') = \left.\frac{\delta n(\mathbf{r})}{\delta v(\mathbf{r}')}\right|_{\substack{\{V_\beta\}=0 \\ \{\Psi_\beta\}=0}}$ is the static equilibrium density response function and $\mathbf{L}$ provides the linear response relationship between the current vector $\mathbf{I}^\intercal = (I_1, \ldots, I_{\mathcal{N}-1}, Q_1, \ldots, Q_{\mathcal{N}-1})$ and the potential vector $\mathbf{\Phi}^\intercal = (V_1, \ldots, V_{\mathcal{N}-1}, \Psi_1, \ldots, \Psi_{\mathcal{N}-1})$

$$\mathbf{I} = \begin{pmatrix} I_1 \\ \vdots \\ I_{\mathcal{N}-1} \\ Q_1 \\ \vdots \\ Q_{\mathcal{N}-1} \end{pmatrix} = \left(\begin{array}{cccccc} \frac{\delta I_1}{\delta V_1} & \cdots & \frac{\delta I_1}{\delta V_{\mathcal{N}-1}} & \frac{\delta I_1}{\delta \Psi_1} & \cdots & \frac{\delta I_1}{\delta \Psi_{\mathcal{N}-1}} \\ \vdots & \ddots & \vdots & \vdots & \ddots & \vdots \\ \frac{\delta I_{\mathcal{N}-1}}{\delta V_1} & \cdots & \frac{\delta I_{\mathcal{N}-1}}{\delta V_{\mathcal{N}-1}} & \frac{\delta I_{\mathcal{N}-1}}{\delta \Psi_1} & \cdots & \frac{\delta I_1}{\delta \Psi_{\mathcal{N}-1}} \\ \frac{\delta Q_1}{\delta V_1} & \cdots & \frac{\delta Q_1}{\delta V_{\mathcal{N}-1}} & \frac{\delta Q_1}{\delta \Psi_1} & \cdots & \frac{\delta Q_1}{\delta \Psi_{\mathcal{N}-1}} \\ \vdots & \ddots & \vdots & \vdots & \ddots & \vdots \\ \frac{\delta Q_{\mathcal{N}-1}}{\delta V_1} & \cdots & \frac{\delta Q_{\mathcal{N}-1}}{\delta V_{\mathcal{N}-1}} & \frac{\delta Q_{\mathcal{N}-1}}{\delta \Psi_1} & \cdots & \frac{\delta Q_{\mathcal{N}-1}}{\delta \Psi_{\mathcal{N}-1}} \end{array} \right) \Bigg|_{\mathbf{\Phi}=0} \begin{pmatrix} V_1 \\ \vdots \\ V_{\mathcal{N}-1} \\ \Psi_1 \\ \vdots \\ \Psi_{\mathcal{N}-1} \end{pmatrix} = \mathbf{L}\mathbf{\Phi}. \tag{6.4}$$

It has already been shown [41] that, for any finite temperature T, we have $det(\chi(\mathbf{r}, \mathbf{r}')) < 0$. Therefore, in order to complete the proof of the theorem, it remains to be show that $\det(\mathbf{L}) \neq 0$.

In the steady-state the time-derivative of the entropy $\mathcal{S}$ equals the variation of the entropy current $\mathsf{S} = Q/T$ along the central molecular region. By construction, in the linear response regime we have [96–98]

$$\dot{\mathcal{S}} = \frac{1}{T}\sum_{\alpha=1}^{\mathcal{N}-1}(I_\alpha V_\alpha + Q_\alpha \Psi_\alpha) = \frac{1}{T}\mathbf{\Phi}^\intercal \mathbf{I} = \frac{1}{T}\mathbf{\Phi}^\intercal \mathbf{L}\mathbf{\Phi} \tag{6.5}$$

where we used eq. (6.4) in the last steps. From the second law of the thermodynamics, we know that $\dot{\mathcal{S}} \geq 0$ where the equality sign holds at equilibrium. Therefore $\mathbf{\Phi}^\intercal \mathbf{L}\mathbf{\Phi} > 0$ for all $\mathbf{\Phi} \in \mathbb{R}^{\mathcal{N}-1}\backslash\{\mathbf{0}\}$ and the $\mathbf{L}$ matrix is positive definite. From eq. (6.3) we can therefore conclude that $J \neq 0$ completing the proof of the multi-terminal iq-DFT theorem.

In the following sections of the present chapter we will restrict ourselves to the two-terminal case (an alternative demonstration of the one-to-one correspondence can be found in ref. [94]) where we adopt the same sign convention for the currents, i.e., $I \equiv I_L = -I_R$ (electrical current), $W \equiv W_L = -W_R$ (energy current) and $Q \equiv Q_L = -IV - Q_R$ (heat current).

It is worth mentioning that an equivalent formulation in the two terminal situation stems from considering as third basic variable the energy current W instead of Q. The theory thus leads to a one-to-one correspondence between $(n(\mathbf{r}), I, W)$ and the trio of potentials $(v(\mathbf{r}), V - \mu_L\Psi, \Psi)$. The two formulations are related through [99]

$$W_\alpha = Q_\alpha + \mu_\alpha I_\alpha. \tag{6.6}$$

6.1.1 Kohn-Sham equations of iq-DFT

The iq-DFT theorem holds for any form of the interaction, in particular also for the non-interacting case. In order to establish the Kohn-Sham (KS) scheme, we make the usual assumption of non-interacting representability, i.e., that there exists a unique trio of potentials $(v_s(\mathbf{r}), V_s, \Psi_s)$ for a non-interacting system, the Kohn-Sham system, which exactly reproduces the densities $(n(\mathbf{r}), I, Q)$ of the interacting system

with potentials $(v(\mathbf{r}), V, \Psi)$. Following the standard KS procedure, the xc potentials of the iq-DFT framework are then defined as

$$v_{\mathrm{Hxc}}[n,I,Q](\mathbf{r}) = v_s[n,I,Q](\mathbf{r}) - v[n,I,Q](\mathbf{r}), \tag{6.7a}$$

$$V_{\mathrm{xc}}[n,I,Q] = V_s[n,I,Q] - V[n,I,Q], \tag{6.7b}$$

$$\Psi_{\mathrm{xc}}[n,I,Q] = \Psi_s[n,I,Q] - \Psi[n,I,Q]. \tag{6.7c}$$

The self-consistent coupled KS equations for the densities read ($\int \equiv \int_{-\infty}^{\infty} \frac{d\omega}{2\pi}$ in the following)

$$n(\mathbf{r}) = 2\sum_{\alpha=L,R}\int f(\frac{\omega-\mu_{s,\alpha}}{T_{s,\alpha}})A_{s,\alpha}(\mathbf{r},\omega), \tag{6.8a}$$

$$I = 2\sum_{\alpha=L,R}\int f(\frac{\omega-\mu_{s,\alpha}}{T_{s,\alpha}})s_\alpha\mathcal{T}_s(\omega), \tag{6.8b}$$

$$Q = 2\sum_{\alpha=L,R}\int f(\frac{\omega-\mu_{s,\alpha}}{T_{s,\alpha}})s_\alpha(\omega-\mu_{s,L})\mathcal{T}_s(\omega), \tag{6.8c}$$

where $f(x) = [1+\exp(x)]^{-1}$ is the Fermi function, $\mu_{s,\alpha} = \mu + V_{s,\alpha}$, $T_{s,\alpha} = T(1+s_\alpha\Psi_s/2)$ and $s_{L/R} = \pm 1$. We remind the reader the definitions of the partial spectral function $A_{s,\alpha}(\mathbf{r},\omega) = \langle\mathbf{r}|\,\mathbf{G}(\omega)\mathbf{\Gamma}_\alpha(\omega)\mathbf{G}^\dagger(\omega)\,|\mathbf{r}\rangle$, with $\mathbf{G}(\omega)$ and $\mathbf{\Gamma}_\alpha(\omega)$ the KS Green's function and broadening matrices, respectively, and the KS transmission function $\mathcal{T}_s(\omega) = \mathrm{Tr}\left\{\mathbf{G}(\omega)\mathbf{\Gamma}_L(\omega)\mathbf{G}^\dagger(\omega)\mathbf{\Gamma}_R(\omega)\right\}$. Finally, the energy current follows directly from eqs. (6.6) and (6.8)

$$W = 2\sum_{\alpha=L,R}\int f(\frac{\omega-\mu_{s,\alpha}}{T_{s,\alpha}})s_\alpha\omega\mathcal{T}_s(\omega). \tag{6.9}$$

Eqs. (6.8a) and (6.8b) have the same structure as the KS equations of the original i-DFT formulation, except that in the present formalism the thermal gradient along the central region is not a parameter anymore but a basic potential which depends on the densities of the system. Therefore, the only possible parametric temperature dependence in the approximations for the functionals eqs. (6.7) is through the average temperature T.

6.2 Linear Response

In this section, we develop the linear response formalism for iq-DFT which leads to expressions for the linear transport coefficients G, S, and κ purely in terms of quantities accessible by the theory.

To linear order, the relationship between the currents (I, Q) resulting from application of the potentials (V, Ψ) reads

$$\begin{pmatrix} I \\ Q \end{pmatrix} = \mathbf{L} \begin{pmatrix} V \\ \Psi \end{pmatrix} = \begin{pmatrix} L_{11} & L_{12} \\ L_{21} & L_{22} \end{pmatrix} \begin{pmatrix} V \\ \Psi \end{pmatrix} \tag{6.10}$$

with $L_{21} = L_{12}$ from Onsager's relation. The conductance matrix $\mathbf{L}$ can be expressed in terms of the transport coefficients as [92]

$$\mathbf{L} = \begin{pmatrix} G & -TGS \\ -TGS & T\kappa + T^2GS^2 \end{pmatrix} \tag{6.11}$$

where G is the electrical conductance, S is the Seebeck coefficient and κ is the thermal(heat) conductance. Equivalently, we can use eq. (6.11) to express the transport coefficients in terms of the matrix elements L_{ij} as

$$G = \left.\frac{\partial I}{\partial V}\right|_{\substack{V=0 \\ \Psi=0}} = L_{11}, \tag{6.12a}$$

$$S = \left.\frac{\partial V}{\partial \Delta T}\right|_{\substack{I=0 \\ Q=0}} = -\frac{1}{T}\frac{L_{12}}{L_{11}}, \tag{6.12b}$$

$$\kappa = \left.\frac{\partial Q}{\partial \Delta T}\right|_{\substack{I=0 \\ Q=0}} = \frac{1}{T}\left(L_{22} - \frac{L_{12}^2}{L_{11}}\right). \tag{6.12c}$$

The same current variations as in eq. (6.10) can be expressed in terms of the KS system

$$\begin{pmatrix} I \\ Q \end{pmatrix} = \mathbf{L}_s \begin{pmatrix} V + V_{\mathrm{xc}} \\ \Psi + \Psi_{\mathrm{xc}} \end{pmatrix}, \tag{6.13}$$

where we have used the definition of the KS potentials eqs. (6.7) and that $I_s = I$ and $Q_s = Q$ by the KS construction. In the linear response regime, the changes in the xc potentials can be written as

$$\begin{pmatrix} V_{\mathrm{xc}} \\ \Psi_{\mathrm{xc}} \end{pmatrix} = \mathbf{F}_{\mathrm{xc}} \begin{pmatrix} I \\ Q \end{pmatrix} = \mathbf{F}_{\mathrm{xc}}\mathbf{L} \begin{pmatrix} V \\ \Psi \end{pmatrix}, \tag{6.14}$$

with the matrix of xc derivatives $\mathbf{F}_{\mathrm{xc}}$ defined by

$$\mathbf{F}_{\mathrm{xc}} = \left(\begin{array}{cc} \frac{\partial V_{\mathrm{xc}}}{\partial I} & \frac{\partial V_{\mathrm{xc}}}{\partial Q} \\ \frac{\partial \Psi_{\mathrm{xc}}}{\partial I} & \frac{\partial \Psi_{\mathrm{xc}}}{\partial Q} \end{array} \right) \Bigg|_{\substack{I=0 \\ Q=0}} \tag{6.15}$$

and eq. (6.10) has been used. Combining eqs. (6.10), (6.13), and (6.15), and using the fact that V and Ψ are arbitrary, we arrive at the Dyson equation

$$\mathbf{L} = \mathbf{L}_s + \mathbf{L}_s \mathbf{F}_{\mathrm{xc}} \mathbf{L}, \tag{6.16}$$

or, equivalently,

$$\mathbf{F}_{\mathrm{xc}} = \mathbf{L}_s^{-1} - \mathbf{L}^{-1} = \mathbf{R}_s - \mathbf{R}. \tag{6.17}$$

Here, $\mathbf{L}$ and $\mathbf{L}_s$ are the interacting and KS conductance matrices where each element is evaluated at $(V = 0, \Psi = 0)$ and $(V_s = 0, \Psi_s = 0)$, respectively. Similarly, $\mathbf{R} = \mathbf{L}^{-1}$ and $\mathbf{R}_s = \mathbf{L}_s^{-1}$ are the interacting and KS resistance matrices where each element is evaluated at $(I = 0, Q = 0)$. As a consequence of the Onsager's relations between the cross terms in the conductance matrices, from eq. (6.17) it follows

$$\left. \frac{\partial V_{\mathrm{xc}}}{\partial Q} \right|_{\substack{I=0 \\ Q=0}} = \left. \frac{\partial \Psi_{\mathrm{xc}}}{\partial I} \right|_{\substack{I=0 \\ Q=0}}. \tag{6.18}$$

We can express the $\mathbf{F}_{\mathrm{xc}}$ elements as function of the linear transport coefficients making use of eqs. (6.11) and (6.17) for the interacting and the KS system

$$\left. \frac{\partial V_{\mathrm{xc}}}{\partial I} \right|_{\substack{I=0 \\ Q=0}} = \frac{1}{G_s} + T\frac{S_s^2}{\kappa_s} - \frac{1}{G} - T\frac{S^2}{\kappa}, \tag{6.19a}$$

$$\left. \frac{\partial \Psi_{\mathrm{xc}}}{\partial I} \right|_{\substack{I=0 \\ Q=0}} = \left. \frac{\partial V_{\mathrm{xc}}}{\partial Q} \right|_{\substack{I=0 \\ Q=0}} = \frac{S_s}{\kappa_s} - \frac{S}{\kappa}, \tag{6.19b}$$

$$\left. \frac{\partial \Psi_{\mathrm{xc}}}{\partial Q} \right|_{\substack{I=0 \\ Q=0}} = \frac{1}{T\kappa_s} - \frac{1}{T\kappa}. \tag{6.19c}$$

These equations can be inverted to yield

$$\kappa = \frac{\kappa_s}{1 - T\frac{\partial \Psi_{\rm xc}}{\partial Q}\Big|_{\substack{I=0\\Q=0}} \kappa_s}, \tag{6.20a}$$

$$S = \frac{S_s - \kappa_s \frac{\partial V_{\rm xc}}{\partial Q}\Big|_{\substack{I=0\\Q=0}}}{1 - T\frac{\partial \Psi_{\rm xc}}{\partial Q}\Big|_{\substack{I=0\\Q=0}} \kappa_s}, \tag{6.20b}$$

$$G = \frac{G_s}{1 - \left(\frac{\partial V_{\rm xc}}{\partial I}\Big|_{\substack{I=0\\Q=0}} + \frac{TS^2}{\kappa} - \frac{TS_s^2}{\kappa_s}\right) G_s}. \tag{6.20c}$$

Eqs. (6.20) are exact expressions for the interacting (linear) transport coefficients in any molecular transport setup. They express the many-body transport coefficients in terms of quantities which are fully accessible within iq-DFT, i.e, the xc derivatives evaluated at $(I = 0, Q = 0)$ and the KS transport coefficients. The transport coefficients in iq-DFT exhibit increasing complexity: while the thermal conductance κ (eq. (6.20a)) only depends on the KS thermal conductance κ_s and $\frac{\partial \Psi_{\rm xc}}{\partial Q}$, the Seebeck coefficient depends on its KS contribution S_s, κ_s as well as the two xc derivatives, $\frac{\partial V_{\rm xc}}{\partial Q}$ and $\frac{\partial \Psi_{\rm xc}}{\partial Q}$. Finally, the electrical conductance depends on the three KS coefficients (κ_s, S_s, G_s) and the three xc derivatives through S and κ.

Using eqs. (6.20) for the iq-DFT transport coefficients, we now briefly discuss the relation of iq-DFT to other DFT-based frameworks for the description of steady-state transport. At first, we consider the simplest approximation which completely neglects the xc contributions to the transport coefficients, i.e., setting $V_{\rm xc} \approx 0$ and $\Psi_{\rm xc} \approx 0$. Then all linear transport coefficients reduce to the corresponding KS coefficients, i.e., we recover the standard LB+DFT approach. At the next level, we consider the relation to the original i-DFT formalism which is designed to give the exact electrical steady current. The i-DFT expression for the electrical conductance

$$G = \frac{G_s}{1 - \frac{\partial V_{\rm xc}^{\rm i-DFT}}{\partial I}\Big|_{I=0} G_s} \tag{6.21}$$

is exact, just as the corresponding iq-DFT expression (6.20c). Thus, we can establish the exact relation

$$\frac{\partial V_{\rm xc}^{\rm i-DFT}}{\partial I}\Big|_{I=0} = \frac{\partial V_{\rm xc}^{\rm iq-DFT}}{\partial I}\Big|_{\substack{I=0\\Q=0}} + \frac{TS^2}{\kappa} - \frac{TS_s^2}{\kappa_s} \tag{6.22}$$

for the current derivatives at $I = 0$ of the xc bias in i-DFT and iq-DFT. In the original i-DFT framework, the Seebeck coefficient as well as the thermal conductance are given by their KS counterparts. In iq-DFT, this corresponds to the approximation of setting $\Psi_{\rm xc} \approx 0$ and approximating the xc bias as a functional independent of the heat current, i.e., $V_{\rm xc}[n, I, Q] \approx V_{\rm xc}[n, I]$. In the previous chapter we have extended the original i-DFT formalism to not only give the many-body electrical conductance but also the many-body Seebeck coefficient, while for the thermal conductance one still find discrepancies with the correct many-body quantity. In iq-DFT, this corresponds to the approximation $\Psi_{\rm xc}[n, I, Q] \approx \Psi_{\rm xc}[n, I]$, independent of Q for general $V_{\rm xc}[n, I, Q]$. Then we find $S = S_s - \kappa_s \frac{\partial V_{\rm xc}}{\partial Q}|_{Q=0}^{I=0} = S_s - \frac{\partial V_{\rm xc}}{\partial \Delta T}|_{Q=0}^{I=0} = S_s - S_{\rm xc}$, as in refs. [42, 85]. This approximation then also implies a finite correction (over pure i-DFT) for the electrical conductance $G = G_s[1 - \left(\frac{\partial V_{\rm xc}}{\partial I}|_{\substack{I=0\\Q=0}} + TS_{\rm xc}(S_{\rm xc} - 2S_s)/\kappa_s\right) G_s]^{-1}$.

In order to calculate the interacting transport coefficients from eq. (6.20), one first needs to evaluate the KS coefficients, and consequently, an approximation for the functional $v_{\rm Hxc}[n]$ is required where the dependence of $v_{\rm Hxc}$ on I and Q can be neglected if we work in the linear response regime. In order to gain some first insight into the possible approximations for the iq-DFT functionals, in the following section we will discuss an application of iq-DFT formalism to a particular model system in the linear response regime.

6.3 Application to the single impurity Anderson Model

In this section we apply our iq-DFT framework to the SIAM. Due to its simplicity and evident physical interpretation, this model is ideally suited as a first system

to explore the new formalism and has been used in many previous works [42, 95, 100], both within and outside any DFT setting.

For simplicity, we choose symmetric coupling of the leads, i.e., $\gamma_L = \gamma_R = \gamma/2$. In the present section we are mostly concerned with application of the theory to the linear response regime, but for derivation purposes we keep a finite symmetric thermal gradient and a finite symmetric DC bias between the leads , i.e., $T_\alpha = T(1 + s_\alpha \frac{\Psi}{2})$ and $V_\alpha = s_\alpha \frac{V}{2}$ with $s_{L/R} = \pm 1$ where we choose $\mu = 0$.

6.3.1 Reverse engineering from the Many-Body Model

In order to apply our iq-DFT formalism to the SIAM, we need approximations for all the xc potentials of the formalism. Since here we are concerned with the linear response regime only, we actually need to construct parametrizations for the derivatives of the xc potentials (at zero currents) appearing in eqs. (6.20).

This can be achieved through a reverse engineering process. First, we express the interacting density on and currents through the dot in terms of the many-body spectral function $A(\omega)$ [86, 88]:

$$n = \sum_{\alpha=L,R} \int f\left(\frac{\omega - s_\alpha \frac{V}{2}}{T\left(1 + s_\alpha \frac{\Psi}{2}\right)}\right) A(\omega), \tag{6.23a}$$

$$I = \frac{\gamma}{2} \sum_{\alpha=L,R} \int s_\alpha f\left(\frac{\omega - s_\alpha \frac{V}{2}}{T\left(1 + s_\alpha \frac{\Psi}{2}\right)}\right) A(\omega), \tag{6.23b}$$

$$Q = \frac{\gamma}{2} \sum_{\alpha=L,R} \int s_\alpha f\left(\frac{\omega - s_\alpha \frac{V}{2}}{T\left(1 + s_\alpha \frac{\Psi}{2}\right)}\right) (\omega - \frac{V}{2}) A(\omega). \tag{6.23c}$$

In order to proceed with the reverse engineering, we consider the MBM spectral function of eq. (5.6) which correctly describes the impurity coupled to the leads in range of temperatures larger than any other energy scale of the system. In particular, the MBM correctly captures CB physics, but not the Kondo regime.

For the reverse engineering, we also need the densities and currents expressed through the KS equations. These can be obtained from eqs. (6.23) by replacing the basic potentials by their non-interacting versions, i.e., $v \to v_s$, $V \to V_s$ and $\Psi \to \Psi_s$, and replacing $A(\omega) \to A_s(\omega) = \gamma/((\omega - v_s)^2 + \gamma^2/4)$. The resulting

integrals can be evaluated analytically (see appendix B) and the basic variables of the theory can then be expressed as

$$n = 1 - \frac{1}{\pi}\left(\mathrm{Im}\left[\psi\left(z_s^R\right)\right] + \mathrm{Im}\left[\psi\left(z_s^L\right)\right]\right), \tag{6.24a}$$

$$I = \frac{\gamma}{2\pi}\left(\mathrm{Im}\left[\psi\left(z_s^R\right)\right] - \mathrm{Im}\left[\psi\left(z_s^L\right)\right]\right), \tag{6.24b}$$

$$Q = \frac{\gamma^2}{2\pi}\left(\mathrm{Re}\left[\psi\left(z_s^L\right)\right] - \mathrm{Re}\left[\psi\left(z_s^R\right)\right]\right) + \frac{\gamma^2}{2\pi}\log\left(\frac{1+\Psi_s/2}{1-\Psi_s/2}\right) + \left(v_s - \frac{V_s}{2}\right) I, \tag{6.24c}$$

where $z_s^{L/R} = \frac{1}{2} + \frac{\gamma/2 + \mathrm{i}(v_s \mp V_s/2)}{2\pi T(1 \pm \Psi_s/2)}$ and $\psi(z)$ is the digamma function with general complex argument z [89]. Also for the MBM, all integrals in eqs. (6.23) can be evaluated analytically using the same integrals of the appendix B, which means that we can use the results obtained in eq. (6.24). Making use of eq. (5.6) with eq. (6.23) yields

$$n^{\mathrm{MBM}} = \frac{n(v, V, \Psi)}{1 + \frac{1}{2}\left(n(v, V, \Psi) - n(v+U), V, \Psi\right)} \tag{6.25a}$$

$$I^{\mathrm{MBM}} = I(v, V, \Psi) - \frac{1}{2} n(v, V, \Psi)\left(I(v, V, \Psi) - I(v+U, V, \Psi)\right) \tag{6.25b}$$

$$Q^{\mathrm{MBM}} = Q(v, V, \Psi) - \frac{1}{2} n(v, V, \Psi)\left(Q(v, V, \Psi) - Q(v+U, V, \Psi)\right) \tag{6.25c}$$

where we have made explicit the dependence of the density and the currents of eq. (6.24) with the effective potentials that enter as arguments, replacing the KS potentials (v_s, V_s, Ψ_s).

Taking the derivatives of eqs. (6.24) with respect to the related KS potentials, we can derive in an exact way the matrix elements L_{ij}^s of the matrix $\mathbf{L}_s$ (see eq. (6.13)) as

$$L_{ij}^s(v_s) = M_{ij}(v_s) \tag{6.26}$$

where we have used the M_{ij} coefficients derived in eqs. (B.19) and made explicit the dependence on the KS potential v_s.

Similarly, also for the many-body model we can derive the corresponding matrix elements of the interacting response matrix $\mathbf{L}$ by taking the corresponding derivatives. These matrix elements then read

$$L_{ij}(v) = \left(1 - \frac{n}{2}\right) M_{ij}(v) + \frac{n}{2} M_{ij}(v+U). \tag{6.27}$$

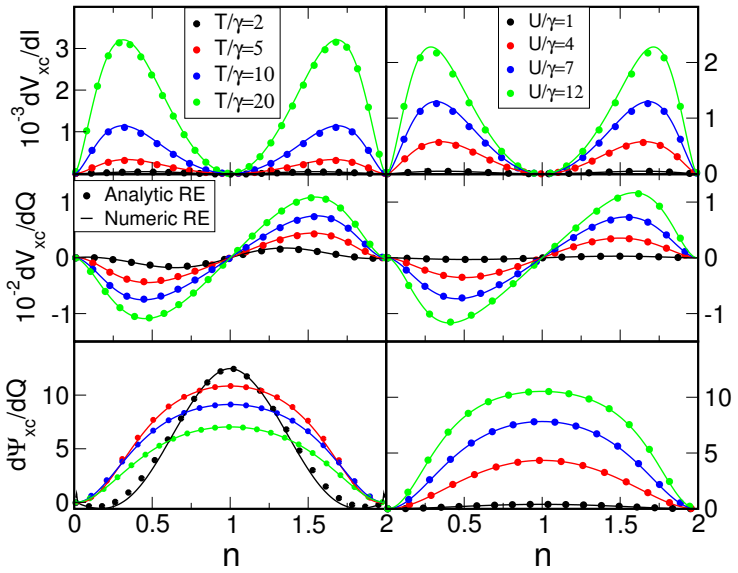

Figure 6.2: Comparison between analytical and numerical reverse engineered xc derivatives as function of the density. The left column corresponds to $U/\gamma = 8$ and the right one to $T/\gamma = 12$. For the analytic result the relation between the gates and the density from the SSM has been used, while for the numeric inversion this relation directly follows eq. (6.24a). The xc derivatives are obtained in both approaches using eqs. (6.27) and (6.28).

Combining eqs. (6.12) and eqs. (6.19) we arrive at

$$\left.\frac{\partial V_{\rm xc}}{\partial I}\right|_{\substack{I=0\\Q=0}} = \frac{1}{L^s_{11}(v_s)} - \frac{1}{L_{11}(v)} + \frac{L^s_{12}(v_s)^2}{L^s_{11}(v_s)}\frac{1}{\det(\mathbf{L_s}(v_s))} - \frac{L_{12}(v)^2}{L_{11}(v)}\frac{1}{\det(\mathbf{L}(v))}, \tag{6.28a}$$

$$\left.\frac{\partial \Psi_{\rm xc}}{\partial I}\right|_{\substack{I=0\\Q=0}} = \left.\frac{\partial V_{\rm xc}}{\partial Q}\right|_{\substack{I=0\\Q=0}} = \frac{L^s_{12}(v_s)}{\det(\mathbf{L_s}(v_s))} - \frac{L_{12}(v)}{\det(\mathbf{L}(v))}, \tag{6.28b}$$

$$\left.\frac{\partial \Psi_{\rm xc}}{\partial Q}\right|_{\substack{I=0\\Q=0}} = \frac{L^s_{11}(v_s)}{\det(\mathbf{L_s}(v_s))} - \frac{L_{11}(v)}{\det(\mathbf{L}(v))}. \tag{6.28c}$$

Eqs. (6.28) together with eqs. (6.27) provide the analytical parametrizations of the xc derivatives in terms of both v_s and v. Instead, the dependence of the xc derivatives on the density can be obtained by (i) replacing v in the argument of the many-body coefficients L_{ij} by $v(n)$, the inverse of the density-potential relationship of eq. (6.23) (at $V = 0$ and $\Psi = 0$) and, similarly, (ii) by using $v_s(n)$ as arguments in the KS coefficients L^s_{ij} which can be obtained by inverting the corresponding KS expression $n(v_s)$ for the density (at $V_s = 0$ and $\Psi_s = 0$). These inverse functions can easily be obtained numerically and, by construction, the

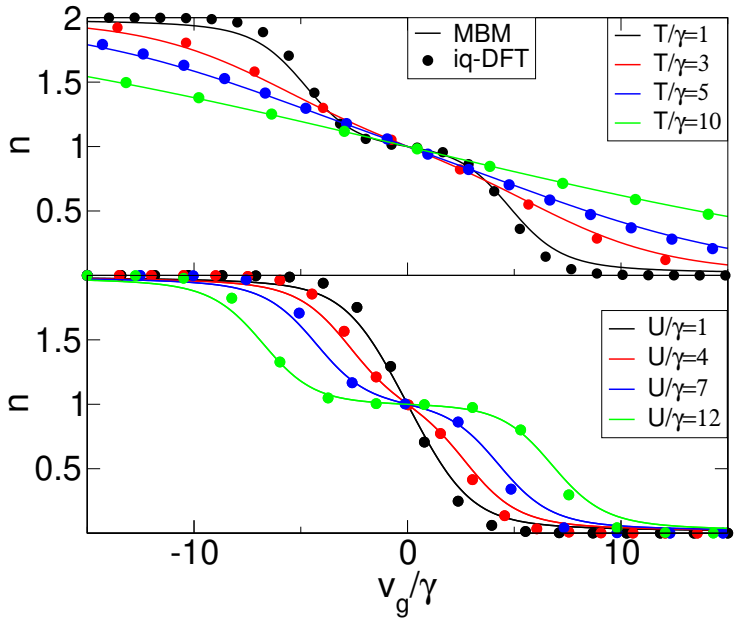

Figure 6.3: Equilibrium density of the SIAM as a function of the gate voltage ($v_g = v + \frac{U}{2}$) from the MBM and iq-DFT. In iq-DFT, the Hxc potential of the single site model has been used (see main text). Upper panel: density for different temperatures at fixed $U/\gamma = 8$, lower panel: density for different interactions at fixed $T/\gamma = 1$.

resulting density functionals for the xc derivatives then give exactly the same linear response transport coefficients (in a DFT framework) as the many-body model. Nevertheless, here we are interested in finding an analytical parametrization for the xc derivatives in terms of the density and therefore an approximation for the density-gate relationship is required. The completion of our analytical approach requires the insertion of parametrizations of both $v(n)$ and $v_s(n)$) from SSM into eqs. (6.28). We choose the exact SSM potentials eqs. (A.1) and (A.2).

The xc derivatives provide a measure of the correction required over the KS system to accurately describe the linear response properties of the many-body model. From fig. 6.2 it is evident that the xc corrections become larger with increasing temperature T or interaction strength U. In the left column of fig. 6.2, the xc derivatives are calculated at $U/\gamma = 8$ for different temperatures T while in the right column T is fixed to $T/\gamma = 12$ and the xc derivatives are obtained for different interactions U. Our analytical parametrization is compared with the numerically exact inversion from the MBM approach.

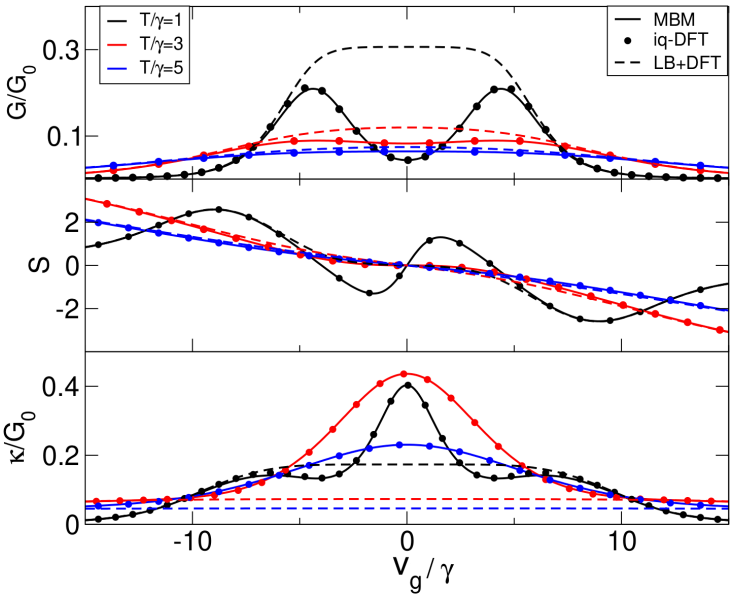

Figure 6.4: Transport coefficients and electronic contribution to the figure of merit as a function of the gate voltage ($v_g = v + \frac{U}{2}$) for $U/\gamma = 8$. The iq-DFT results using the analytic reverse engineered xc derivatives eqs. (6.28) are compared with those obtained directly from eqs. (6.23) when using the model spectral function of eq. (5.6).

6.3.2 Numerical results

In order to assess the accuracy of our analytically RE approximations for the derivatives of the iq-DFT xc potentials in comparison to the reference MBM, we solve the DFT problem in the standard way where we use the v_{Hxc} of the SSM (eq. (A.3)). In fig. 6.3, the iq-DFT densities as function of the gate voltage ($v_g = v + \frac{U}{2}$) are compared with the ones obtained from MBM. As expected, this approximate Hxc potential works better as T/γ is increased (for fixed U/γ) while for relatively small $T/\gamma = 1$ the qualitative behaviour of the density is captured well for different interactions while quantitative differences persist.

In fig. 6.4, we show the linear transport coefficients for a fixed interaction strength $U/\gamma = 8$ and various temperatures as function of the gate voltage v_g for the MBM, iq-DFT, and the LB+DFT approach (corresponding to the KS transport coefficients). The iq-DFT results agree extremely well with the MBM ones highlighting the good approximation of the gate-density relations (eqs. (A.3)) in the range $T/\gamma > 1$. On the other hand, the LB+DFT results are only accurate in the empty/full orbital regime ($|v_g|/\gamma \geq 7$) where correlations play essentially no

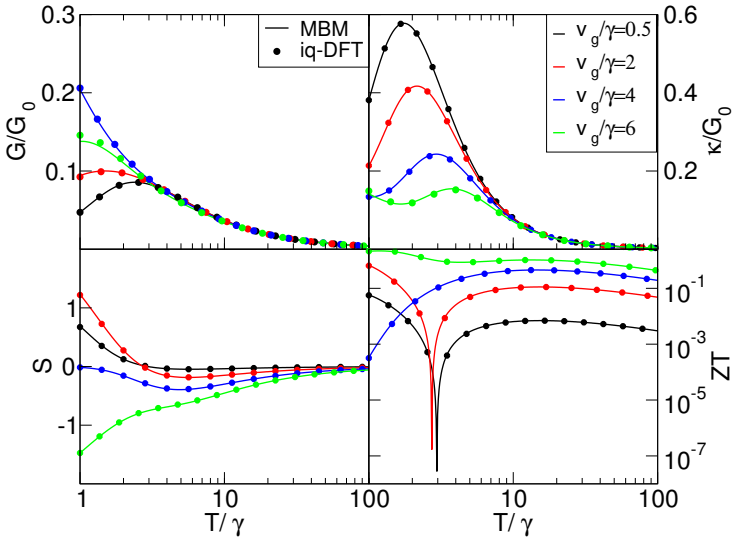

Figure 6.5: Transport coefficients and electronic contribution to the figure of merit as a function of the temperature for $U/\gamma = 8$. The iq-DFT results using the analytic reverse engineered xc derivatives eqs. (6.28) are compared with those obtained directly from eqs. (6.23) when using the model spectral function of eq. (5.6).

role. Notice that, for $T/\gamma = 1$, in the LB+DFT the Seebeck coefficient flattens around $v_g/\gamma = 0$, while both iq-DFT and MBM predict a significant deviation [42, 85]. Note that the electrical and heat conductances are shown in units of the quantum of conductance G_0, while the Seebeck coefficient is given in atomic units.

In fig. 6.5, the iq-DFT transport coefficients as well as the figure of merit of the system $ZT = TGS^2/\kappa$ are compared with those obtained from MBM for fixed gate potential as function of temperature for strong correlations $U/\gamma = 8$. As in fig. 6.5 we observe excellent agreement as T/γ increases. Finally in fig. 6.6, we show the iq-DFT transport coefficients for different interaction strength U using xc parametrizations (eq. (6.28)). Again we observe that for the given, fixed temperature $T/\gamma = 1$, the whole range from weak ($U/\gamma = 1$) to strong correlations ($U/\gamma > 7$) is correctly captured in iq-DFT as compared to the MBM.

As summary of our numerical results, we have shown that our parametrization for the derivatives of the iq-DFT xc potentials leads to rather accurate reproduction of the linear response transport coefficients of the MBM. There were two approximations involved in our iq-DFT approach: (i) we used the approximate Hxc potential of eq. (A.3) for the self-consistent calculation of the density and (ii) the

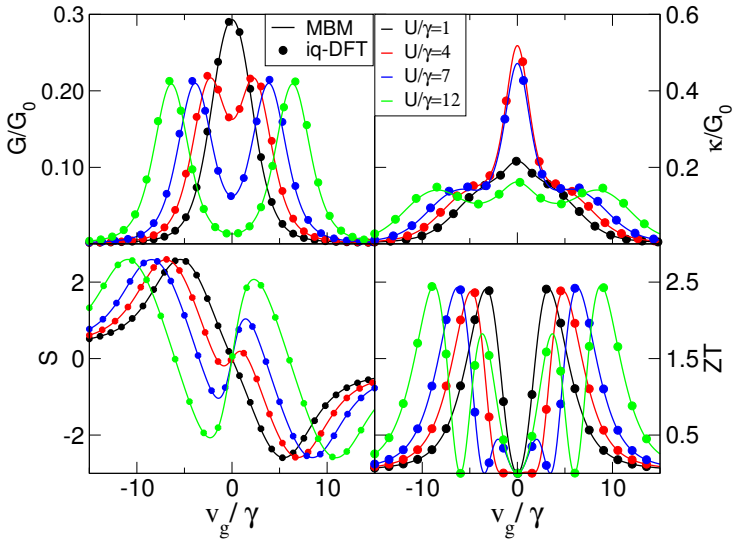

Figure 6.6: Transport coefficients and electronic contribution to the figure of merit as function of the gate voltage ($v_g = v + \frac{U}{2}$) for $T/\gamma = 1$. The iq-DFT results using the analytic reverse engineered xc derivatives are compared with those obtained directly from eqs. (6.23) when using the model spectral function of eq. (5.6).

approximate density-potential relations from the SSM eqs. (A.1) and (A.2) were used to construct the xc derivatives as functionals of the equilibrium density. Both approximations (i) and (ii) originate from the SSM and therefore it is not surprising that the corresponding iq-DFT calculations show improved agreement with the MBM as temperature increases. We would also like to emphasize again that the MBM approximation for the spectral function eq. (5.6) is by construction derived for the CB regime ($T/T_K \gg 1$ where T_K is the Kondo temperature of the system). Therefore our approximation cannot and should not be expected to accurately describe the linear transport coefficients of the interacting system for temperatures in the Kondo regime ($T \ll T_K$). Nevertheless, our approximation may very well serve as a first step towards the construction of improved approximations which are valid in this regime as well. While such a construction is beyond the scope of the present study, we have already observed that the low temperature behaviour of the Seebeck coefficient and the thermal conductance are qualitatively correctly captured with the analytical approach. Therefore the main corrections appear to be necessary for the electrical conductance, where ideas of the corresponding i-DFT shown in the previous chapter are expected to be transferable to iq-DFT as well.

This chapter is based on the article [95].

7

Non-Equilibrium Spectral functions with Multi-Terminal Steady-State Density Functional Theory

Contents

7.1 Non-Equilibrium Spectral functions from multi-terminal i-DFT 96
7.2 i-DFT potentials for the Anderson model 100
7.2.1 Results 103

In this chapter we generalize i-DFT to the multi-terminal configuration and then consider the specific situation of a junction connected to three electrodes. We show how in the "ideal STM setup", where one of the electrodes is weakly coupled to the system, one can extract the *non-equilibrium* many-body spectral function of the junction at arbitrary temperature and bias between the other two electrodes within the i-DFT framework [95]. We apply the approach to the SIAM for which we construct an approximate xc functional which partially captures the splitting of the Kondo peak at finite bias. We also identify the crucial feature of the xc functional needed to fully describe the splitting of the Kondo peak.

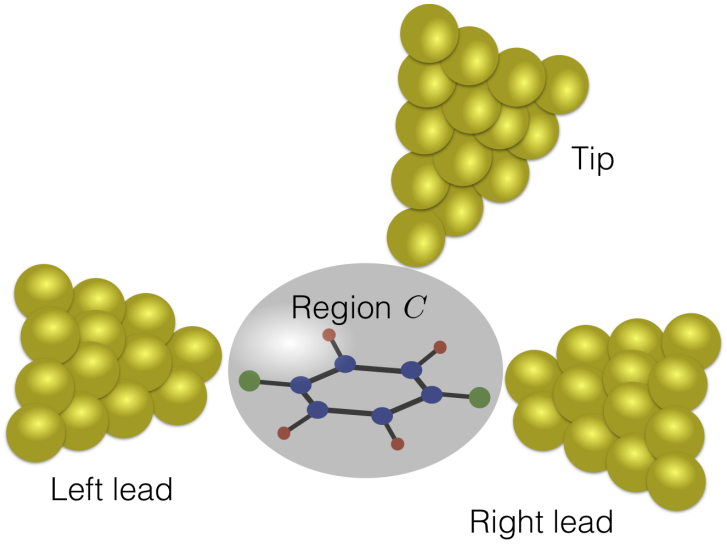

Figure 7.1: Schematic drawing of a three-terminal nanoscale junction. A molecular region of space C is coupled to a left (L) and right (R) leads at voltages $V_L = -V_R = V/2$ with temperature T and to a tip (τ) at voltage V_τ with zero temperature $T_\tau = 0$.

7.1 Non-Equilibrium Spectral functions from multi-terminal i-DFT

We consider a nanoscopic region C containing a quantum dot or molecule and a number of electrodes $\alpha = 1, .., \mathcal{N}$, as depicted schematically in fig. 7.1 for $\mathcal{N} = 3$. The system is assumed to be in a steady-state characterized by temperatures T_α and external voltages V_α in electrode α and by a gate voltage $v(\mathbf{r})$ in C. As long as region C is finite there are no constraints on the shape of its boundaries. Due to gauge invariance the same steady-state is attained by shifting all voltages by a constant energy P, i.e., $V_\alpha \to V_\alpha + P$ and $v(\mathbf{r}) \to v(\mathbf{r}) + P$. Let I_α be the longitudinal current flowing out of electrode α and $n(\mathbf{r})$ be the density in the nanoscopic region. Due to charge conservation (consequence of the aforementioned gauge invariance) the currents fulfill $\sum_\alpha I_\alpha = 0$. This situation resembles the aforementioned multi-terminal iq-DFT framework (see section 6.1) with the exception that the aim in the present chapter is restricted to the correct description of the density in the central region C and the electrical currents. Following the same ideas as in section 6.1 we can write the linear response relationship between the current

vector $\mathbf{I}$ and the potential vector $\mathbf{\Phi}$ as

$$\mathbf{I} = \begin{pmatrix} I_1 \\ \vdots \\ I_{\mathcal{N}-1} \end{pmatrix} = \left. \begin{pmatrix} \frac{\delta I_1}{\delta V_1} & \cdots & \frac{\delta I_1}{\delta V_{\mathcal{N}-1}} \\ \vdots & \ddots & \vdots \\ \frac{\delta I_{\mathcal{N}-1}}{\delta V_1} & \cdots & \frac{\delta I_{\mathcal{N}-1}}{\delta V_{\mathcal{N}-1}} \end{pmatrix} \right|_{V_\alpha=0} \begin{pmatrix} V_1 \\ \vdots \\ V_{\mathcal{N}-1} \end{pmatrix} = \mathbf{L}\mathbf{\Phi}. \tag{7.1}$$

By construction, the rate of production of entropy in the theory corresponds to $\dot{\mathcal{S}} = \frac{1}{T}\sum_{\alpha=1}^{\mathcal{N}-1} I_\alpha V_\alpha = \mathbf{\Phi}^\intercal \mathbf{L}\mathbf{\Phi}$. Since the rate of production of entropy has to be larger than zero in any out of equilibrium situation, we can conclude that $\mathbf{L}$ is positive definite and therefore there exists a one to one map between the set of "densities" $(n, I_1, \ldots, I_{\mathcal{N}-1})$ and the set of "potentials" $(v, V_1, \ldots, V_{\mathcal{N}-1})$ in a finite (and gate dependent) region of voltages V_α around zero voltage around any common temperature T.

Assuming that the interacting density and currents are non-interacting representable, the multi-terminal i-DFT map (for non-interacting systems) tells us that there exists a unique set of Kohn-Sham (KS) potentials $(v_s, \mathbf{\Phi}_s)$ which in the non-interacting system reproduce the density $n(\mathbf{r})$ and currents $\mathbf{I}$ of the interacting one. Following the KS procedure, we define the exchange-correlation (xc) voltages $V_{\alpha,\mathrm{xc}}[n,\mathbf{I}] = V_{\alpha,s}[n,\mathbf{I}] - V_\alpha[n,\mathbf{I}]$ and the Hartree-xc (Hxc) gate voltage $v_{\mathrm{Hxc}}[n,\mathbf{I}] = v_s[n,\mathbf{I}] - v[n,\mathbf{I}]$ (which are functionals of the density in C and the currents) and then calculate the interacting density and currents by solving self-consistently the equations (henceforth $\int \equiv \int \frac{d\omega}{2\pi}$)

$$n(\mathbf{r}) = 2\sum_\alpha \int f_\alpha(\omega - V_\alpha - V_{\alpha,\mathrm{xc}}[n,\mathbf{I}])\, A_{\alpha,s}(\omega,\mathbf{r}), \tag{7.2}$$

$$I_\alpha = 2\sum_{\alpha'} \int \left[f_\alpha(\omega - V_\alpha - V_{\alpha,\mathrm{xc}}[n,\mathbf{I}]) - f_{\alpha'}(\omega - V_{\alpha'} - V_{\alpha',\mathrm{xc}}[n,\mathbf{I}]) \right] \mathcal{T}_{\alpha\alpha',s}(\omega), \tag{7.3}$$

where $f_\alpha(\omega) = 1/(e^{\omega/T_\alpha}+1)$ is the Fermi function of lead α at temperature T_α. In the KS equations $A_{\alpha,s}(\omega,\mathbf{r}) = \langle \mathbf{r}|\mathbf{G}_s^{\mathrm{R}}(\omega)\Gamma_\alpha(\omega)\mathbf{G}_s^{\mathrm{A}}(\omega)|\mathbf{r}\rangle$ is the partial KS spectral function written in terms of the retarded/advanced KS Green's functions $\mathbf{G}_s^{\mathrm{R/A}}$ and hybridization $\mathbf{G}_\alpha(\omega)$ due to lead α, whereas $\mathcal{T}_{\alpha\alpha',s}(\omega) = \mathrm{Tr}\left[\mathbf{G}_s^{\mathrm{R}}(\omega)\Gamma_\alpha(\omega)\mathbf{G}_s^{\mathrm{A}}(\omega)\Gamma_{\alpha'}(\omega)\right]$ are the KS transmission probabilities.

Here, we first recall how to calculate out-of-equilibrium spectral functions from transport measurements [101–107], and then we proceed to calculate the corresponding quantity taking advantage of the multi-terminal i-DFT framework.

We consider a three-terminal molecular junction as illustrated in fig. 7.1. Two electrodes, the left ($\alpha = L$) and right ($\alpha = R$) ones, have voltages $V_L = -V_R = V/2$ (gauge fixing) and we choose the same finite temperature $T_L = T_R = T$. The third electrode plays the role of a tip ($\alpha = \tau$) and is kept at zero temperature and voltage V_τ. The contact between the tip and the nanoscopic region is described by the energy-independent hybridization Γ_τ whose indices run over a suitable one-electron orbital basis for the considered molecule. The Γ_τ matrix, aside from being constrained to be symmetric and positive semi-definite, will be varied at will.

According to Meir and Wingreen [86] the current I_τ flowing out of the tip is given by

$$I_\tau = 2 \int \mathrm{Tr}\left[f_\tau(\omega - V_\tau)\Gamma_\tau A(\omega) + i\Gamma_\tau G^<(\omega)\right] \tag{7.4}$$

where $A(\omega) = i\left[G^>(\omega) - G^<(\omega)\right]$ is the non-equilibrium, finite-temperature many-body spectral function expressed in terms of the lesser/greater Green's functions whereas $f_\tau(\omega) = \theta(-\omega)$ is the zero-temperature Fermi function of the tip. In eq. (7.4) the trace is over the indices of the molecular one-electron basis. In the ideal Scanning Tunneling Microscopy (STM) limit, $\Gamma_\tau \to 0$, the Green's functions $G^\lessgtr$ are not affected by a change of the tip voltage and hence [108]

$$\lim_{\Gamma_\tau \to 0} \frac{\partial G^\lessgtr(\omega)}{\partial V_\tau} = 0. \tag{7.5}$$

We then consider a hybridization of the form

$$\Gamma_\tau = \gamma_\tau \Big[\eta_p |p\rangle\langle p| + \eta_q |q\rangle\langle q| + \eta_{pq}\big(|p\rangle\langle q| + |q\rangle\langle p|\big)\Big]. \tag{7.6}$$

Here $|p\rangle$ and $|q\rangle$ are elements of an arbitrary single-particle basis and γ_τ, η_p, η_q, and η_{pq} are frequency-independent constants, i.e., we take the tip to be a featureless

lead in the wide-band limit. The operator (7.6) is symmetric and positive semi-definite for all $\gamma_\tau, \eta_p, \eta_q \geq 0$ and $|\eta_{pq}| \leq \sqrt{\eta_p \eta_q}$. Taking into account eq. (7.5) it is straightforward to show that

$$\lim_{\gamma_\tau \to 0} \frac{1}{\gamma_\tau} \frac{\partial I_\tau}{\partial V_\tau} = \frac{\mathcal{A}(V_\tau)}{\pi} \tag{7.7}$$

where

$$\mathcal{A}(\omega) = \eta_p A_{pp}(\omega) + \eta_q A_{qq}(\omega) + \eta_{pq}\Big[A_{pq}(\omega) + A_{qp}(\omega)\Big] \tag{7.8}$$

is a linear combination of the matrix elements of the spectral function, i.e. $A_{pq}(\omega) = \langle p|A(\omega)|q\rangle$. Choosing, e.g., $\eta_p = 1$ and $\eta_q = 0$ we can obtain all diagonal elements $A_{pp} = \mathcal{A}$ by varying p. Subsequently we can extract the off-diagonal elements $A_{pq} + A_{qp} = \mathcal{A} - A_{pp} - A_{qq}$ by setting $\eta_{pq} = \eta_p = \eta_q = 1$.

From the i-DFT perspective we fix the gauge according to $V_{\mathrm{L},s} = -V_{\mathrm{R},s} = V_s/2$ and consider the combination $I = (I_L - I_R)/2$ and I_τ as the two independent currents. Then the triple $v_{\mathrm{Hxc}} = v_{\mathrm{Hxc}}[n, I_\tau, I]$, $V_{\tau,\mathrm{xc}} = V_{\tau,\mathrm{xc}}[n, I_\tau, I]$ and $V_{\mathrm{xc}} = V_{\mathrm{xc}}[n, I_\tau, I]$ are functionals of the triple n, I_τ and I (here $V_{\mathrm{xc}}[n, I_\tau, I] = V_s[n, I_\tau, I] - V[n, I_\tau, I]$). Considering n, I_τ and I as interacting functionals of the physical voltages v, V_τ and V, eq. (7.5) implies that $\partial n(\mathbf{r})/\partial V_\tau \to 0$ and $\partial I/\partial V_\tau \to 0$ for $\Gamma_\tau \to 0$, therefore by the chain rule it thus follows that

$$\lim_{\Gamma_\tau \to 0} \frac{\partial v_{\mathrm{Hxc}}}{\partial V_\tau} = \lim_{\Gamma_\tau \to 0} \frac{\partial V_{\mathrm{xc}}}{\partial V_\tau} = 0. \tag{7.9}$$

Following the same ideas described in ref. [108] for the equilibrium spectral function, we now take advantage of these relations in order to express the (non-equilibrium) spectral function A in terms of the (non-equilibrium) KS spectral function A_s. In the non-interacting KS system the tip current is given by eq. (7.4), replacing $A(\omega)$ with the KS spectral function $A_s = \sum_\alpha A_{\alpha,s}$, $G^<(\omega)$ by the KS lesser GF $G_s^<$ and V_τ by $V_{\tau,s} = V_\tau + V_{\tau,xc}$. Taking into account eq. (7.9) and the fact that Γ_τ is energy-independent, we find

$$\lim_{\gamma_\tau \to 0} \frac{1}{\gamma_\tau} \frac{\partial I_\tau}{\partial V_\tau} = \frac{\mathcal{A}_s(V_\tau + V_{\tau,\mathrm{xc}})}{\pi} \left(1 + \frac{\partial V_{\tau,\mathrm{xc}}}{\partial I_\tau} \frac{\partial I_\tau}{\partial V_\tau}\right) \tag{7.10}$$

where $\mathcal{A}_s$ is defined as in eq. (7.8) with $A \to A_s$. Combining this result with eq. (7.7), we arrive at the first main result of this chapter

$$\mathcal{A}(\omega) = \lim_{\gamma_\tau \to 0} \frac{\mathcal{A}_s(\omega + V_{\tau,\mathrm{xc}}(\omega))}{1 - \frac{\gamma_\tau}{\pi} \frac{\partial V_{\tau,\mathrm{xc}}(\omega)}{\partial I_\tau} \mathcal{A}_s(\omega + V_{\tau,\mathrm{xc}}(\omega))}, \tag{7.11}$$

which generalizes the corresponding result of ref. [108] to non-equilibrium spectral functions. Here we have made explicit the dependence of $V_{\tau,\mathrm{xc}}$ on $\omega = V_\tau$ through its dependence on I_τ. Choosing, e.g., $\eta_p = 1$ and $\eta_q = 0$, eq. (7.11) provides a relation between A_{pp} and $A_{s,pp}$. The off-diagonal combination $A_{pq} + A_{qp}$ does instead follow by setting $\eta_{pq} = \eta_p = \eta_q = 1$. We also observe that both $\mathcal{A}_s$ and $\mathcal{A}$ are normalized to the same value, i.e. $\int \mathcal{A}(\omega) = \int \mathcal{A}_s(\omega)$ as it should be[1].

7.2 i-DFT potentials for the Anderson model

We apply the i-DFT framework to the three-terminal single-impurity Anderson model (SIAM) with charging energy U. Since the SIAM nanoscopic region has only one electronic degree of freedom, the density $n = N$ coincides with the impurity occupation N, and all hybridization matrices are scalar. We then write $\Gamma_\tau = \gamma_\tau$ for the tip and consider energy-independent left/right hybridizations $\gamma_{L/R}$. The i-DFT self-consistent equations for n, I_τ and I read

$$n = 2 \int \sum_{\alpha=L,R,\tau} \tilde{f}_\alpha(\omega) \frac{\gamma_\alpha}{\gamma} A_s(\omega) \tag{7.12}$$

$$I_\tau = 2\gamma_\tau \int \left[\frac{\gamma_L + \gamma_R}{\gamma} \tilde{f}_\tau(\omega) - \sum_{\alpha=L,R} \frac{\gamma_\alpha}{\gamma} \tilde{f}_\alpha(\omega) \right] A_s(\omega) \tag{7.13}$$

$$I = \int \left[\gamma_L \frac{2\gamma_R + \gamma_\tau}{\gamma} \tilde{f}_L(\omega) - \gamma_R \frac{2\gamma_L + \gamma_\tau}{\gamma} \tilde{f}_R(\omega) - \frac{\gamma_\tau(\gamma_L - \gamma_R)}{\gamma} \tilde{f}_\tau(\omega) \right] A_s(\omega) \tag{7.14}$$

where we have defined $\tilde{f}_\alpha(\omega) \equiv f_\alpha(\omega - V_\alpha - V_{\alpha,\mathrm{xc}})$ as the shifted Fermi function and $\gamma \equiv \gamma_L + \gamma_R + \gamma_\tau$. The KS spectral function is simply $A_s(\omega) = \ell_\gamma(\omega - v - v_{\mathrm{Hxc}})$ with the Lorentzian $\ell_\gamma(\omega) = \gamma/(\omega^2 + \gamma^2/4)$.

[1] This follows by integrating over ω both sides of eq. (7.11), changing variable $\omega' = \omega + V_{\tau,\mathrm{xc}}(\omega)$ in the r.h.s. and taking into account the Jacobian $\frac{\mathrm{d}\omega'}{\mathrm{d}\omega} = 1/(1 - \frac{\gamma_\tau}{\pi} \frac{\partial V_{\tau,xc}(\omega)}{\partial I_T} \mathcal{A}_s(\omega + V_{\tau,xc}(\omega)))$.

Here we note that one can also express n, I, and I_τ in terms of the many-body spectral function $A(\omega)$. The resulting equations have the same structure as eqs. (7.12)-(7.14) with $A_s(\omega)$ replaced by $A(\omega)$, and the Fermi functions evaluated at the external biases, i.e., without the xc contributions. Since both KS and many-body spectral functions are normalized, the range of possible densities and currents is the same in the interacting and non-interacting case and any set of many-body "densities" (n, I, I_τ) is non-interacting representable.

In order to derive an approximation for the i-DFT potentials we observe that in the interacting system the current flowing out of lead α reads $I_\alpha = 2\int [f_\alpha(\omega - V_\alpha)\gamma_\alpha A(\omega) + i\gamma_\alpha G^<(\omega)]$. Taking into account that the impurity occupation is $n = -2i\int G^<(\omega)$ we get

$$n + \frac{I_\alpha}{\gamma_\alpha} = 2\int f_\alpha(\omega - V_\alpha)A(\omega). \tag{7.15}$$

Inserting the MBM interacting spectral function of eq. (5.6) valid in the CB regime into the r.h.s. of eq. (7.15) we get the same expression obtained in ref. [41] for the two-terminal setup. Following the same analysis of the step features of the numerical RE (H)xc potentials as in appendix A.2 (see fig. A.2), we can parametrize our CB functionals in the same manner

$$v^{\rm CB}_{\rm Hxc} - V^{\rm CB}_{\alpha,\rm xc} \approx \frac{U}{2} + \frac{U}{\pi}\mathrm{atan}\left[\frac{N + I_\alpha/(2\gamma_\alpha) - 1}{\nu W(T_\alpha)}\right] \tag{7.16}$$

with $\nu = 1$, $W(T) = 0.16 \times (\gamma/U)(1 + 9(T/\gamma)^2)$ and $I_L = I - I_\tau/2$, $I_R = -I - I_\tau/2$ (as follows from charge conservation). From eqs. (7.16) we can easily extract an explicit form of the (H)xc potentials $v^{\rm CB}_{\rm Hxc}$, $V^{\rm CB}_{\tau,\rm xc}$ and $V^{\rm CB}_{\rm xc} = 2V^{\rm CB}_{L,\rm xc} = -2V^{\rm CB}_{R,\rm xc}$ in terms of n, I_τ and I

$$v^{\rm CB}_{\rm Hxc} = \frac{U}{2} + \frac{U}{2\pi}\mathrm{atan}\left[\frac{N + I_L/(2\gamma_L) - 1}{\nu W(T_L)}\right] + \frac{U}{2\pi}\mathrm{atan}\left[\frac{N + I_R/(2\gamma_R) - 1}{\nu W(T_R)}\right] \tag{7.17a}$$

$$V^{\rm CB}_{\rm xc} = -\frac{U}{\pi}\mathrm{atan}\left[\frac{N + I_L/(2\gamma_L) - 1}{\nu W(T_L)}\right] + \frac{U}{\pi}\mathrm{atan}\left[\frac{N + I_R/(2\gamma_R) - 1}{\nu W(T_R)}\right] \tag{7.17b}$$

$$v^{\rm CB}_{\tau,\rm xc} = \frac{U}{2\pi}\text{atan}\left[\frac{N + I_L/(2\gamma_L) - 1}{\nu W(T_L)}\right] + \frac{U}{2\pi}\text{atan}\left[\frac{N + I_R/(2\gamma_R) - 1}{\nu W(T_R)}\right] - \frac{U}{\pi}\text{atan}\left[\frac{N + I_\tau/(2\gamma_\tau) - 1}{\nu W(T_\tau)}\right]. \quad (7.17c)$$

The (H)xc potentials in eq. (7.17) are certainly inadequate for temperatures $T \lesssim T_K$. In particular for $T = 0$ the Friedel sum rule implies that the zero-bias interacting and KS conductances $\mathcal{G}_{\alpha\beta} = \partial I_\alpha/\partial V_\beta$ and $\mathcal{G}_{s,\alpha\beta} = \partial I_\alpha/\partial V_{s,\beta}$ are identical [2]. Since (repeated indices are summed over)

$$\mathcal{G}_{\alpha\beta} = \frac{\partial I_\alpha}{\partial V_{s,\mu}}\frac{\partial V_{s,\mu}}{\partial V_\beta} = \mathcal{G}_{s,\alpha\mu}\left(\delta_{\mu\beta} + \frac{\partial V_{\mu,\rm xc}}{\partial I_\nu}\mathcal{G}_{\nu\beta}\right) \quad (7.18)$$

the zero-temperature xc voltages must fulfill $\partial V_{\mu,\rm xc}/\partial I_\nu = 0$ at zero currents. We incorporate this property in $v_{\rm Hxc}$ and $V_{\rm xc}$ using the parametrization of eq. (A.6) for the two-terminal case, i.e., for $\gamma_\tau = 0$, which has been shown to be accurate in a wide range of temperatures and charging energy. For $V_{\tau,\rm xc}$ we propose

$$V_{\tau,\rm xc}(n, I_\tau, I) = \Big[1 - b(n)a_\tau(I_\tau)a(I)\Big]V^{\rm CB}_{\tau,\rm xc}(n, I_\tau, I) \quad (7.19)$$

where in $V^{\rm CB}_{\tau,\rm xc}$ we now take $\nu = 2$ [45] and the functions a_τ and a are similar to the one used in ref. [108] and read

$$a_\tau(I_\tau) = 1 - \frac{2}{\pi}\text{atan}\left[\lambda\left(\frac{I_\tau}{W(0)\gamma_{\tau,\rm eff}}\right)^2\right] \quad (7.20)$$

$$a(I) = 1 - \frac{2}{\pi}\text{atan}\left[\lambda\left(\frac{I}{W(T)\gamma_{\rm eff}}\right)^2\right] \quad (7.21)$$

with $\gamma_{\tau,\rm eff} = \frac{4\gamma_\tau(\gamma_L+\gamma_R)}{\gamma}$, $\gamma_{\rm eff} = \frac{4\gamma_L\gamma_R}{\gamma_L+\gamma_R}$ and $\lambda = 0.16$. For $b(N)$ we implement the same function as in eq. (A.8) but we replace the *two-terminal* conductance $\mathcal{G}_{\rm univ} = dI/dV$ at the ph symmetric gate $v = -U/2$, voltage $V = 0$ and symmetric coupling $\gamma_L = \gamma_R$ (this is a universal function depending only on the ratio T/T_K)

[2] Using the Friedel sum-rule one can show that $\mathcal{G}_{\alpha\beta} = C_{\alpha\beta}(\gamma_\tau, \gamma_L, \gamma_R)A(\mu)$ where the prefactor $C_{\alpha\beta}$ depends only on the hybridizations and $A(\mu)$ is the interacting spectral function at chemical potential μ (which is set to zero in our case). Since $A(\mu) = \frac{4}{\gamma}\sin^2(\pi N/2)$ and since in i-DFT the KS occupation N is the same as the interacting N we conclude that the interacting and KS conductances are the same.

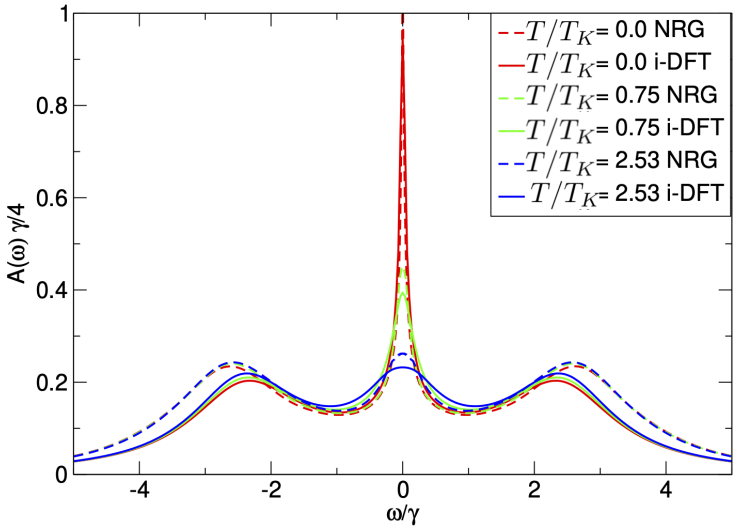

Figure 7.2: Equilibrium i-DFT spectral functions $A(\omega)$ of the SIAM at ph symmetry for $U/\gamma = 5$ for various temperatures compared with NRG results [109, 110]. The Kondo temperature is $T_K/\gamma \approx 0.066$.

with the three-terminal conductance $\mathcal{G}_\tau = dI_\tau/dV_\tau$ at the ph symmetric gate and voltages $V = V_\tau = 0$:

$$b(N=1) = 1 + \frac{1}{\left.\frac{\partial V^{\mathrm{CB}}_{\tau,\mathrm{xc}}}{\partial I_\tau}\right|_{\substack{N=1 \\ I=I_\tau=0}}} \left(\frac{1}{\mathcal{G}_\tau} - \frac{1}{\mathcal{G}_{s,\tau}}\right). \tag{7.22}$$

One can show that $\mathcal{G}_\tau = \frac{4\gamma_\tau(\gamma_L+\gamma_R)}{\gamma^2}\mathcal{G}_{\mathrm{univ}}$. In eq. (7.22) $\mathcal{G}_{s,\tau} = dI_\tau/dV_{s,\tau}$ is the KS conductance at the same external potentials, i.e., ph gate and zero voltages.

7.2.1 Results

As a first test we use our three-terminal i-DFT setup to compute the spectral function of the SIAM in thermal equilibrium for which we can compare with results from NRG techniques [109, 110], see fig. 7.2. The i-DFT spectra agree reasonably well with the NRG ones although the height of the Kondo peak is slightly overestimated and for $T/T_K \gtrsim 2.5$ the Coulomb blockade side peaks are a bit too narrow. In general, the finite temperature i-DFT spectra are of comparable quality as the zero-temperature ones [108].

We now consider the zero-temperature, non-equilibrium SIAM and benchmark the i-DFT spectra against recent results from the Quantum Monte Carlo (QMC)

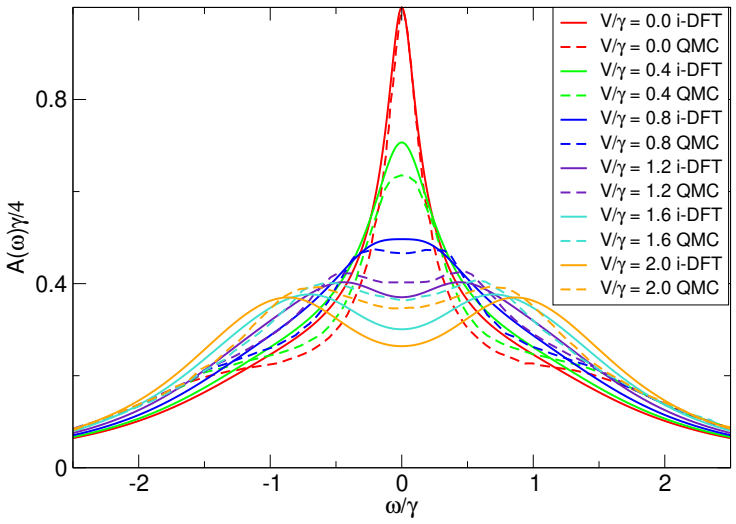

Figure 7.3: Comparison of i-DFT and QMC non-equilibrium spectral functions from ref. [111] at particle-hole symmetry for $U/\gamma = 2.5$ and zero temperature. The Kondo temperature is $T_K/\gamma \approx 0.39$.

approach [111], see fig. 7.3. i-DFT reproduces all main qualitative features of the QMC spectra. In particular, our simple functional of eq. (7.19) for the xc tip bias is able to capture the finite-bias splitting of the Kondo peak in this moderately correlated case $U/\gamma = 2.5$. Nevertheless, in i-DFT the splitting appears at somewhat higher biases and the distance between the peaks increases with bias faster than in QMC. We have done calculations for the same set of biases but at a finite temperature $T/T_K = 0.6$ and observed no dramatic changes except for the suppression of the Kondo peak already at zero voltage.

In fig. 7.4 (left panel) we compare i-DFT with QMC non-equilibrium spectral functions [111] for a stronger interaction strength $U/\gamma = 4$. Clearly our approximation to $V_{\tau,xc}$ is missing a crucial feature since the Kondo splitting is totally absent in i-DFT. Below we highlight an exact property that $V_{\tau,xc}$ must fulfill in order to capture the finite-bias splitting. The interacting spectral function in eq. (7.11) can also be written as

$$A(\omega) = \frac{\mathrm{d}}{\mathrm{d}\omega} \int^{\omega + V_{\tau,xc}(\omega)} \mathrm{d}\omega' A_s(\omega'). \tag{7.23}$$

Therefore, given a many-body (e.g., QMC) spectral function $A(\omega)$, by integration of eq. (7.23) one can reverse-engineer the xc tip bias $V_{\tau,xc}$ which corresponds to the

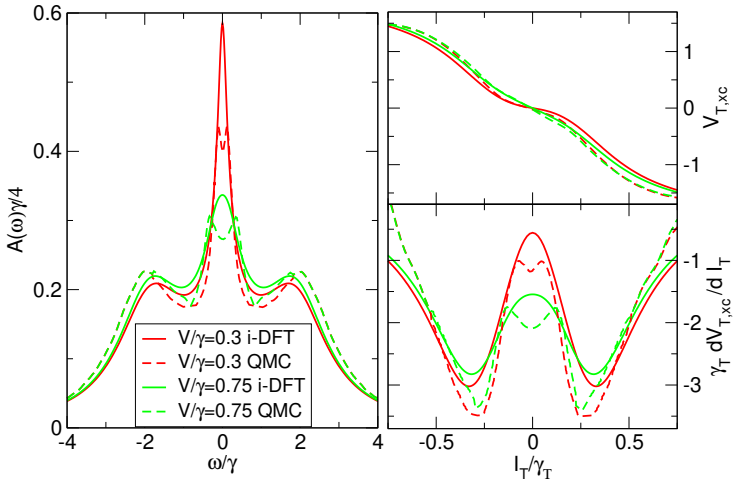

Figure 7.4: Left panel: i-DFT and QMC non-equilibrium spectral functions at particle-hole symmetry for $U/\gamma = 4$ with QMC results from ref. [111]. Upper right panel: xc tip bias as function of tip current I_τ at $N = 1$ and fixed current I corresponding to the two bias values. i-DFT results from our model tip xc bias of eq. (7.19), QMC results from reverse engineering using the QMC spectral function, see text. Lower right panel: derivatives of $V_{\tau,xc}$ of upper right panel with respect to I_τ.

given A. In the upper right panel of fig. 7.4 we extracted $V_{\tau,xc}$ as function of I_τ (for fixed values of n and I) corresponding to the QMC spectral functions of the left panel of the same figure and compare to our i-DFT functional of eq. (7.19). Although some differences are visible our approximate xc tip bias seems to agree rather well with the reverse engineered one. The missing feature becomes evident if we compare the derivatives of $V_{\tau,xc}$ with respect to I_τ, see lower right panel of fig. 7.4. While the derivative of the reverse engineered $V_{\tau,xc}$ exhibits a double peak in the vicinity of $I_\tau/\gamma_\tau \approx 0$, our approximation exhibits only a single maximum at $I_\tau/\gamma_\tau = 0$. Of course, the height as well as the positions of the maxima depend on the current I between the left and right leads. We have verified that using the reverse engineered $V_{\tau,xc}$ in eq. (7.11) the i-DFT and QMC spectral functions become indistinguishable. The correct incorporation of the double peak feature into an improved approximation for $V_{\tau,xc}$ is beyond the scope of this work. However, the established existence of this xc bias constitutes a proof-of-concept: i-DFT provides a numerically cheap method to calculate non-equilibrium spectral functions at zero and finite temperature.

8 Conclusions

In this thesis we have revisited and proposed different DFT frameworks which aim to describe the steady-state electrical and thermal transport driven by electrons through nanoscale junctions. Focusing on strongly correlated systems, the structure of the required exchange-correlation functionals in several basic model systems have been investigated.

Equilibrium properties of the Hxc functionals of multi-orbital quantum dots are addressed in part I, where we use the well studied single impurity problem as basis for the description of more complex situations. The Hxc potentials for double quantum dots in the grand-canonical ensemble subject to generic density-density interactions and Hund's rule coupling are studied in chapter 3 by reverse-engineering exact many-body solutions. At low temperatures, the structure of the Hxc potentials consists of ubiquitous steps whose exact positions depend on the regime defined by the interaction parameters. These structures can be understood and derived from an analysis of the stability diagrams. Alternatively, the decomposition of the interaction allows to rationalize the step structures of the Hxc potentials into basic components related to the single orbital problem which itself is parametrized in a straightforward manner. Furthermore, the decomposition into basic potentials is generalized to multi-orbital systems for the situation in which the intra-Coulomb repulsions are larger than the common inter-Coulomb repulsion between the dots.

DFT calculations employing the thus parametrized Hxc potentials for double, triple and quadruple quantum dots show excellent agreement with exact numerical results at low temperatures.

When contacting the quantum dots to electron reservoirs, interesting physical effects may arise. In chapter 4, we study the structure of the Hxc potentials of the double quantum dot when the couplings to the reservoirs is different for each dot. At low temperatures and similar on-site energies, the abrupt emptying of one impurity and the filling of the other impurity as the gate voltage is continuously varied, an effect known as level occupation switching. We constructed Hxc potentials which allow to qualitatively describe this effect. Comparison with accurate NRG results highlights the accuracy of the KS conductance at low temperatures, which is correctly described within the LB+DFT approach and is in agreement with the Friedel sum rule. However, the correct description of the DQD electrical conductances highly depends on the details of the Hxc functionals parametrization. A unified functional structure from the symmetric coupling to the completely asymmetric coupling to the electrodes is still an open question.

The non-equilibrium transport situation is considered in part II. A formally exact framework in this context is time-dependent DFT. Since in this thesis we are concerned with the steady-state regime, we consider a recently proposed general framework for steady-state electrical transport (i-DFT) [41] which has the advantage over TDDFT that the (H)xc functionals only depend on the molecular region. In chapter 5, we generalize i-DFT to the situation when there is a temperature gradient across the junction. As a direct consequence, we derive an exact expression for the Seebeck coefficient of the interacting system as a sum of the KS Seebeck coefficient and a correction term related to a derivative of the i-DFT xc bias functional. A general expression for the electronic contribution to the thermal conductance within i-DFT is also derived. For the SIAM we construct an approximation to the (H)xc functionals both in the Coulomb blockade as well as in the Kondo regime. In the Coulomb blockade regime we find that both Hxc gate and xc bias potential consist of a sum or difference of two pieces, each of which depends only on the

temperature of one of the leads. We compare the transport coefficients for the SIAM obtained with our method with those from NRG calculations reported in the literature. While our parametrization by construction becomes exact at high temperatures, in the Kondo regime ($T \ll T_K$) the agreement is reasonable but not perfect for the electrical conductance and the Seebeck coefficient. However, the i-DFT thermal conductance does not capture the correct many-body behaviour. This disagreement is expected since i-DFT is by construction meant for the description of the density in the molecular region and the electrical current through it, but is not supposed to also correctly capture the heat (or energy) current through the molecule. Therefore, in chapter 6 we propose a new density functional framework, which we call iq-DFT, to describe both electronic and heat (energy) transport in the steady-state for a (molecular) junction connected to $\mathcal{N}$ leads and driven out of equilibrium by external biases and/or temperature gradients. The foundation of iq-DFT rests on the one-to-one correspondence between the set of "densities" and the set of "potentials" which we prove for a window of finite biases and thermal gradients around equilibrium. The corresponding KS system requires $2\mathcal{N} - 1$ xc potentials which need to be approximated in practice. The i-DFT formalism may be viewed as an approximation to iq-DFT where the xc contributions to the Ψ- field are neglected completely and the xc contribution to the local (gate) potential is independent of the heat current. We develop the iq-DFT linear response formalism for the two-terminal situation which allows to access all linear thermal transport coefficients, i.e., the electrical conductance, the Seebeck coefficient, as well as the electronic contribution to the thermal conductance. All these coefficients can fully and exactly be expressed in terms of quantities accessible with iq-DFT, leading to xc corrections for all three transport coefficients. As a first example, we apply iq-DFT in the linear response regime to the Anderson model. From reverse engineering of a many-body model spectral function valid in the Coulomb blockade regime, we construct fully analytical parametrizations of the derivatives of the iq-DFT xc potentials which accurately reproduce the transport coefficients of the many-body model. These parametrizations are expected to serve as a first step

towards constructing of approximate xc functionals beyond the Coulomb blockade regime, in analogy to the previous chapter. As any DFT framework, due to the non-interacting nature of the KS system iq-DFT can be expected to be a highly efficient numerical scheme for the ab-initio calculation of current and heat transport through nanoscale systems as accurate approximations for the xc functionals become available. While the construction of such functionals which can be used in ab-initio calculations is still work for the future we hope that our studies on simple models can be a useful guide in this endeavor.

Finally in chapter 7, we generalize the i-DFT formalism for steady state transport through nanoscale junctions to the situation of multiple electrodes, a particular situation of the aforementioned multi-terminal iq-DFT. In particular, for a three-terminal setup in the limit of vanishing coupling to one of the electrodes (ideal STM limit), we show how to extract the non-equilibrium spectral function of the junction at both zero and finite temperature extending earlier work [108] which was restricted both to equilibrium and zero temperature. For the specific situation of an Anderson model coupled to three electrodes, we construct an approximate xc functional which describes, at least for not too strong interactions, the splitting of the Kondo peak at finite bias and yields results in reasonable qualitative agreement with computationally more demanding many-body approaches such as NRG and non-equilibrium QMC. Although for stronger interactions our approximation does not capture the splitting of the Kondo peak, we were nevertheless able to identify the missing feature which needs to be incorporated in future functionals. Since multi-terminal i-DFT is comparable in computational effort to standard LB+DFT calculations, it is therefore suitable to study systems currently inaccessible for accurate out of equilibrium many-body methods.

Appendices

A

Basic exchange-correlation functionals from model Hamiltonians

Contents

A.1 Single Site Model 113
A.2 Single Impurity Anderson Model 115
A.3 Constant Interaction Model 118

In this Appendix we derive the most common used functionals of the three main model Hamiltonians used throughout the different chapters. The main features of the xc potentials are steps whose slopes are governed by the effect of the coupling to the leads and the temperature.

A.1 Single Site Model

The total density of the single site model at finite temperature is described in the GCE by eq. (2.45). We can analytically invert the relationship between the density and the potential for the interacting system, finding

$$v = \frac{1}{\beta}\left(\log\left(1-2n-e^{-\beta U}\sqrt{(2n-1)^2e^{2\beta U}+4(1-n)e^{\beta U}}\right)-\log\left(2n\right)\right). \quad \text{(A.1)}$$

For the non-interacting system the corresponding Hamiltonian $\hat{H}_s^{\mathrm{SSM}} = v_s\hat{n}$ (found by turning off the interaction and replacing the gate level with the corresponding

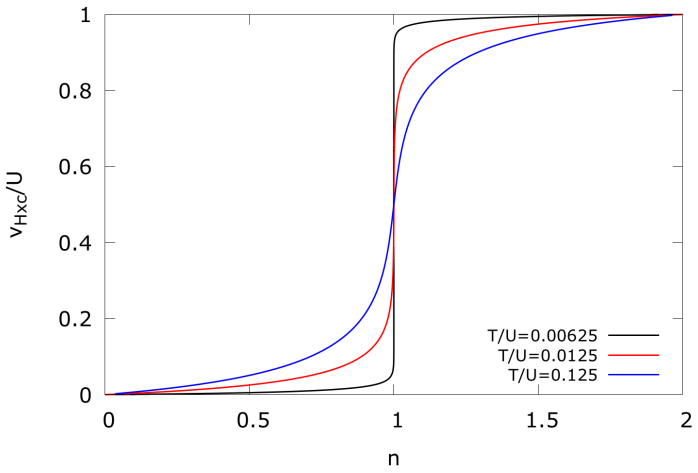

Figure A.1: SSM Hxc functional from eq. (A.3) as function of the density for different temperatures and $U = 8$.

non-interacting gate) leads to the density equation eq. (2.47). The inversion of the non-interacting relation allows to express the non-interacting gate as function of the density

$$v_s = \frac{1}{\beta} \log\left(\frac{2-n}{n}\right). \tag{A.2}$$

The difference between the non-interacting and the interacting potentials leads to the the exact Hxc functional for the Single Site Model

$$v_{\text{Hxc}}^{\text{SSM}}[n] = U + \frac{1}{\beta} \ln\left(\frac{x + \sqrt{x^2 + e^{-\beta U}(1-x^2)}}{1+x}\right) \tag{A.3}$$

where $x = n - 1$.

In fig. A.1 the $v_{\text{Hxc}}^{\text{SSM}}[n]$ is shown for different temperature values and strong correlations $U = 8$. The main feature is a step centered at $n = 1$ that becomes smoother as the temperature is increased. The two temperature limits for the functional are $v_{\text{Hxc}}^{\text{SSM}}(T = 0)[n] = \theta(n-1)$ (where $\theta(x)$ is the Heaviside step function) and $v_{\text{Hxc}}^{\text{SSM}}(T \to \infty)[n] = v_H^{\text{SSM}}[n] = \frac{U}{2}n$. The corresponding step height at low temperatures is equal to the Coulomb repulsion U. This property can alternatively be derived from the study of the xc contribution of the derivative discontinuity.

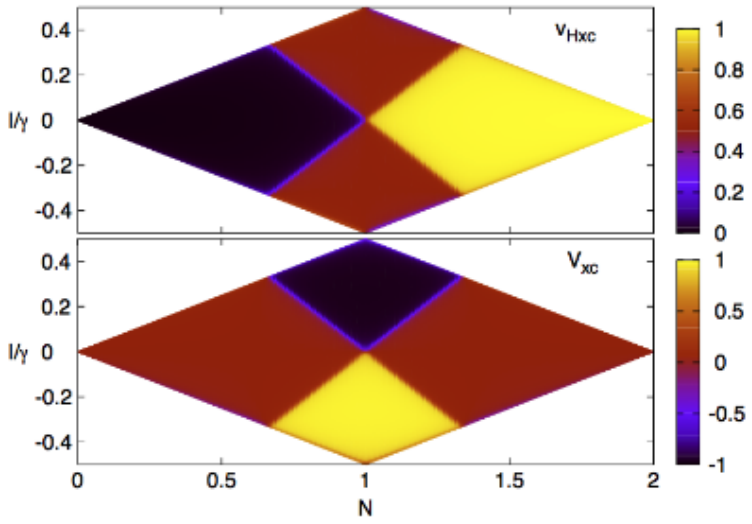

Figure A.2: RE i-DFT functionals for the SIAM in units of the Coulomb repulsion U.

A.2 Single Impurity Anderson Model

In the original i-DFT publication [41], a couple of simple and accurate functionals were constructed from a reverse engineering procedure for the SIAM. The authors numerically explored the required functionals in order to obtain the same density and steady current as the MBM (see eq. (2.49)). In fig. A.2 the numerically RE functionals are shown in units of the Coulomb repulsion U. The main features of these pair of potentials are some steps along the diagonals $N = 1 \mp I/\gamma$. From this observation, a reasonable fit for the pair of xc functionals for the SIAM (in the i-DFT framework) for the CB regime is:

$$\tilde{v}_{\mathrm{Hxc}}[n, I] = \frac{U}{4} \sum_{s=\pm} \left[1 + \frac{2}{\pi} \operatorname{atan}\left(\frac{n + \frac{s}{\gamma} I - 1}{W_0} \right) \right], \tag{A.4}$$

$$\tilde{V}_{\mathrm{xc}}[n, I] = -U \sum_{s=\pm} \frac{s}{\pi} \operatorname{atan}\left(\frac{n + \frac{s}{\gamma} I - 1}{W_0} \right). \tag{A.5}$$

with $W_0 = 0.16\gamma/U$. In later works [45], this parametrization was generalized to describe also the transition to the Kondo regime

$$v_{\mathrm{Hxc}}[n, I] = \left(1 - a^{(T)}[I] b^{(T)}[n]\right) \tilde{v}_{\mathrm{Hxc}}[n, I] + a^{(T)}[I] b^{(T)}[n] v^{(0)}_{\mathrm{Hxc}}[n], \tag{A.6}$$

$$V_{\mathrm{xc}}[n, I] = \left(1 - a^{(T)}[I] b^{(T)}[n]\right) \tilde{V}_{\mathrm{xc}}[n, I]), \tag{A.7}$$

where the temperature dependent fitting parameters take the form

$$a^{(T)}[I] = 1 - \left[\frac{2}{\pi}\,\mathrm{atan}\left(\frac{I}{\gamma W(T)}\right)\right]^2, \tag{A.8a}$$

$$b^{T}[n] = 1 + \frac{c^{(T)}[n]}{\frac{\partial \tilde{V}_{\mathrm{xc}}}{\partial I}\Big|_{n=1,I=0}}\left(\frac{1}{G_{univ}} - \frac{1}{G_{ph,0}}\right), \tag{A.8b}$$

$$c^{(T)}[n] = 1 + \frac{4}{\pi^2}\,\mathrm{atan}\left(\frac{6-\frac{U}{\gamma}}{3W(T)}\right)\mathrm{atan}\left(\left(\frac{n-1}{3W(T)}\right)^2\right), \tag{A.8c}$$

with $G_{ph,0} = G_{ph,s}(0)$, G_{univ} is the universal conductance given in ref. [112] and $W(T) = W_0(1 + 9(T/\gamma)^2)$.

The low temperature functional $v_{\mathrm{Hxc}}^{(0)}$ corresponds to an accurate parametrization derived in ref. [84] through a fit to RE results obtained through Bethe ansatz approach for the Hxc potential of the SIAM for $T = 0$

$$v_{\mathrm{Hxc}}^{(0)} = U\frac{n}{2} + \alpha\frac{U}{2}\left(1 - n - \frac{2}{\pi}\arctan\left(\frac{1-n}{\sigma}\right)\right), \tag{A.9}$$

with $\alpha = U/(U + 2.84\gamma)$ and $\sigma = 0.4055\gamma/U + 0.0975(\gamma/U)^2 + 0.021(\gamma/U)^3$. Since this functional is by construction accurate in the range $n \in [0.1, 1.9]$, in chapter 4 we make a linear interpolation outside this range to ensure that $v_{\mathrm{Hxc}}^{\mathrm{SIAM}}[n = 0] = 0$ and $v_{\mathrm{Hxc}}^{SIAM}[n = 2] = U$ (for the construction of the DFT 1 parametrization). For the description of the SIAM, this range of densities corresponding to almost empty/full occupation does not require high accuracy in the functional, but in the DQD problem where we use the SIAM functional as a basic ingredient, small discrepancies with respect to the exact functional in this regime lead to significant deviations in the conductance.

We can analytically invert [47, 85, 113] the (exact) SIAM xc functionals for the high temperature regime ($T > \gamma$) with explicit thermal gradient dependence. We consider the density and current expressions in terms of the interacting potentials

making use of the SSM spectral function eq. (2.46)

$$\begin{aligned} n &= \int dw \left(f_L(w - \frac{V}{2}) + f_R(w + \frac{V}{2}) \right) \left[\left(1 - \frac{n}{2} \right) \delta(w - v) + \frac{n}{2} \delta(w - v - U) \right] \\ &= \left(1 - \frac{n}{2} \right) \left(f_L(z_L) + f_R(z_R) \right) + \frac{n}{2} \left(f_L(z_L + U) + f(z_R + U) \right) \end{aligned} \tag{A.10}$$

$$\begin{aligned} 2I/\gamma &= \int dw \left(f_L(w - \frac{V}{2}) - f_R(w + \frac{V}{2}) \right) \left[\left(1 - \frac{n}{2} \right) \delta(w - v) + \frac{n}{2} \delta(w - v - U) \right] \\ &= \left(1 - \frac{n}{2} \right) \left(f_L(z_L) - f_R(z_R) \right) + \frac{n}{2} \left(f_L(z_L + U) - f_R(z_R + U) \right) \end{aligned} \tag{A.11}$$

where we have introduced $z_\alpha = v \mp \frac{V}{2}$ or $\alpha = L, R$. We can combine the previous equations such that

$$N + x_\alpha = (2 - n) f_\alpha(z_\alpha) + n f_\alpha(z_\alpha + U) \tag{A.12}$$

where $x_\alpha = \pm 2I/\gamma$. Eq. (A.12) is a quadratic equation for $s_\alpha = e^{\frac{z_\alpha}{T_\alpha}}$

$$a_\alpha s_\alpha^2 + b_\alpha s_\alpha + c_\alpha = 0 \tag{A.13}$$

with $a_\alpha = e^{\frac{U}{T_\alpha}} (n + x_\alpha)$, $b_\alpha = e^{\frac{U}{T_\alpha}} (2n + x_\alpha - 2) + x_\alpha$, and $c_\alpha = n + x_\alpha - 2$. Solving for s_α and taking into account that $z_\alpha = T_\alpha \log(s_\alpha)$ we have

$$z_\alpha = T_\alpha \log \left(\frac{1}{2a_\alpha} \left(-b_\alpha \pm \sqrt{b_\alpha^2 - 4a_\alpha c_\alpha} \right) \right). \tag{A.14}$$

We can follow an analogous procedure for the non-interacting system ($U = 0$)

$$\begin{aligned} N + x_\alpha = 2 f(z_{\alpha,s}) = \frac{2}{e^{\frac{z_{\alpha,s}}{T_\alpha}} + 1} \\ \implies e^{\frac{z_{\alpha,s}}{T_\alpha}} (n + x_\alpha) = -c_\alpha \implies z_{\alpha,s} = T_\alpha \log \left(\frac{-c_\alpha e^{\frac{U}{T_\alpha}}}{a_\alpha} \right). \end{aligned} \tag{A.15}$$

The difference of eq. (A.15) and eq. (A.14) leads to

$$g_{\mathrm{Hxc}}(n, \pm 2I/\gamma, T_{L/R}) = z_{L/R,xc}(n, x_\pm) = T_{L/R} \log \left(\frac{-2c_{L/R} e^{\frac{U}{T_{L/R}}}}{-b \pm \sqrt{b_{L/R}^2 - 4a_{L/R} c_{L/R}}} \right). \tag{A.16}$$

Substituting the values for the parameters (a, b, c), choosing the negative sign for the square root (this condition impose the positive sign of the log) and simplifying the results, we arrive to the final expression

$$v_{\mathrm{Hxc}} = \frac{1}{2} \left(g_{\mathrm{Hxc}}(n, -I, T_R) + g_{\mathrm{Hxc}}(n, I, T_L) \right) \tag{A.17}$$

$$V_{\mathrm{xc}} = g_{\mathrm{Hxc}}(n, -I, T_R) - g_{\mathrm{Hxc}}(n, I, T_L) \tag{A.18}$$

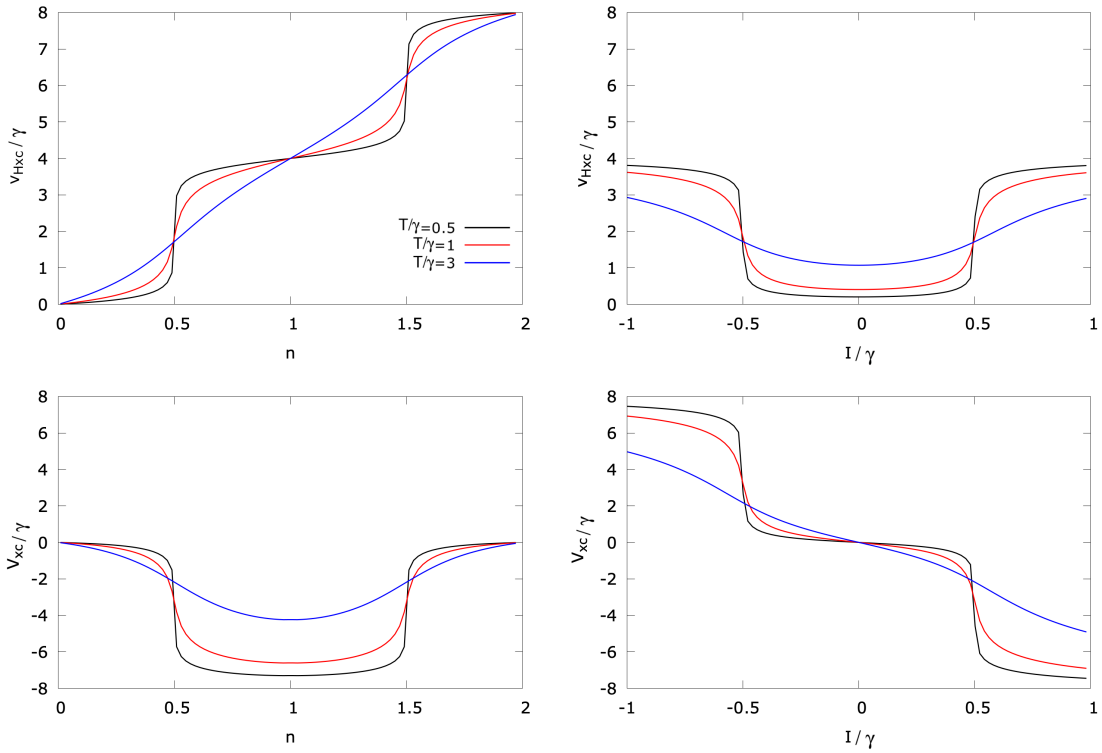

Figure A.3: xc functionals eqs. (A.17) and (A.18) for different temperatures when $U/\gamma = 8$. In the left figures $I/\gamma = 0.5$ while in the right figures $n = 0.5$.

with

$$g_{\mathrm{Hxc}}(n, I, T) = \begin{cases} T \log\left(\frac{-1}{p}\right) & \text{if} \quad j = 0 \\ U + T \log\left(\frac{p+\sqrt{p^2 - zje^{-U/T}}}{j}\right) & \text{if} \quad p \geq 0 \\ T \log\left(\frac{z}{p-\sqrt{p^2 - zje^{-U/T}}}\right) & \text{if} \quad p < 0 \end{cases} \tag{A.19}$$

where $z = j - 2$, $p = n - n_{crit}$, $n_{crit} = 1 - I/\gamma\left(1 + e^{-U/T}\right)$ and $j = 2I/\gamma + n$.

In fig. A.3 the xc functionals from eqs. (A.17) and (A.18) are presented as function of one basic variable (the other fixed to 0.5) for different temperatures and strong correlations $U/\gamma = 8$. The i-DFT density and current results obtained making use of these functionals are shown in fig. 2.3.

A.3 Constant Interaction Model

From the numerical observation of the RE xc functionals for the CIM, a simple parametrization was proposed in the original i-DFT formulation [41] based on

the xc functionals of the SIAM

$$v_{\rm Hxc}^{\rm CIM}[N,I] = \frac{U}{4}\sum_{k=1}^{2\mathcal{M}-1}\sum_{s=\pm}\left[1+\frac{2}{\pi}\,\mathrm{atan}\left(\frac{\Delta_K^{(s)(N,I)}}{W}\right)\right] \tag{A.20}$$

$$V_{\rm xc}^{\rm CIM}[N,I] = -U\sum_{k=1}^{2\mathcal{M}-1}\sum_{s=\pm}\frac{s}{\pi}\,\mathrm{atan}\left(\frac{\Delta_K^{(s)(N,I)}}{W}\right), \tag{A.21}$$

here $\mathcal{M}$ is the number of levels in the CIM and $\Delta_K^{(s)}$ is a the piece-wise linear function of N and I which vanishes along the step edge passing through $(K,0)$ with positive ($s=+1$) or negative ($s=-1$) slopes (the value of the slopes depends on K, see[41]).

In situations of equilibrium, i.e., when the steady current $I=0$, the functional $v_{\rm Hxc}^{\rm CIM}$ shows an interesting property at low temperatures: It can be seen as the addition of steps centered at integer values of the total occupation provided by simpler models

$$v_{\rm Hxc}^{\rm CIM}[N] = \sum_{k}^{2\mathcal{M}-1} v_{\rm Hxc}^{X}[N+1-k], \tag{A.22}$$

where $X = SSM, SIAM$ depending if our system is coupled to the leads. We require that $v_{\rm Hxc}^{X}[N+1-k]=0$ if $N+1-k<0$ and $v_{\rm Hxc}^{X}[N+1-k]=U$ if $N+1-k>2$. We denote eq. (A.22) as the DFT 1 approximation for the Hxc potential of the CIM. The accuracy of this approximation can be numerically checked by comparing with the exact RE result, see [15].

The essential features of the density at low temperatures are correctly described with the simple functional structure of eq. (A.22). One structural problem emerges as the temperature is increased: In fig. A.4 the CIM functionals for $\mathcal{M}=2$ are shown. The DFT 1 result shows excellent agreement with the RE (see [15]) at low temperatures, but for $T=3$ the functional considerably differs from the RE. In particular, it shows 3 straight lines connecting the regions $N\in[0,1]$,$N\in[1,3]$ and $N\in[3,4]$. By construction, eq. (A.22) is fixed to $v_{\rm Hxc}^{\rm CIM}[N=1]=U/2$, $v_{\rm Hxc}^{\rm CIM}[N=3]=5U/2$ which does not correspond to the RE functional values at high temperatures. In order to correct this behaviour, we proposed [72] an alternative to eq. (A.22) by considering the sum of the three $v_{\rm Hxc}^{X}$ steps (without imposing any restriction if $N+1-k<0$ or $N+1-k>2$) and then shifting and rescaling the

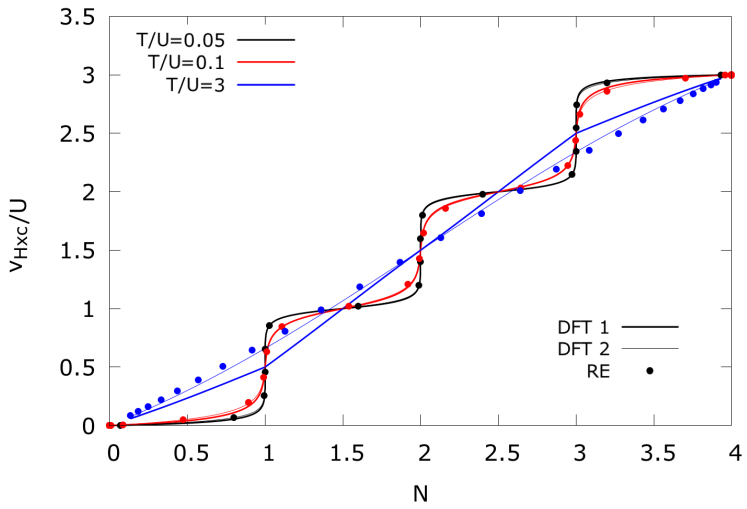

Figure A.4: v_{Hxc} functional comparison for the uncontacted degenerated CIM between DFT 1 (eq. (A.22)), DFT 2 (eq. (A.23)) and the exact RE result for different temperatures and Coulomb repulsion $U = 1$.

functional to fix the extremes $v^{\mathrm{CIM}}_{\mathrm{Hxc}}[N = 0] = 0$ and $v^{\mathrm{CIM}}_{\mathrm{Hxc}}[N = 2\mathcal{M}] = (2\mathcal{M} - 1)U$. Formally, this (DFT 2) corresponds to

$$v^{\mathrm{CIM}}_{\mathrm{Hxc}}[N] = \frac{(2\mathcal{M} - 1)U}{v^{\mathrm{max}}_{\mathrm{CIM}}} \sum_{k=1}^{2M-1} \left[v^{X}_{\mathrm{Hxc}}[N + 1 - k] - v^{X}_{\mathrm{Hxc}}[1 - k] \right] \tag{A.23}$$

where

$$v^{\mathrm{max}}_{\mathrm{CIM}} = \sum_{J=1}^{2M-1} \left[v^{X}_{\mathrm{Hxc}}[2\mathcal{M} - J + 1] - v^{X}_{\mathrm{Hxc}}[-J + 1] \right]. \tag{A.24}$$

is the maximal value that the sum in eq. (A.23) acquires at $N = 2\mathcal{M}$. The prefactor $(2\mathcal{M} - 1)U/v^{\mathrm{max}}_{\mathrm{CIM}}$ thus rescales the potential such that the potential yields the exact value $(2M - 1)U$ at $N = 2\mathcal{M}$.

In fig. A.4 can be observed that although the discrepancies between eq. (A.22) and eq. (A.23) are irrelevant at low temperatures, the functional at high temperatures is corrected with eq. (A.23) (DFT 2).

B

Analytic expressions for the transport integrals in the Single Impurity Anderson Model

In this Appendix we analytically evaluate the most important integrals needed both in the MBM and in the construction of our parametrization for the derivatives of the iq-DFT xc potentials. In our MBM for the SIAM, the many-body spectral function consists of two Lorentzians with broadening γ ($\gamma > 0$) centered at v and $v + U$, see eq. (2.49). Therefore, all integrals needed to compute the MBM density and currents have the form $\int d\omega \omega^n f(\omega) A(\omega)$ with $n = 0, 1$. The first integral we are interested in is

$$\mathcal{I}_1 = \int_{-\infty}^{\infty} f(x - V/2) \frac{\gamma}{(x - x_0)^2 + \frac{\gamma^2}{4}} \mathrm{d}x, \tag{B.1}$$

where the Fermi function $f(z)$ can be expanded as [114]

$$f(z) = \frac{1}{1 + e^{\frac{z}{T}}} = \frac{1}{2} - \frac{\mathrm{i}}{2\pi} \sum_{n=0}^{\infty} \frac{1}{n + \frac{1}{2} + \mathrm{i}\frac{z}{2\pi T}}. \tag{B.2}$$

Using the substitution $x = V/2 + Tz$ and the abbreviations $a = \frac{x_0 - V/2}{T}$ and $b = \frac{\gamma}{2T}$, we can write the integral as

$$\mathcal{I}_1 = 2b \int_{-\infty}^{\infty} \frac{\mathrm{d}z}{(\mathrm{e}^z + 1)[(z - a)^2 + b^2]} \equiv 2b \int_{-\infty}^{\infty} g(z) \mathrm{d}z. \tag{B.3}$$

The integrand $g(z)$ has only single poles with non-vanishing imaginary part in the complex plane. We therefore use the calculus of residues to compute this integral. $g(z)$ has simple poles at $a \pm \mathrm{i}b$ with residues

$$\mathrm{Res}(g, a \pm \mathrm{i}b) = \pm \frac{1}{2\mathrm{i}b(\mathrm{e}^{a \pm \mathrm{i}b} + 1)} \tag{B.4}$$

and at $\pm(2n+1)\pi\mathrm{i}$ with residues

$$\mathrm{Res}(g, \pm(2n+1)\pi\mathrm{i}) = -\frac{1}{[(2n+1)\pi\mathrm{i} \mp a]^2 + b^2} \tag{B.5}$$

for $n \in \mathbb{N}_0$. Since $g(z)$ vanishes sufficiently fast as $|z| \to \infty$ we can close the integration contour by a semi-circle with infinite radius in the upper half plane (avoiding the poles on the imaginary axis). The integral then can be evaluated as

$$\mathcal{I}_1 = 4b\pi\mathrm{i}\left[\frac{1}{\mathrm{i}2b(\mathrm{e}^{a+\mathrm{i}b}+1)} - \sum_{n=0}^{\infty} \frac{1}{[(2n+1)\pi\mathrm{i} - a]^2 + b^2}\right]. \tag{B.6}$$

For the terms in the sum, we perform a fractional decomposition and then use the series representation of the digamma function ψ

$$\psi(z) = \sum_{n=0}^{\infty}\left(\frac{1}{n+1} - \frac{1}{n+z}\right) - \gamma^{EM}, \tag{B.7}$$

with the Euler-Mascheroni constant $\gamma^{EM} \sim 0.5772$ to obtain

$$\mathcal{I}_1 = 2\pi\left[\frac{1}{\mathrm{e}^{a+\mathrm{i}b}+1} - \frac{1}{2\pi\mathrm{i}}\psi\left(\frac{1}{2} + \frac{b+\mathrm{i}a}{2\pi}\right) + \frac{1}{2\pi\mathrm{i}}\psi\left(\frac{1}{2} + \frac{-b+\mathrm{i}a}{2\pi}\right)\right]. \tag{B.8}$$

We then apply the reflection formula

$$\psi(1-z) = \psi(z) + \pi\cot(\pi z)$$

to the last term together with the properties

$$\mathrm{Im}\left[\psi(x+\mathrm{i}y)\right] = \frac{\mathrm{i}}{2}\left(\psi(x-\mathrm{i}y) - \psi(x+\mathrm{i}y)\right)$$
$$\frac{1}{e^z+1} + \frac{\mathrm{i}}{2}\tan\left(\frac{-\mathrm{i}z}{2}\right) = \frac{1}{2}$$

and simplify te result

$$\begin{aligned}\mathcal{I} &= 2\pi\left[\frac{1}{\mathrm{e}^{a+\mathrm{i}b}+1} - \frac{1}{2\mathrm{i}}\tan\left(\frac{b-\mathrm{i}a}{2}\right) - \frac{1}{2\pi\mathrm{i}}\left(\psi\left(\frac{1}{2}+\frac{b+\mathrm{i}a}{2\pi}\right) - \psi\left(\frac{1}{2}+\frac{\beta-\mathrm{i}a}{2\pi}\right)\right)\right] \\ &= 2\pi\left[\frac{1}{2} - \frac{1}{\pi}\,\mathrm{Im}\left(\psi\left(\frac{1}{2}+\frac{b+\mathrm{i}a}{2\pi}\right)\right)\right] = \pi - 2\,\mathrm{Im}\left[\psi\left(\frac{1}{2}+\frac{b+\mathrm{i}a}{2\pi}\right)\right].\end{aligned} \tag{B.9}$$

Returning to the original parameters, we finally arrive at

$$\mathcal{I}_1(\gamma, x_0, V/2, T) = \pi - 2\,\mathrm{Im}\left[\psi\left(\frac{1}{2} + \frac{\frac{\gamma}{2} + \mathrm{i}(x_0 - V/2)}{2\pi T}\right)\right]. \tag{B.10}$$

The second integral we are interested in is

$$\mathcal{I}_2 = \int_{-\infty}^{\infty} \mathrm{d}x\, \left(f(\frac{x - V/2}{1 + \Psi/2}) - f(\frac{x + V/2}{1 - \Psi/2})\right) \frac{x\gamma}{(x - x_0)^2 + \frac{\gamma^2}{4}}\,, \tag{B.11}$$

where $\Psi = \frac{T_L - T_R}{T}$. We can rewrite $\mathcal{I}_2$ by decomposing the second factor as

$$\frac{x\gamma}{(x - x_0)^2 + \frac{\gamma^2}{4}} = \frac{\gamma}{2}\left[G^A(x) + G^R(x)\right] - \mathrm{i}x_0\left[G^A(x) - G^R(x)\right] \tag{B.12}$$

with the advanced and retarded Green function $G^{A/R}(x) = \frac{1}{x - \left(x_0 \pm \mathrm{i}\frac{\gamma}{2}\right)}$. Noting that the last term on the r.h.s. of Eq. (B.12) reduces to a Lorentzian we obtain

$$\mathcal{I}_2 = \mathcal{I}_2^A + \mathcal{I}_2^R + x_0\mathcal{I}_3, \tag{B.13}$$

where $\mathcal{I}_3 = \mathcal{I}_1\left(\gamma, x_0, V/2, T_L\right) - \mathcal{I}_1(\gamma, x_0, -V/2, T_R)$ and we have defined

$$\mathcal{I}_2^{A/R} = \frac{\gamma}{2}\lim_{r\to\infty}\int_{-r}^{\infty} \mathrm{d}x\; G^{A/R}(x)\left[f\left(\frac{x - V/2}{1 + \Psi/2}\right) - f\left(\frac{x + V/2}{1 - \Psi/2}\right)\right]. \tag{B.14}$$

The integrals $\mathcal{I}_2^{A/R}$ are convergent because the difference of the Fermi functions decays asymptotically at least as x^{-1} as $|x| \to \infty$ and the Green function contributes another asymptotic x^{-1} behaviour in the same limit. Note that a lower cutoff has been explicitly introduced in Eq. (B.14) to correctly account for the non-equivalent asymptotics of the two Fermi functions due to their generally different temperatures (in general, $\Psi \neq 0$).

By simple variable substitution, the integrals $\mathcal{I}_2^{A/R}$ can be written as

$$\begin{aligned}\mathcal{I}_2^{A/R} =& \frac{\gamma}{2}\lim_{r\to\infty}\int_{\frac{-r+V/2}{1-\psi/2}}^{\infty} \mathrm{d}z f_T(z)\left(\frac{1}{z + \frac{V/2 - (x_0 \pm i\gamma/2)}{1+\Psi/2}} - \frac{1}{z + \frac{-V/2 - (x_0 \pm i\gamma/2)}{1-\Psi/2}}\right) \\ &+ \frac{\gamma}{2}\lim_{r\to\infty}\int_{\frac{-r-V/2}{1+\psi/2}}^{\frac{-r+V/2}{1-\psi/2}} \mathrm{d}z\, \frac{f_T(z)}{z + \frac{V/2 - (x_0 \pm i\gamma/2)}{1+\Psi/2}}.\end{aligned} \tag{B.15}$$

The first contribution can now again be evaluated by closing the contour with a semicircle in the upper half plane and summing the residues of all poles inside the

contours. On the other hand, the second integral becomes trivial by replacing $f(z)$ with unity which is justified in the limit $r \to \infty$. This leads to

$$\begin{aligned}\mathcal{I}^A =& \frac{\gamma}{2}\left[\psi\left(\frac{1}{2}+\frac{\gamma/2-\mathrm{i}(x_0-V/2)}{2\pi T_L}\right)-\psi\left(\frac{1}{2}+\frac{\gamma/2-\mathrm{i}(x_0+V/2)}{2\pi T_R}\right)\right] \\ &+\frac{\gamma}{2}\log\left(\frac{1+\Psi/2}{1-\Psi/2}\right).\end{aligned} \tag{B.16}$$

and

$$\begin{aligned}\mathcal{I}^R =& \frac{\gamma}{2}\left[\psi\left(\frac{1}{2}+\frac{\gamma/2+\mathrm{i}(x_0-V/2)}{2\pi T_L}\right)-\psi\left(\frac{1}{2}+\frac{\gamma/2+\mathrm{i}(x_0+V/2)}{2\pi T_R}\right)\right] \\ &+\frac{\gamma}{2}\log\left(\frac{1+\Psi/2}{1-\Psi/2}\right).\end{aligned} \tag{B.17}$$

Using $\mathrm{Re}\left(\psi(a+\mathrm{i}b)\right) = \frac{1}{2}\left(\psi(a+\mathrm{i}b)+\psi(a-\mathrm{i}b)\right)$ we arrive at the final result for our second integral

$$\begin{aligned}\mathcal{I}_2 \;=\; & \gamma\,\mathrm{Re}\left[\psi\left(\frac{1}{2}+\frac{\gamma/2+\mathrm{i}(x_0-V/2)}{2\pi T_L}\right)\right]-\gamma\,\mathrm{Re}\left[\psi\left(\frac{1}{2}+\frac{\gamma/2+\mathrm{i}(x_0+V/2)}{2\pi T_R}\right)\right] \\ &+x_0\mathcal{I}_3+\gamma\log\left(\frac{1+\Psi/2}{1-\Psi/2}\right).\end{aligned} \tag{B.18}$$

The results for the integrals of Eqs. (B.10) and (B.18) are sufficient to analytically evaluate the density and currents for the SIAM both in the many-body model as well as in the KS system. With these integrals we can also derive the analytical expressions for the integrals entering the transport coefficients in the linear esponse regime. These coefficients are

$$M_{11}(v) = \frac{\gamma}{4\pi}\left.\frac{\mathrm{d}\mathcal{I}_3}{\mathrm{d}V}\right|_{\substack{V=0\\ \Psi=0}} = \frac{-\gamma^2}{4\pi}\int f'(\omega)\frac{\mathrm{d}\omega}{(\omega-v)^2+\frac{\gamma^2}{4}} = \frac{\gamma}{4\pi^2 T}\,\mathrm{Im}\left(\mathrm{i}\psi^{(1)}(z_1)\right) \tag{B.19a}$$

$$M_{12}(v) = \frac{\gamma}{4\pi}\left.\frac{\mathrm{d}\mathcal{I}_2}{\mathrm{d}V}\right|_{\substack{V=0\\ \Psi=0}} = \frac{-\gamma^2}{4\pi}\int f'(\omega)\frac{\omega\,\mathrm{d}\omega}{(\omega-v)^2+\frac{\gamma^2}{4}} = \frac{\gamma}{4\pi^2 T}\,\mathrm{Im}\left(z_0\psi^{(1)}(z_1)\right) \tag{B.19b}$$

$$\begin{aligned}M_{22}(v) = \frac{\gamma}{4\pi}\left.\frac{d\mathcal{I}_2}{d\Psi}\right|_{\substack{V=0\\ \Psi=0}} &= \frac{-\gamma^2}{4\pi}\int f'(\omega)\frac{\omega^2\,\mathrm{d}\omega}{(\omega-v)^2+\frac{\gamma^2}{4}} = -\frac{\gamma^2}{8\pi^2 T}\,\mathrm{Re}\left(z_0\psi^{(1)}(z_1)\right) \\ &+vM_{12}+\frac{\gamma^2}{4\pi},\end{aligned} \tag{B.19c}$$

where $z_0 = \frac{\gamma}{2}+\mathrm{i}v$, $z_1 = \frac{1}{2}+\frac{z_0}{2\pi T}$, and $\psi^{(1)}(z)$ is the trigamma function [89].

References

[1] Eberhard KU Gross and Reiner M Dreizler. *Density functional theory*. Vol. 337. Springer Science & Business Media, 2013.

[2] Carsten A Ullrich. *Time-dependent density-functional theory: concepts and applications*. OUP Oxford, 2011.

[3] Neepa T Maitra. "Perspective: Fundamental aspects of time-dependent density functional theory". In: *The Journal of Chemical Physics* 144.22 (2016), p. 220901.

[4] José M Soler et al. "The SIESTA method for ab initio order-N materials simulation". In: *Journal of Physics: Condensed Matter* 14.11 (2002), p. 2745.

[5] Daniel Sánchez-Portal et al. "Density-functional method for very large systems with LCAO basis sets". In: *International journal of quantum chemistry* 65.5 (1997), pp. 453–461.

[6] Emilio Artacho et al. "Linear-scaling ab-initio calculations for large and complex systems". In: *physica status solidi (b)* 215.1 (1999), pp. 809–817.

[7] Axel D Becke. "Density-functional thermochemistry. I. The effect of the exchange-only gradient correction". In: *The Journal of chemical physics* 96.3 (1992), pp. 2155–2160.

[8] Yan Zhao and Donald G Truhlar. "Density functionals with broad applicability in chemistry". In: *Accounts of chemical research* 41.2 (2008), pp. 157–167.

[9] Kieron Burke. "Perspective on density functional theory". In: *The Journal of chemical physics* 136.15 (2012), p. 150901.

[10] Aron J Cohen, Paula Mori-Sánchez, and Weitao Yang. "Insights into current limitations of density functional theory". In: *Science* 321.5890 (2008), pp. 792–794.

[11] Paula Mori-Sánchez, Aron J Cohen, and Weitao Yang. "Discontinuous nature of the exchange-correlation functional in strongly correlated systems". In: *Physical review letters* 102.6 (2009), p. 066403.

[12] Francesc Malet and Paola Gori-Giorgi. "Strong correlation in Kohn-Sham density functional theory". In: *Physical review letters* 109.24 (2012), p. 246402.

[13] Francesc Malet et al. "Exchange–correlation functionals from the strong interaction limit of DFT: applications to model chemical systems". In: *Physical Chemistry Chemical Physics* 16.28 (2014), pp. 14551–14558.

[14] Paola Gori-Giorgi, Michael Seidl, and Giovanni Vignale. "Density-functional theory for strongly interacting electrons". In: *Physical review letters* 103.16 (2009), p. 166402.

[15] S Kurth and G Stefanucci. "Transport through correlated systems with density functional theory". In: *Journal of Physics: Condensed Matter* 29.41 (2017), p. 413002.

[16] NA Lima et al. "Density functionals not based on the electron gas: Local-density approximation for a luttinger liquid". In: *Physical review letters* 90.14 (2003), p. 146402.

[17] Klaus Capelle and Vivaldo L Campo Jr. "Density functionals and model Hamiltonians: Pillars of many-particle physics". In: *Physics Reports* 528.3 (2013), pp. 91–159.

[18] NA Lima, LN Oliveira, and Klaus Capelle. "Density-functional study of the Mott gap in the Hubbard model". In: *EPL (Europhysics Letters)* 60.4 (2002), p. 601.

[19] Andrea Droghetti and Ivan Rungger. "Quantum transport simulation scheme including strong correlations and its application to organic radicals adsorbed on gold". In: *Physical Review B* 95.8 (2017), p. 085131.

[20] Liviu Chioncel et al. "Transmission through correlated Cu n Co Cu n heterostructures". In: *Physical Review B* 92.5 (2015), p. 054431.

[21] Wilhelm H Appelt et al. "Predicting the conductance of strongly correlated molecules: the Kondo effect in perchlorotriphenylmethyl/Au junctions". In: *Nanoscale* 10.37 (2018), pp. 17738–17750.

[22] David Jacob. "Towards a full ab initio theory of strong electronic correlations in nanoscale devices". In: *Journal of Physics: Condensed Matter* 27.24 (2015), p. 245606.

[23] DJ Carrascal and Jaime Ferrer. "Exact Kohn-Sham eigenstates versus quasiparticles in simple models of strongly correlated electrons". In: *Physical Review B* 85.4 (2012), p. 045110.

[24] David Jacob, Gianluca Stefanucci, and Stefan Kurth. "Mott metal-insulator transition from steady-state density functional theory". In: *Physical Review Letters* 125.21 (2020), p. 216401.

[25] Lucas O Wagner et al. "Guaranteed convergence of the kohn-sham equations". In: *Physical review letters* 111.9 (2013), p. 093003.

[26] S Kurth and Gianluca Stefanucci. "Dynamical correction to linear Kohn-Sham conductances from static density functional theory". In: *Physical review letters* 111.3 (2013), p. 030601.

[27] Erich Runge and Eberhard KU Gross. "Density-functional theory for time-dependent systems". In: *Physical Review Letters* 52.12 (1984), p. 997.

[28] Mark E Casida. "Time-dependent density functional response theory for molecules". In: *Recent Advances In Density Functional Methods: (Part I)*. World Scientific, 1995, pp. 155–192.

[29] MGUJ Petersilka, UJ Gossmann, and EKU Gross. "Excitation energies from time-dependent density-functional theory". In: *Physical review letters* 76.8 (1996), p. 1212.

[30] Gianluca Stefanucci and C-O Almbladh. "Time-dependent quantum transport: An exact formulation based on TDDFT". In: *EPL (Europhysics Letters)* 67.1 (2004), p. 14.

[31] Na Sai et al. "Dynamical corrections to the DFT-LDA electron conductance in nanoscale systems". In: *Physical review letters* 94.18 (2005), p. 186810.

[32] Max Koentopp, Kieron Burke, and Ferdinand Evers. "Zero-bias molecular electronics: Exchange-correlation corrections to Landauer's formula". In: *Physical Review B* 73.12 (2006), p. 121403.

[33] Giovanni Vignale and Massimiliano Di Ventra. "Incompleteness of the Landauer formula for electronic transport". In: *Physical Review B* 79.1 (2009), p. 014201.

[34] Florian G Eich, M Di Ventra, and G Vignale. "Density-functional theory of thermoelectric phenomena". In: *Physical review letters* 112.19 (2014), p. 196401.

[35] FG Eich et al. "Luttinger-field approach to thermoelectric transport in nanoscale conductors". In: *Physical Review B* 90.11 (2014), p. 115116.

[36] FG Eich, M Di Ventra, and G Vignale. "Functional theories of thermoelectric phenomena". In: *Journal of Physics: Condensed Matter* 29.6 (2016), p. 063001.

[37] Fabio Covito et al. "Transient charge and energy flow in the wide-band limit". In: *Journal of chemical theory and computation* 14.5 (2018), pp. 2495–2504.

[38] ND Lang. "Resistance of atomic wires". In: *Physical Review B* 52.7 (1995), p. 5335.

[39] Rolf Landauer. "Spatial variation of currents and fields due to localized scatterers in metallic conduction". In: *IBM Journal of research and development* 1.3 (1957), pp. 223–231.

[40] M Büttiker. "Four-terminal phase-coherent conductance". In: *Physical review letters* 57.14 (1986), p. 1761.

[41] Gianluca Stefanucci and Stefan Kurth. "Steady-state density functional theory for finite bias conductances". In: *Nano letters* 15.12 (2015), pp. 8020–8025.

[42] Kaike Yang et al. "Density functional theory of the Seebeck coefficient in the Coulomb blockade regime". In: *Physical Review B* 94.8 (2016), p. 081410.

[43] Gianluca Stefanucci and C-O Almbladh. "Time-dependent quantum transport: An exact formulation based on TDDFT". In: *EPL (Europhysics Letters)* 67.1 (2004), p. 14.

[44] G Stefanucci et al. *Molecular and nano electronics: analysis, design and simulation*. 2006.

[45] S Kurth and G Stefanucci. "Nonequilibrium Anderson model made simple with density functional theory". In: *Physical Review B* 94.24 (2016), p. 241103.

[46] Neepa T Maitra, Kieron Burke, and Chris Woodward. "Memory in time-dependent density functional theory". In: *Physical review letters* 89.2 (2002), p. 023002.

[47] Niklas Dittmann, Janine Splettstoesser, and Nicole Helbig. "Nonadiabatic Dynamics in Single-Electron Tunneling Devices with Time-Dependent Density-Functional Theory". In: *Physical review letters* 120.15 (2018), p. 157701.

[48] Niklas Dittmann, Nicole Helbig, and Dante M Kennes. "Dynamics of the Anderson impurity model: Benchmarking a nonadiabatic exchange-correlation potential in time-dependent density-functional theory". In: *Physical Review B* 99.7 (2019), p. 075417.

[49] Harshani O Wijewardane and Carsten A Ullrich. "Time-dependent Kohn-Sham theory with memory". In: *Physical review letters* 95.8 (2005), p. 086401.

[50] Roberto D'Agosta and Giovanni Vignale. "Relaxation in time-dependent current-density-functional theory". In: *Physical review letters* 96.1 (2006), p. 016405.

[51] H Julian Goldsmid et al. *Introduction to thermoelectricity*. Vol. 121. Springer, 2010.

[52] Gianaurelio Cuniberti, Giorgos Fagas, and Klaus Richter. "Introducing molecular electronics: A brief overview". In: *Introducing molecular electronics* (2006), pp. 1–10.

[53] Juan Carlos Cuevas and Elke Scheer. *Molecular electronics: an introduction to theory and experiment*. World Scientific, 2010.

[54] Michael Thoss and Ferdinand Evers. "Perspective: Theory of quantum transport in molecular junctions". In: *The Journal of chemical physics* 148.3 (2018), p. 030901.

[55] Ferdinand Evers et al. "Advances and challenges in single-molecule electron transport". In: *Reviews of Modern Physics* 92.3 (2020), p. 035001.

[56] B Dutta et al. "Single-Quantum-Dot Heat Valve". In: *Physical Review Letters* 125.23 (2020), p. 237701.

[57] Cronin B Vining. "Half-full glasses". In: *Nature materials* 7.10 (2008), pp. 765–766.

[58] Cronin B Vining. "An inconvenient truth about thermoelectrics". In: *Nature materials* 8.2 (2009), pp. 83–85.

[59] Yonatan Dubi and Massimiliano Di Ventra. "Colloquium: Heat flow and thermoelectricity in atomic and molecular junctions". In: *Reviews of Modern Physics* 83.1 (2011), p. 131.

[60] Pierre Hohenberg and Walter Kohn. "Inhomogeneous electron gas". In: *Physical review* 136.3B (1964), B864.

[61] Robert G Parr and Weitao Yang. "Density-functional theory of atoms and molecules. International Series of Monographs on Chemistry". In: *Oxford University Press, New York* 3 (1994), pp. 14312–14321.

[62] Eberhard Engel and Reiner M Dreizler. *Density functional theory*. Springer, 2013.

[63] Walter Kohn and Lu Jeu Sham. "Self-consistent equations including exchange and correlation effects". In: *Physical review* 140.4A (1965), A1133.

[64] Narbe Mardirossian and Martin Head-Gordon. "Thirty years of density functional theory in computational chemistry: an overview and extensive assessment of 200 density functionals". In: *Molecular Physics* 115.19 (2017), pp. 2315–2372.

[65] John P Perdew, Kieron Burke, and Matthias Ernzerhof. "Generalized gradient approximation made simple". In: *Physical review letters* 77.18 (1996), p. 3865.

[66] N David Mermin. "Thermal properties of the inhomogeneous electron gas". In: *Physical Review* 137.5A (1965), A1441.

[67] Rolf Landauer. "Electrical resistance of disordered one-dimensional lattices". In: *Philosophical magazine* 21.172 (1970), pp. 863–867.

[68] M Büttiker et al. "Generalized many-channel conductance formula with application to small rings". In: *Physical Review B* 31.10 (1985), p. 6207.

[69] Gianluca Stefanucci and Robert Van Leeuwen. *Nonequilibrium many-body theory of quantum systems: a modern introduction*. Cambridge University Press, 2013.

[70] Gianluca Stefanucci and S Kurth. "Towards a description of the Kondo effect using time-dependent density-functional theory". In: *Physical review letters* 107.21 (2011), p. 216401.

[71] Kamil Walczak. "Coulomb blockade in molecular quantum dots". In: *Open Physics* 4.1 (2006), pp. 8–19.

[72] Nahual Sobrino, Stefan Kurth, and David Jacob. "Exchange-correlation potentials for multiorbital quantum dots subject to generic density-density interactions and Hund's rule coupling". In: *Physical Review B* 102.3 (2020), p. 035159.

[73] Gianluca Giovannetti. "The influence of Coulomb Correlations and Spin-Orbit Coupling in the electronic structure of double perovskites Sr _2 XOsO _6(X = Sc, Mg)". In: *arXiv preprint arXiv:1611.06482* (2016).

[74] Tanja Dimitrov et al. "Exact maps in density functional theory for lattice models". In: *New Journal of Physics* 18.8 (2016), p. 083004.

[75] E Perfetto and G Stefanucci. “Missing derivative discontinuity of the exchange-correlation energy for attractive interactions: The charge Kondo effect”. In: *Physical Review B* 86.8 (2012), p. 081409.

[76] PG Silvestrov and Yoseph Imry. “Level-occupation switching of the quantum dot, and phase anomalies in mesoscopic interferometry”. In: *New Journal of Physics* 9.5 (2007), p. 125.

[77] Yaakov Kleeorin and Yigal Meir. “Abrupt disappearance and re-emergence of the SU (4) and SU (2) Kondo effects due to population inversion”. In: *Physical Review B* 96.4 (2017), p. 045118.

[78] Philipp Tröster, Peter Schmitteckert, and Ferdinand Evers. “Transport calculations based on density functional theory, Friedel’s sum rule, and the Kondo effect”. In: *Physical Review B* 85.11 (2012), p. 115409.

[79] Gianluca Stefanucci and Stefan Kurth. “Kondo effect in the Kohn–Sham conductance of multiple-level quantum dots”. In: *physica status solidi (b)* 250.11 (2013), pp. 2378–2385.

[80] H Mera et al. “Assessing the accuracy of Kohn-Sham conductances using the Friedel sum rule”. In: *Physical Review B* 81.3 (2010), p. 035110.

[81] David C Langreth. “Friedel sum rule for Anderson’s model of localized impurity states”. In: *Physical Review* 150.2 (1966), p. 516.

[82] H Mera and YM Niquet. “Are Kohn-Sham Conductances Accurate?” In: *Physical review letters* 105.21 (2010), p. 216408.

[83] CA Büsser et al. “Transport in carbon nanotubes: Two-level SU (2) regime reveals subtle competition between Kondo and intermediate valence states”. In: *Physical Review B* 83.12 (2011), p. 125404.

[84] Justin P Bergfield et al. “Bethe ansatz approach to the kondo effect within density-functional theory”. In: *Physical review letters* 108.6 (2012), p. 066801.

[85] Nahual Sobrino, Roberto D’Agosta, and Stefan Kurth. “Steady-state density functional theory for thermoelectric effects”. In: *Physical Review B* 100.19 (2019), p. 195142.

[86] Yigal Meir and Ned S Wingreen. “Landauer formula for the current through an interacting electron region”. In: *Physical review letters* 68.16 (1992), p. 2512.

[87] Carlo WJ Beenakker. “Theory of Coulomb-blockade oscillations in the conductance of a quantum dot”. In: *Physical Review B* 44.4 (1991), p. 1646.

[88] TA Costi and V Zlatić. “Thermoelectric transport through strongly correlated quantum dots”. In: *Physical Review B* 81.23 (2010), p. 235127.

[89] M Abramowitz. “Handbook of Mathematical Functions with Formulas, Graphs, and Mathematical Tables”. In: *Dover Publications Inc., New York* (1965).

[90] Severin G Jakobs, Mikhail Pletyukhov, and Herbert Schoeller. "Nonequilibrium functional renormalization group with frequency-dependent vertex function: A study of the single-impurity Anderson model". In: *Physical Review B* 81.19 (2010), p. 195109.

[91] Wataru Izumida, Osamu Sakai, and Syunya Suzuki. "Kondo effect in tunneling through a quantum dot". In: *Journal of the Physical Society of Japan* 70.4 (2001), pp. 1045–1053.

[92] Herbert B Callen. "The application of Onsager's reciprocal relations to thermoelectric, thermomagnetic, and galvanomagnetic effects". In: *Physical Review* 73.11 (1948), p. 1349.

[93] Lars Onsager. "Reciprocal relations in irreversible processes. I." In: *Physical review* 37.4 (1931), p. 405.

[94] Nahual Sobrino et al. "Thermoelectric transport within density functional theory". In: *Physical Review B* 104.12 (2021), p. 125115.

[95] Stefan Kurth et al. "Nonequilibrium spectral functions from multiterminal steady-state density functional theory". In: *Physical Review B* 100.8 (2019), p. 085114.

[96] Keiji Saito et al. "Thermopower with broken time-reversal symmetry". In: *Physical Review B* 84.20 (2011), p. 201306.

[97] Kay Brandner and Udo Seifert. "Multi-terminal thermoelectric transport in a magnetic field: bounds on Onsager coefficients and efficiency". In: *New Journal of Physics* 15.10 (2013), p. 105003.

[98] Herbert B Callen. *Thermodynamics and an Introduction to Thermostatistics*. 1998.

[99] Miguel A Sierra and David Sánchez. "Nonlinear heat conduction in Coulomb-blockaded quantum dots". In: *Materials Today: Proceedings* 2.2 (2015), pp. 483–490.

[100] María Isabel Alomar, Jong Soo Lim, and David Sánchez. "Coulomb-blockade effect in nonlinear mesoscopic capacitors". In: *Physical Review B* 94.16 (2016), p. 165425.

[101] Y. Meir, N. S. Wingreen, and P. A. Lee. "Low-temperature transport through a quantum dot: The Anderson model out of equilibrium". In: *Phys. Rev. Lett.* 70 (1993), p. 2601.

[102] Ned S. Wingreen and Yigal Meir. "Anderson model out of equilibrium: Noncrossing-approximation approach to transport through a quantum dot". In: *Phys. Rev. B* 49 (16 1994), pp. 11040–11052.

[103] Qing-feng Sun and Hong Guo. "Kondo resonance in a multiprobe quantum dot". In: *Phys. Rev. B* 64 (15 2001), p. 153306.

[104] M. Krawiec. "Nonequilibrium Kondo effect in asymmetrically coupled quantum dots". In: *Phys. Rev. B* 66 (16 2002), p. 165408.

[105] N. Shah and A. Rosch. "Nonequilibrium conductance of a three-terminal quantum dot in the Kondo regime: Perturbative renormalization group study". In: *Phys. Rev. B* 73 (8 2006), p. 081309.

[106] P. Fritsch and S. Kehrein. "Nonequilibrium Kondo model with voltage bias in a magnetic field". In: *Phys. Rev. B* 81 (3 2010), p. 035113.

[107] G. Cohen et al. "Green's Functions from Real-Time Bold-Line Monte Carlo Calculations: Spectral Properties of the Nonequilibrium Anderson Impurity Model". In: *Phys. Rev. Lett.* 112 (2014), p. 146802.

[108] David Jacob and Stefan Kurth. "Many-body spectral functions from steady state density functional theory". In: *Nano letters* 18.3 (2018), pp. 2086–2090.

[109] Sareh Motahari. "Kondo physics and thermodynamics of the Anderson impurity model by distributional exact diagonalization". PhD thesis. Martin-Luther University Halle-Wittenberg, Germany, 2017.

[110] Ryan Requist. private communication.

[111] Corentin Bertrand et al. "Reconstructing nonequilibrium regimes of quantum many-body systems from the analytical structure of perturbative expansions". In: *Physical Review X* 9.4 (2019), p. 041008.

[112] TA Costi. "Kondo effect in a magnetic field and the magnetoresistivity of Kondo alloys". In: *Physical review letters* 85.7 (2000), p. 1504.

[113] Stefan Kurth and Gianluca Stefanucci. "Time-dependent i-DFT exchange-correlation potentials with memory: applications to the out-of-equilibrium Anderson model". In: *The European Physical Journal B* 91.6 (2018), pp. 1–7.

[114] Alexander L Fetter and John Dirk Walecka. *Quantum theory of many-particle systems*. Courier Corporation, 2012.